University of California
Santa Barbara

# Refractory Oxide Anodes For Fast-Charging Lithium-Ion Batteries

A dissertation submitted in partial satisfaction
of the requirements for the degree
Doctor of Philosophy
in
Materials
by

Kira Emily Wyckoff

Committee in charge:

Professor Ram Seshadri, Chair
Professor Raphaële Clément
Professor Michael Gordon
Professor Anton Van der Ven

September 2023

The Dissertation of Kira Emily Wyckoff is approved.

---

Professor Raphaële Clément

---

Professor Michael Gordon

---

Professor Anton Van der Ven

---

Professor Ram Seshadri, Committee Chair

September 2023

Refractory Oxide Anodes For Fast-Charging Lithium-Ion Batteries



by

Kira Emily Wyckoff

*To all of the scientists that have come before me, thank you for creating a framework for research, learning, and discovery*

# Acknowledgements

Thank you so much to my parents, Julia and Winston Wyckoff, for supporting my hobbies, dreams, and education for my entire life. From the plethora of farm animals I raised, to national level sports, to my desire to explore the world, I felt supported and loved in all of my endeavors. I was given the responsibility and freedom to make my own decisions from an early age, and that ultimately shaped me into the independent and confident person I am today. Thank you to my sister, Elena Wyckoff, for being my friend and supporting me. You constantly inspire me with your perseverance, positivity, and creativity.

Thank you to my grandparents, Emily and Al Wyckoff. To my grandma, thank you for showing me unconditional love and showering me with grandma cookies. To my grandpa, thank you for teaching me about my roots and inspiring me in so many ways. I will cherish the time we spent gardening, hunting on the farm, driving down country roads, fishing, and mushroom hunting. You showed me that deep relationships are built from actions, not words. Spending a significant amount of time in Iowa brought me peace, love, and perspective.

Thank you to Linus Kautzsch, my best friend and partner in life. We have become such a strong team over the years and it has brought me so much joy during my PhD to learn, grow, and have fun together. Thank you for your unconditional love and support. The future is bright.

I have lived with many people during my PhD that have become life long friends who I cherish dearly, from North San Marcos to Holiday Hill. First of all, thank you to Karen McBride for not only putting a roof over my head, but for becoming such a close friend. I must thank Bailey Rossi and Karen for a year of support and friendship

that I will never forget. Holiday Hill has been my home, and the people I lived with there have become family; Yolita Eggeler, Yaroslav Filipov, Vianna Mabanag, Patrick Mossman, Michael Fernandez.

I have been playing soccer and swimming at UC Santa Barbara for ten years and want to thank all of my sports friends for the fun we have had together. There are too many soccer teams to name, but one of the first was "Engineering Untied" and one of the last was "Your TA's". Jordan Snyder has been a close teammate, friend, and swimming buddy for many years.

Thank you to Nicole Schauser for your dear friendship. From the sea to the mountains to the lab, you are my Santa Barbara sister. Thank you to my office mates Arava Zohar and Salva Rezei, for discussion, friendship, and mutual appreciation for food and science.

Thank you to all of my collaborators, especially Jonas Kaufman, Jadon Bienz, Sun Woong Baek, Ananya Kepper, and Rebecca Vincent. It has been a joy to work together. Thank you to Sir Anthony Cheetham, for your guidance, insight, and direction. Your scientific knowledge and intuition is inspirational.

Thank you to Ram Seshadri for teaching me to love science and giving me the safety, support, and freedom to explore. This work was made possible because of your dedication to science and belief in me.

# Curriculum Vitæ

Kira Emily Wyckoff

## Education

| | |
|---|---|
| September 2018 – September 2023 | Ph.D. in Materials<br>Certificate in Graduate Managment Practice<br>University of California, Santa Barbara<br>Advisor: Professor Ram Seshadri |
| September 2015 – June 2017 | M.Sc. in Materials Science<br>University of California Santa Barbara |
| September 2012 – June 2016 | B.Sc. in Chemical Engineering<br>University of California Santa Barbara |

## Publications

13. K. E. Wyckoff*, A. Zohar*, T. Li, Y. Zhou, A. Patterson, L. Kautzsch, W. Wang, A. Kepper, L. Pilon, A. K. Cheetham, R. Seshadri "Atomic disorder and metallicity in fast-charging Wadsley-Roth anodes for lithium-ion batteries," *In preparation.* * These authors contributed equally to this work.
12. K. E. Wyckoff*, J. Bienz*, M. Saber, A. Van der Ven, A. K. Cheetham, R. Seshadri "Relating crystallographic features to rate performance in Wadsley-Roth materials for lithium-ion batteries," *In preparation.* * These authors contributed equally to this work.
11. A. Patterson, R. Elizalde-Segovia, K. E. Wyckoff, A. Zohar, P. Ding, W. Turner, K. Poeppelmeier, S. Narayan, R. Clément, R. Seshadri, and K. Griffith (2023) "Rapid and Reversible Lithium Insertion with Multielectron Redox in the Wadsley-Roth Compound $NaNb_{13}O_{33}$," *Chem. Mater.* 35: 6364–6373.
10. A. Zohar, K. E. Wyckoff, R. C. Vincent, T. E. Mates, and R. Seshadri (2023) "Controlling operating voltages in molybdenum oxide anodes through inductive effects," *Chem. Mater.* 35: 5009–5016.
9. K. E. Wyckoff, L. Kautzsch, J. Kaufman, B. R. Ortiz, A. Kallistova, G. Pokharel, J. Liu, K. M. Taddei, K. M. Wiaderek, S. H. Lapidus, S. D. Wilson, A. Van der Ven, and R. Seshadri (2023) "Electrochemical control of magnetism on the breathing kagome network of $Li_xScMo_3O_8$," *Chem. Mater.* 35: 4945–4954.
8. S. W. Baek, K. E. Wyckoff, D. D. Robertson, M. Frajnkovič, Y. Zhou, S. H. Tolbert, R. Seshadri, and L. Pilon (2023) "Operando calorimetry investigation of particle size effects on heat generation in Wadsley-Roth $(W_{0.2}V_{0.8})_3O_7$-based electrodes," *ACS Appl. Energy Mater.* 6: 1355—1367.

7. P. Vishnoi, J. L. Zuo, X. Li, D. C. Binwal, K. E. Wyckoff, L. Mao, L. Kautzsch, G. Wu, S. D. Wilson, M. G. Kanatzidis, R. Seshadri, and A. K. Cheetham (2022) "Hybrid layered double perovskite halides of transition metals," *J. Am. Chem. Soc.* 144: 6661–6666.

6. K. E. Wyckoff, J. Kaufman, S. W. Baek, C. Dolle, J. Zak, J. Bienz, L. Kautzsch, R. Vincent, A. Zohar, K. See, Y. Eggeler, L. Pilon, A. Van der Ven, and R. Seshadri (2022) "Metal-metal bonding as an electrode design principle in the low-strain cluster compound $LiScMo_3O_8$," *J. Am. Chem. Soc.* 144: 5841–5854.

5. S. D. Jones, H. Nguyen, P. M. Richardson, Y.-Q. Chen, K. E. Wyckoff, C. J. Hawker, R. J. Clément, G. H. Fredrickson, and R. A. Segalman (2022) "Design of polymeric zwitterionic solid electrolytes with superionic lithium transport," *ACS Central Sci.* 8: 169–175.

4. E. C. Schueller, Y. M. Oey, K. Miller, K. E. Wyckoff, R. Zhang, S. D. Wilson, J. R. Rondinelli, and R. Seshadri (2021) "$AB_2X_6$ compounds and the stabilization of trirutile oxides," *Inorg. Chem.* 60: 9224–9232.

3. S. W. Baek, K. E. Wyckoff, D. M. Butts, J. Bienz, A. Likitchatchawankun, M. B. Preefer, M. Frajkovič, B. S. Dunn, R. Seshadri, and L. Pilon (2021) "Operando calorimetry informs the origin of rapid rate performance in microwave-prepared $TiNb_2O_7$ electrodes," *J. Power Sources* 490: 229537.

2. K. E. Wyckoff*, D. D. Robertson*, M. B. Preefer, S. M. L. Teicher, J. Bienz, L. Kautzsch, T. E. Mates, J. A. Cooley, S. H. Tolbert, and R. Seshadri (2021) "High capacity $Li^+$ storage through multielectron redox in the fast-charging Wadsley–Roth phase$(W_{0.2}V_{0.8})_3O_7$," *Chem. Mater.* 32: 9415–9424. * These authors contributed equally to this work.

1. E. E. Levin, J. D. Bocarsly, K. E. Wyckoff, T. M. Pollock, and R. Seshadri (2017) "Tuning the magnetocaloric response in half-Heusler/Heusler $MnNi_{1+x}Sb$ solid solutions," *Phys. Rev. Mater.* 1: 075003(1–8).

**Abstract**

Refractory Oxide Anodes For Fast-Charging Lithium-Ion Batteries

by

Kira Emily Wyckoff

Lithium-ion batteries are a cornerstone of modern society. As the demand for batteries increases, and the types of applications expand and diversify, there is a huge momentum to improve and optimize all aspects of a battery. The electrode materials within a lithium-ion battery largely dictate the maximum capacity that can be stored and the charge rate. To improve these properties, it is necessary to develop accurate electrode material design strategies. This work examines a variety of refractory oxides as anode material candidates to develop a deeper understanding of the relationships between crystal structure and battery performance. Wadsley-Roth materials are a burgeoning class of high voltage anode materials, that are championed for their ability to store large amounts of charge at fast cycling rates. A variety of these materials are experimentally examined to understand the impact of transition metal selection, crystallographic features, disorder, and particle size on material performance. Data-mining efforts pulled a large number of published experimental data sets together to draw broader insight and design strategies for this material family. Inspired by crystallographic motifs in the Wadsley-Roth family, metal-metal bonding is evaluated as an alternative design strategy for fast-charging materials, using the Mo cluster compound $LiScMo_3O_8$. Detailed studies explore the unusual relationship between electrochemistry and magnetism in this material, illuminating the coupled relationship between lithium insertion, disorder, and electronic structure in this frustrated magnet. Together,

this work develops more nuanced understanding on the relationship between crystallographic features and high-rate properties, informing future material design strategies for fast-charging Li-ion batteries.

# Contents

# List of Figures

# List of Tables

# Chapter 1

# Introduction

## 1.1 Brief history of batteries

Battery technology is a cornerstone of modern society. Although battery technology generally has progressed rapidly in the past hundred years, the modern battery has only been made possible because of a series of discoveries and steps over arguably thousands of years. We cannot discuss batteries without introducing the concept of electricity, because the driving force for progressing battery technology directly relates to the ability to store and control electricity. Figure 1.1 shows an abridged schematic of the path towards modern day lithium-ion ($Li^+-$ion) batteries. One of the first recorded ways humans were cognizant of electricity and current was through shocks from electric fish. From both ancient Egyptian, Greek, Roman, and Arabic texts, we learn that physicians and naturalists were aware of electric shocks that could be delivered by a variety of eels, rays, and fish. Similarly, there are recorded observations in later years around 600 BCE about static electricity on objects such as rods of amber.

It would take millennia for more targeted scientific research on the topic, instigating

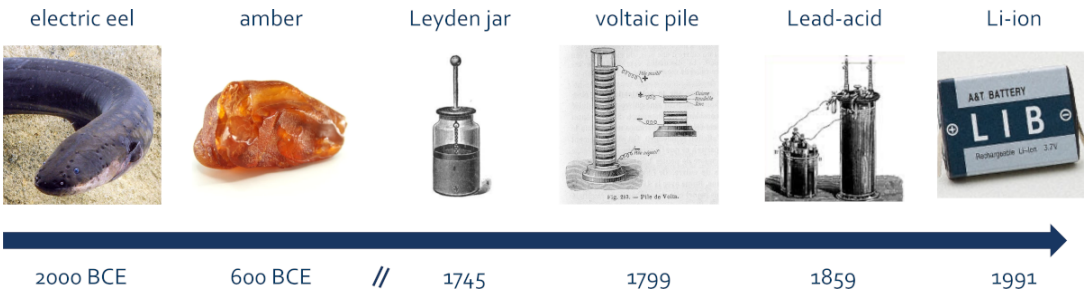


Figure 1.1: A high-level summary of the background and history of electricity as it relates to the development of the modern Li-ion battery.

larger momentum for the discovery, research, and understanding of electricity and batteries. In 1600, the English scientist William Gilbert coined the word electricus in his text *De Magnete*. In this text, he examined electricity and magnetism, and electricus was inspired by elektron, the Greek word for amber. This eventually led to the inclusion of "electric" and "electricity" in 1646 as English words in Thomas Brownes's Pseudodoxia Epidemica.

Through a combination of both accidental and intentional experiments over the next few hundred years, spanning multiple continents, more accurate and concrete physics were established. The Leyden jar, a simple capacitor made of metal foil and glass, was one of the first successful methods of storing charge. Italian biologist Luigi Galvani discovered in 1780 that an electric current caused a frogs legs to twitch when two different types of metal came into contact with the leg. In 1799 Alessandro Volta developed the foundation of a modern battery, the voltaic pile. By stacking copper and zinc metal foils, separated by electrolyte-infused brine, the voltaic pile was capable of producing a stable current. Today, this type of battery cell would be called a "primary cell". A milestone in battery development occurred less than sixty years later in 1859, when Gaston Planté invented the first rechargeable system, which is today called a "secondary" cell. He created the lead-acid battery, consisting of a lead anode, a lead

dioxide cathode, and a sulfuric acid electrolyte. The lead-acid battery, although both large and bulky, is still used in automotives today because of its reliability and ability to produce large currents in surges.

Other scientists pushed the development of "dry cells" including Georges Leclanché with ammonium chloride "Leclanché cell" in 1868 and Carl Gassner with an improved dry cell design in 1888. As scientists worked to advance cells that were more feasible with commercial potential, Waldemar Jungner, a Swedish engineer, invented the nickel-cadmium battery in 1899. This invention marked a major milestone in the development of storage batteries, and was the first battery that used an alkaline electrolyte. The next year, Thomas Edison introduced the nickel-iron battery, which was subsequently used in the locomotive and mining industries.

Although alkaline batteries revolutionized energy storage and are still widely used today, drawbacks such as weight and toxicity motivated the development of batteries based on $Li^+-$ions. Li became a clear target for next-generation battery technology because of its low atomic weight, small ion size, and high electrochemical potential. Although initial experiments began in the United States in 1912 by Gilbert Lewis, commercial $Li^+-$ion batteries did not emerge until the 1980's. Three important discoveries stand out as the driving force for the advancement of $Li^+-$ion batteries as commercially viable products. Stanley Whittingham outlined the basic principles for intercalation chemistry using Li with $TiS_2$ as a model host in a 2 V system.[1] John Goodenough improved upon this system by advancing oxide materials as alternative Li intercalation hosts. Namely, he discovered that $LiCoO_2$ served as a robust and high voltage (4 V) cathode material.[2] In both of these systems, metallic Li served as the anode, contributing to a hazardous and explosive system. Akira Yoshino substituted a carbon material, petroleum coke, for metallic Li, enabling a much safer, functioning, com-

mercial system. The first commercial $Li^+-$ion battery was released by Sony in 1991. These three individuals collectively won the Nobel Prize in Chemistry in 2019 for their scientific contributions, which together unlocked the potential for portable electronics. Modern research on batteries has focused on both continued optimization and advancement of $Li^+-$ion batteries, and future directions include work on multivalent batteries such as Mg and Ca. This thesis specifically focuses on the understanding and optimization of the electrode materials used in the modern $Li^+-$ion battery architecture.

## 1.2 Basic functionality of a battery

To motivate the research explored later in this thesis, it is necessary to describe the basic functionality of a $Li^+-$ion battery, displayed in Figure 1.2. Fundamentally, a $Li^+-$ion battery works by converting the change in free energy due to the transfer of $Li^+-$ions from the anode to the cathode into electrical work. As a note, anode and cathode materials are both considered generally "electrode materials", but the anode colloquially refers to a lower voltage electrode material and the cathode refers to a higher voltage electrode material. In a charged state, $Li^+-$ions reside in the anode while the cathode is Li deficient. Thermodynamically, the $Li^+-$ions would rather reside in the cathode. The electrolyte only allows the passage of $Li^+-$ions and so electrons must travel through an external circuit that connects the anode and the cathode. When the battery is charged and the electrodes (anode and cathode) are connected, the spontaneous reaction occurs where the $Li^+-$ions migrate from the anode to the cathode, and electrons flow through the external circuit. This is called "discharging" a battery.

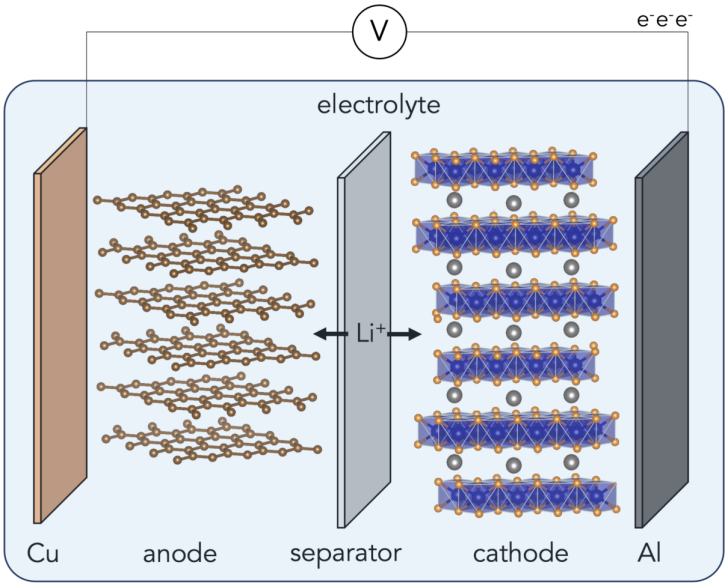


Figure 1.2: A schematic depicting a Li-ion battery in a discharged state.

Although there are many engineering aspects that govern the performance of a $Li^+-$ion battery in a system, the electrode materials themselves govern the performance on the atomic scale. This means to design better batteries, it is critical to design better electrode materials. Two important parameters to consider for electrode materials are the electronic conductivity and the ionic conductivity. These both have important ramifications on performance relating to charge rate, capacity stored, and battery efficiency. Ideally, a battery would be able to store a large amount of charge quickly, over thousands of cycles. The goal of this thesis is to work towards understanding how to design materials that are capable of this, using low voltage anode materials as research platforms.

## 1.3 Applications reliant on batteries

$Li^+-$ion batteries have become so ubiquitous over the last 30 years that it is easy to take them for granted. But in actuality, $Li^+-$ion batteries represent a hugely impressive feat of science and engineering. The first application of the modern $Li^+-$ion battery was to power a Sony camcorder. Since then, the number of applications has exponentially increased, from portable electronics, to medical devices, to renewable energy storage, to the skyrocketing production of electric vehicles. Figure 1.3 outlines select $Li^+-$ion battery applications and their associated energy storage needs.

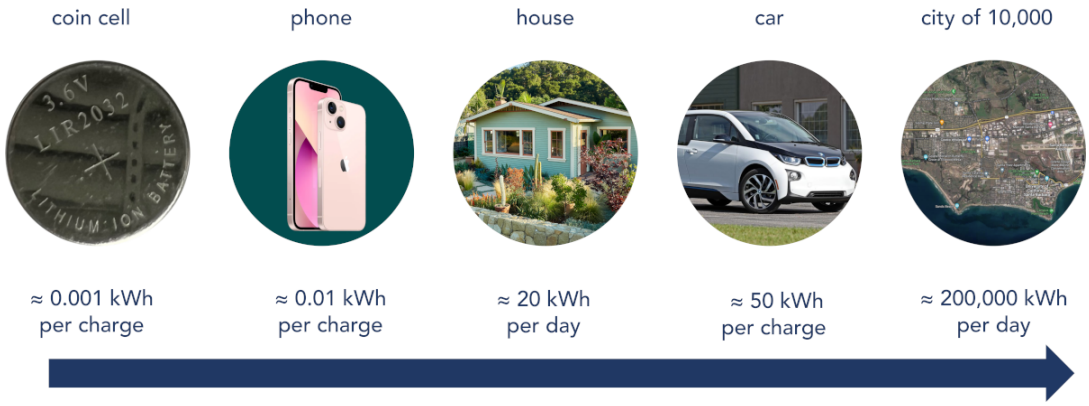


Figure 1.3: A schematic illustrating a range of energy requirements for $Li^+-$ion batteries.

As the applications for $Li^+-$ion batteries broadens, it is important to acknowledge that each application has its own hierarchy of needs with regards to its battery usage. For example, an electric toothbrush does not need to charge quickly, but a cell phone does. And even within an application class, such as electric vehicles, the market is segmented. For example, some consumers are happier with less expensive, lower range (ie. lower capacity) cars, while others desire a high-end vehicle that can change in 15 minutes and drive 400 miles on a single charge. With a huge diversity in applications and needs, it has become clear that there is no single optimal electrode material. There

will always be trade-offs between capacity, charge rate, voltage, cost, longevity, and safety. It is necessary to be able to custom-design batteries from a range of electrode materials that can satisfy different needs. The work in this thesis aims to diversify candidate anode materials to drive improvements in fast-charging capabilities.

## 1.4 Technical primer on electricity

The following section provides a summarized glossary of relevant terms and units, in addition to brief overview of basic battery cycling experiments.

### 1.4.1 Electrons, charge, energy, and current

The quantum of charge is that carried by a single electron, of magnitude $|e|$. Charge is measured in coulombs C, and the electronic charge is:

$$|e| = 1.602 \times 10^{-18}\,\mathrm{C} \tag{1.1}$$

The charge on its own is not associated with an energy, but under the influence of an electric field, whose potential is measured in volts V, the electron (or other charge) takes on an energy $E$ that is simply the product of charge and voltage $V$. For an electron experiencing a 1 V potential, the energy is

$$E = |e| \times V \quad \text{in units of eV} \tag{1.2}$$

and 1 eV = $1.602\times10^{-19}$ J.

A Faraday is the charge of Avogadro number of electrons, so

$$F = |e| \times N_A \quad \text{in units of } \mathrm{C\,mol^{-1}} \tag{1.3}$$

and 1 $F$ = 96,485.332 $\mathrm{C\,mol^{-1}}$ .

The base unit of electric current is an ampere, A. An ampere is defined as one coulomb of charge going past a point in one second, mathematically written as

$$\mathrm{A} = \mathrm{C} \times \mathrm{s}^{-1} \tag{1.4}$$

The unit of electric charge typically used for batteries is the ampere hour. This metric can be understood as how long a certain amount of current can be sustained until the battery is fully discharged.

$$1\mathrm{A\,h} = 3600\,\mathrm{C} \tag{1.5}$$

The ampere hour is conventionally known as the battery capacity. Battery capacity can also be normalized by mass.

The joule (J) is a unit of energy. One joule is defined as the work required to move an electric charge of one coulomb through a potential difference of one volt.

$$\mathrm{J} = \mathrm{C} \times \mathrm{V} \tag{1.6}$$

Power is measured in watts W. A watt is defined as the rate at which electrical work

is performed in joules per second. Because of the definition of a joule, a watt can also be defined as the rate at which electrical work is performed when a current of one ampere flows across a potential difference of one volt.

$$\mathrm{W} = \mathrm{J} \times \mathrm{s}^{-1} = \mathrm{C} \times \mathrm{V} \times \mathrm{s}^{-1} = \mathrm{V} \times \mathrm{A} \tag{1.7}$$

Although the base unit for time is the second s, energy in a battery is typically measured in watt-hours Wh. One watt-hour is equal to one watt of output for one hour, so

$$1\mathrm{W\,h} = 3600\,\mathrm{J} \tag{1.8}$$

When comparing electrode materials, it can be useful to normalize power and energy by mass or volume.

An ideal capacitor has a constant capacitance $C$, described by the following equation,

$$C = \epsilon \frac{A}{d} \tag{1.9}$$

where $\epsilon$ is the permittivity of the dielectric material, $d$ is the separation between the plates, and $A$ is the area of the plates. Capacitance is measured in farads F, and the units of a farad are:

$$\mathrm{F} = \mathrm{C} \times \mathrm{V}^{-1} = \mathrm{A} \times \mathrm{s} \times \mathrm{V}^{-1} \tag{1.10}$$

The charge of a capacitor is equal to the capacitance multiplied by the voltage difference between the plates.

$$q = C \times \mathrm{V} \tag{1.11}$$

If we take the derivative of the charge and voltage with respect to time we can extract a relationship between the current and the sweep rate.

$$\frac{dq}{dt} = C\,\frac{dV}{dt} \tag{1.12}$$

$$i = C \times \frac{dV}{dt} \tag{1.13}$$

The maximum energy of a capacitor is

$$\mathrm{E} = \frac{1}{2} \times Q \times V = \frac{1}{2} \times C \times V^2 \tag{1.14}$$

The prefactor in this equation comes from an integral involved in the derivation. From equation 1.6, one can see that the voltage represents energy per unit charge and rearrange to get the following:

$$dE = V \times dq \tag{1.15}$$

Using the relationship in equation 1.11, one can replace the voltage with a charge per capacitance to get

$$dE = q \times C^{-1} \times dq \tag{1.16}$$

The total energy stored in a capacitor is obtained from the following integral if Q represents the total amount of charge stored when the whole voltage difference appears across the plates.

$$E = \int_0^Q q \times C^{-1}\, dq = \frac{1}{2} \times Q^2 \times C^{-1} \tag{1.17}$$

Using equation 1.11 again, it is possible to simplify the expression.

$$\mathrm{E} = \frac{1}{2} \times Q^2 \times C^{-1} = \frac{1}{2} \times Q \times V = \frac{1}{2} \times C \times V^2 \tag{1.18}$$

## Equations in practice

### Galvanostatically coupled cyclic voltammetry experiment (GCPL)

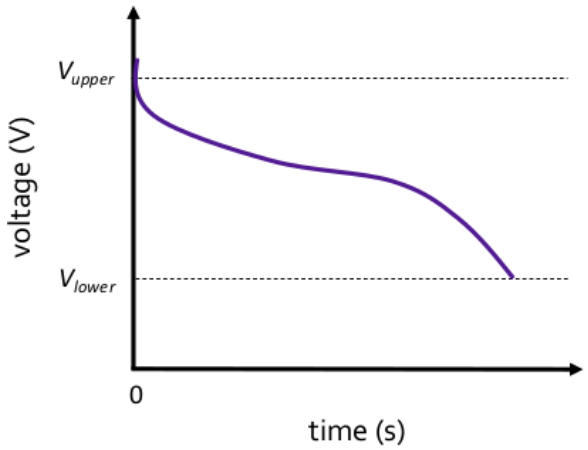


Figure 1.4: Schematic of a discharge curve in a GCPL experiment that shows the upper and lower voltage bounds. The current applied is constant.

In a GCPL experiment, a constant applied current is swept between a specified voltage window. As the current is applied, the potentiostat measures the amount of time it takes to reach the specified voltage limit. This time can be converted to capacity using equation (1.4).

$$q = i \times \text{time} = \frac{\text{C}}{\text{s}} \times \text{s} = \text{C} \tag{1.19}$$

The number of coulombs of charge stored can then be converted to $x$ Li using the Faraday constant $F$ from equation 1.2, the molar mass of the material $M$, and the mass of the active material g.

$$x\,\text{Li} = q \times M \times (F \times \text{g})^{-1} = \text{C} \times \left(\frac{\text{g}}{\text{mol}}\right) \times \left(\frac{\text{mol}}{\text{C}}\right) \times \left(\frac{1}{\text{g}}\right) \tag{1.20}$$

The number of coulombs of charge stored can also be converted to the more commonly used capacity metric mA h $g^{-1}$ using equation 1.4.

$$\text{mA h g}^{-1} = \text{C} \times \left(\frac{1}{\text{g}}\right) \times \left(\frac{1\,\text{hr}}{3600\,\text{s}}\right) \times \left(\frac{1000\text{mA}}{1\text{A}}\right) \tag{1.21}$$

**Cyclic voltammetry experiment (CV)**

In a cyclic voltammetry experiment, the voltage is swept linearly with time and the current response is measured. The current response can give valuable information about redox reactions occurring in the cell. The charge stored for a cyclic voltammetry experiment can be calculated using the sweep rate and by integrating the current response with respect to voltage between the voltage bounds, described by the following equation.

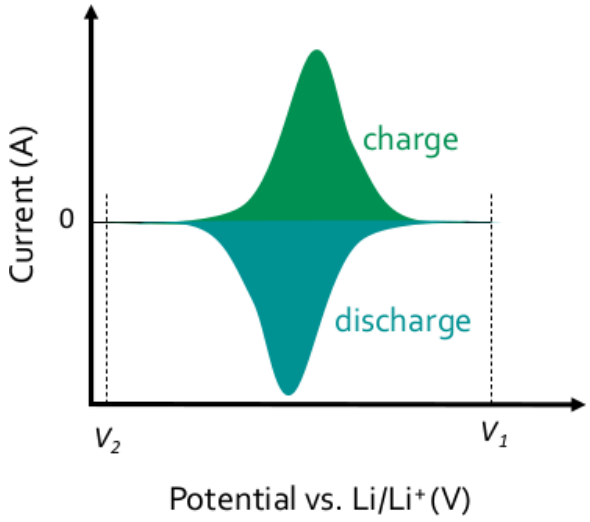


Figure 1.5: Schematic of a cyclic voltammetry experiment. The shaded area in blue shows the area under the curve for a discharge and the shaded area in green shows the area under the curve for charging. The voltage sweep rate is constant.

$$q = \frac{1}{v}\int_{V_1}^{V_2} i\,dV = \frac{\mathrm{s}}{\mathrm{V}} \times \mathrm{A} \times \mathrm{V} = \mathrm{C} \tag{1.22}$$

## 1.5 Electrode design strategies and thesis outline

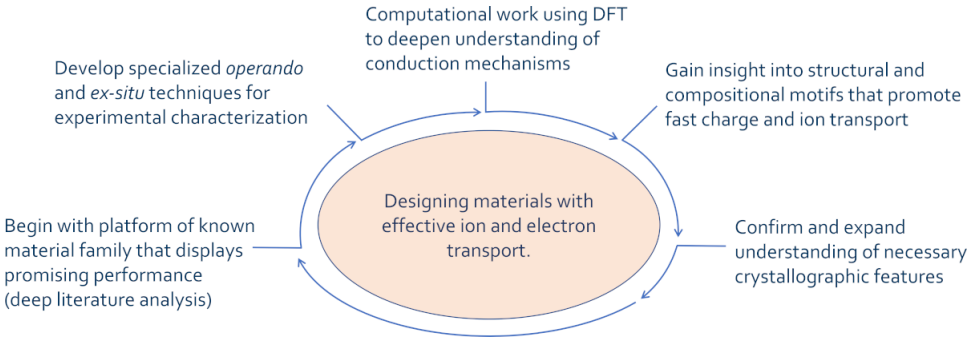


Figure 1.6: An overview schematic depicting the general workflow of the work carried out in this thesis.

Through study of a wide variety of refractory oxide materials, this thesis aims to provide more insight into specific design strategies for improving fast-charging capabilities

in $Li^+$−ion batteries. Figure 1.6 outlines the general research workflow for this body of work. The overarching goal of this research is to design materials with more effective ion and electron transport. We first begin with a platform of a know material family that displays promising performance. We then develop and use specialized *operando* and *ex-situ* techniques to experimentally characterize these materials. DFT-based calculations are additionally used to deepen our understanding of conduction mechanisms. Experimental results, combined with computational work, provide insight into structural and compositional motifs that promote fast charge and ion transport. We are then able to confirm and expand our understanding of necessary crystallographic features that drive improved battery performance. By following an iterative scheme, this thesis examines a variety of material systems, drawing insight about transition metal selection, crystallographic features, disorder, particle size, and magnetism in refractory oxide anode materials.

Wadsley-Roth materials have been gaining traction recently because of their remarkable fast-charging capabilities. First reported in the 1960's, these primarily niobium-based materials have a unique type of polyhedral connectivity that is commonly referred to as a "shear structure" or "block structure". It has become understood that these materials display outstanding performance as higher voltage anodes, but the precise mechanisms driving their performance remain less well understood.

Chapter 2 explores one of the more unique materials in the Wadsley-Roth family, $(W_{0.2}V_{0.8})_3O_7$. This material does not contain any niobium, but instead is comprised of both tungsten and vanadium. Vanadium is one row above niobium on the periodic table and is more electronegative. The influence of vanadium in this material has not been previously explored for electrochemistry and we use this model Wadsley-Roth system to explore fundamental questions relating its crystal structure to performance using

X-ray powder diffraction, microscopy, detailed electrochemistry, X-ray photoelectron spectroscopy, and theoretical calculations. We additionally compare the performance of both micron- and nano-sized particles of the same composition to better understand the impact of particle size to fast-charging capabilities in Wadsley-Roth materials. This study demonstrated similar fast-charging capabilities between both large and small particles, indicating that the atomic-scale crystallographic features, namely a combination of edge- and corner-sharing polyhedra, truly drive the intrinsic rate performance in these systems.

Building off the previous work in Chapter 2, we aim to draw more universal insight about structural motifs that promote fast charge and ion transport through data-mining efforts in Chapter 3. By aggregating published electrochemical data on Wadsley-Roth materials from the literature, we aim to better understand why some materials perform better than others within the same family. It is generally understood that these materials are all high-performance anodes, but it is less well understood what differentiates their performance. Because these data come from a variety of different sources, we develop new metrics to compare fast-charging capabilities in a standardized manner, such as the capacity retention from 1C to 10C. This normalized performance metric allows for the comparison of innate rate capabilities between materials. These data show that differences in performance likely relates to the relative amount of shear connectivity (edge-sharing polyhedra) in a structure. This chapter examines possible connections between structural features and battery performance in an effort to develop more nuanced design strategies for fast-charging electrode materials.

Inspired by the favorable crystallographic features in the Wadlsey-Roth materials, we evaluate and study how an alternative bonding scheme can impact electrochemical performance in anode materials. $LiScMo_3O_8$ is a layered refractory oxide material

that contains a network of metal-metal bonded Mo atoms. We use this material as a model system to understand how the metal-metal bonding scheme affects capacity, structural stability, and fast-charging capabilities, as described in Chapter 4. We are able to probe fundamental questions about the use of Mo as the redox-active species in an anode material, and how metal-metal bonding affects the structural stability of an electrode material during Li insertion and deinsertion. A variety of advanced characterization techniques such as *operando* X-ray diffraction, *operando* Raman spectroscopy, and *operando* calorimetry, are paired with detailed calculations that indicate minimal structural changes occur during cycling. These findings additionally show that although the framework of the material does not change significantly with Li insertion, there is evidence for a unique evolution of Li ordering in the material.

While the initial work on $LiScMo_3O_8$ focused on the implications of metal-metal bonding as it relates to electrochemical performance, Chapter 5 more deeply explores the electronic and magnetic evolution of the material with Li insertion. The metal-metal bonded Mo atoms in $LiScMo_3O_8$ comprise a layered breathing-kagome network, that has been shown to lead to interesting physics in related systems. Electrochemistry and magnetism are intimately related, but their relationship is largely overlooked in the literature. Here we perform *operando* X-ray diffraction and *ex-situ* magnetic, heat capacity, and neutron diffraction measurements to understand how Li insertion impacts the electronic structure of this material. Combined with DFT-based calculations, we explain the likely coupling between charge, spin, and Li ordering in this system. This work highlights the innate intersection between Li insertion, disorder, and electronic structure in a frustrated magnetic material.

# Chapter 2

# High Capacity $Li^+$ Storage through Multielectron Redox in the Fast-Charging Wadsley–Roth Phase $(W_{0.2}V_{0.8})_3O_7$

## 2.1 Abstract

The Wadsley–Roth phase $(W_{0.2}V_{0.8})_3O_7$, crystallizing in a structure obtained through crystallographic shear of $3\times3\times\infty$ $ReO_3$ blocks, is a somewhat rare exemplar for this class of compounds in that it contains a relatively small amount of 4d and/or 5d transition elements. Here we demonstrate that it functions as a high-rate, high-capacity

Reproduced with permission from K. E. Wyckoff,* D. D. Robertson,* M. B. Preefer, S. M. L. Teicher, J. Bienz, T. E. Mates, J. A. Cooley, S. H. Tolbert, and R. Seshadri. High Capacity $Li^+$ Storage through Multielectron Redox in the Fast-Charging Wadsley–Roth Phase $(W_{0.2}V_{0.8})_3O_7$ *Chem. Mater.* 32(21), 9415-9424 (2020). (* equal contribution)

material for lithium ion batteries. Electrochemical insertion and de-insertion in micron sized particles made by conventional solid-state preparation and in sub-100 nm particles made by combining sol-gel precursors with freeze-drying methods, indicate good rate capabilities. The materials display high capacity — close to 300 mAh $g^{-1}$ at low rates — corresponding to insertion of up to 1.3 Li per transition metal at voltages above 1 V. Li insertion is associated with multielectron redox for both V and W observed from ex-situ X-ray photoelectron spectroscopy. The replacement of 4d and 5d elements with vanadium results in a higher voltage than seen in other, usually niobium-containing shear-structured electrode materials, and points to new opportunities for tuning voltage, electrical conductivity, and capacity in compounds in this structural class.

## 2.2 Introduction

The ability to tune the chemistry of electrode materials across multiple length scales provides opportunities for developing electrodes for a variety of Li–ion battery applications, ranging from portable electronics, to electric vehicles, and grid-scale storage.[3, 4] Research on Li-ion battery technology has particularly focused on improving both the energy density and rate capabilities of electrode materials.[5] Materials capable of being charged in the course of minutes as opposed to hours, could have important ramifications across a broad range of applications. For many currently used and studied materials, fast charging is hindered due to intrinsic materials properties often associated with the crystal structure, namely the ease of ion and electron transport, structural and electronic phase transitions *etc.*. A common work-around to address limited ion mobility has been to optimize particle morphology through meso- and nanostructuring,[6, 7] with the goal of decreasing Li–ion diffusion distances within

the particle, sometimes with concomitant suppression of phase transitions.[8–11] Carbon additives and carbon-coating has also been frequently employed to overcome inherently poor electron transport.[12, 13] These impressive feats of engineering, exemplified by materials such as $LiFePO_4$,[12, 13] have allowed for broad adoption of Li–ion batteries in many applications, but the search for new materials continues.

Anode materials with voltages close to 0 V *vs.* $Li/Li^+$, while providing the greatest energy density, are contraindicated for high-rate applications. Graphite for example, effectively transports $Li^+$ ions and electrons but is associated with detrimental electrolyte reactions,[14] dendrite formation that leads to thermal runaway,[15–17] and volume expansion that leads to particle fracture.[18] Highly engineered (*ie.* nanoscaled and carbon-coated) $Li_4Ti_5O_{12}$ with a higher average voltage of 1.5 V has good capacity retention at high rates.[19] The higher voltage minimizes dendrite growth but the costs associated with elaborate electrode preparation decreases widespread adoption.[20]

The focus of this work are on materials that possess crystallographic shear. These are structures that derive from anion vacancies that are accommodated through shear of the basic polyhedral structural motifs. First described by Magnéli,[21] the process of shear results in greater sharing of anions between polyhedra. A class of materials that possess such crystallographic shear are the so-called Wadsley–Roth family of compounds, which have shear structures described as blocks of corner-connected $MO_3$ octahedra. These generally comprise oxides of early transition metals such as Ti, V, Nb, Mo, and W.[22–25] While the earliest reports on these structures were based on electron diffraction and model-building, neutron diffraction has revealed the most intricate structural details.[26, 27]

Early studies on Li insertion in this class of materials showed that a broad array of compositions could be used as electrodes.[28–32] The utility of $TiNb_2O_7$ was redis-

covered by Goodenough and coworkers.[33, 34] Recent studies have demonstrated that large micron-sized particles of the shear structured phases $Nb_{12}WO_{33}$,[35] H–$Nb_2O_5$,[36, 37] $TiNb_{24}O_{62}$,[38] $Nb_{16}W_5O_{55}$,[39] $TiNb_2O_7$,[40] $MoNb_{12}O_{33}$,[41] and $PNb_9O_{25}$,[42] are all capable of impressive lithium storage capacity at high cycling rates.

From a design perspective, compounds displaying features of crystallographic shear are exciting because they contain specific structural motifs that allow for excellent Li–ion diffusion and the potential for electron delocalization. The compounds typically possess some combination of edge- and corner-connected octahedra. How these combine in the structure, along with the specific chemical composition, critically impacts electrochemical performance. The edge-sharing octahedra allow for electron delocalization pathways while also providing structural integrity.[43] This integrity protects against octahedral tilting and rotation seen in pure $ReO_3$ structures (all corner– and no edge–sharing) that are detrimental to reversible cycling.[28, 31, 44] However the corner connectivity deriving from the $ReO_3$ blocks also plays an essential role in creating channels that facilitate ion insertion and transport. Evidence from NMR, magnetism, and conductivity measurements confirms that these structural features contribute to low activation barriers for lithium diffusion.[37, 38, 40, 42, 45] These materials are additionally compelling because of their high capacities. This is due in large part to the fact that these materials comprise of early transition metals capable of multi-electron redox, where it is possible to insert more than 1 Li per transition metal.

While many Wadsley–Roth phases contain Nb, V-containing phases appear to have been much less studied, despite the fact that vanadium is more earth-abundant and more geographically and industrially widespread, compared to niobium.[46] Here we characterize the electrochemical insertion properties of the Wadsley–Roth phase

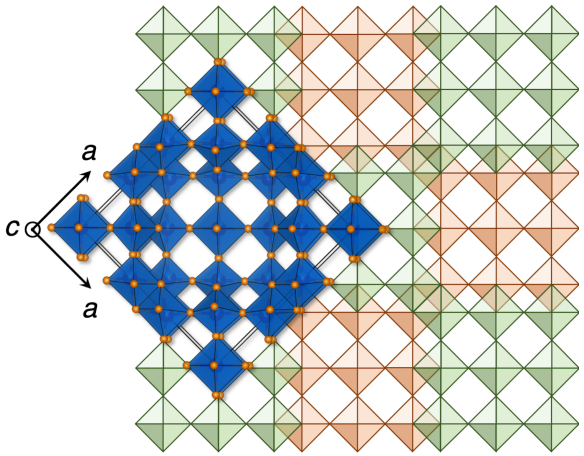


Figure 2.1: Crystal structure of $(W_{0.2}V_{0.8})_3O_7$ (space group is $I_4/mmm$, No. 139) comprising of 3×3×∞ blocks of corner-connected (W,V)$O_3$ octahedra, offset and connected through edge-sharing (shear planes). The real structure is overlaid onto a schematic that depicts the arrangement of the 3×3 blocks. The two different colors employed for the blocks of octahedra are used here to indicate that they are offset along the $c$ direction.

$(W_{0.2}V_{0.8})_3O_7$, whose crystal structure is depicted in figure 2.1. First reported by Galy in 1972, the crystallography of this 3×3×∞ block structure was determined from single-crystal studies.[47] From the viewpoint of composition, this is an interesting compound since the closest vanadium phase to $V_3O_7$ is formed under high-pressure with a distinctly different structure,[48] and a $W_3O_7$ phase does not appear to have been reported. There is a high likelihood that $(W_{0.2}V_{0.8})_3O_7$ is stabilized by configurational entropy, as suggested by Navrotsky and coworkers for related phases.[49]

Early studies examined related compounds as electrodes,[29, 30, 32] but not for high-rate performance. Here, using both small particles prepared through a solution freeze-drying method, and conventionally prepared larger particles, we develop an understanding of the intrinsic capabilities of the materials for Li storage. Reversible and stable cycling at rates up to 20C are demonstrated. The relatively minor perturbation of the structure arising from Li insertion is confirmed with *operando* X-ray diffraction. Ex-situ X-ray photoelectron spectroscopy studies show reduction of the transition met-

als, respectively to $V^{3+}$ and $W^{4+}$, explaining the relatively high capacity. Despite the competitive capacity retention in bulk particles of $(W_{0.2}V_{0.8})_3O_7$, there are kinetic advantages displayed by the smaller particles made by the solution freeze-drying route, particularly at intermediate rates.

The materials studied here differentiate themselves from other Wadsley–Roth phases in that they are not fully oxidized even in the pristine, delithiated state, which contributes to some electronic conductivity prior to lithium insertion. Additionally, the compound stores charge at voltages higher than found in related structures and provides the basis for exploration of voltage tuning within the family of crystallographic shear structures.

## 2.3 Experimental Methods

The title material was conventionally prepared (labelled Conv.) through solid-state methods. Stoichiometric quantities of $WO_3$ (Sigma Aldrich, 99.9 %), $V_2O_5$ (Materion, 99.9 %), and $V_2O_3$ (Strem Chemicals, 95 %) were ground together and pressed into pellets weighing between 250 mg and 300 mg. The pellets were then placed in a vitreous silica tube and sealed with a methane-oxygen torch, evacuated three times, and subsequently filled with 40 mm Hg partial pressure of Ar. The tube was annealed in a furnace at 700°C for 24 h followed by a water quench to room temperature. Small particles were prepared by freeze-drying (henceforth labelled FD) a stoichiometric solution of precursors and subsequently calcining under flowing Ar. In a typical preparation, 200 mg of $NH_4VO_3$ and 105 mg of $(NH_4)_{10}(H_2W_{12}O_{42})$ were added to 5 $cm^3$ of distilled water and heated until the solids were fully dissolved. The resulting yellow solution was added drop-wise to liquid $N_2$. After removal of the remaining liquid $N_2$, the frozen

solution was subjected to vacuum (<100 mTorr) on a Schlenk line for 10 h to 20 h to remove water. Once dry, the powder was calcined in flowing Ar in a tube furnace at 700°C for 1 h (30°C per min ramp rate). The furnace was then cooled to room temperature. The obtained particles were stored under inert atmosphere to prevent unwanted surface oxidation.

Both materials were cast on copper foil in an 80:10:10 (wt-%) ratio of active material:conductive carbons:polyvinylidene fluoride. Cycling of the Conv. material employed carbon black (TIMCAL Super P) while for the FD material, a 50:50 mixture of carbon nanotubes and carbon nanofibers were used. The active material was ball milled for 30 min in a 2 $cm^3$ canister with the appropriate amount of carbon based additives. This mixture was combined with PVDF dissolved in NMP to form a slurry that was mixed in a FlackTek speed mixer at 2000 rpm for 30 min. A 120 $\mu$m doctor blade was used to cast the material onto copper foil, and this film was dried at 110°C under vacuum for 2 h. The electrodes were punched as 10 mm diameter disks with a loading of 1 mg $cm^{-2}$ to 2 mg $cm^{-2}$.

All electrochemical cells were fabricated in an Ar-filled glovebox. Unless noted otherwise, Swagelok cells were employed with 1 M $LiPF_6$ in EC/DMC 50/50 $v/v$ (Sigma Aldrich) with a polished Li foil counter electrode and a glass fiber separator (Whatman GF/D). Cells were discharged to 1 V and charged to 3.2 V. All electrochemical experiments were performed using BioLogic potentiostats.

The compound $(W_{0.2}V_{0.8})_3O_7$ can be considered to comprise $0.6WO_3$ + $1.6VO_2$ + $0.8VO_{2.5}$. W can be reduced to the $4^+$ state and V to the $3^+$ state (as we shall also demonstrate presently), so on this basis, 4.4 electrons (along with the corresponding $Li^+$ ions) can in principle be incorporated. However, following the usual convention for this class of materials, C-rates were calculated based off the reduction of one elec-

tron per redox-active transition metal. In this case, 3 Li were assumed to insert into the crystal structure for calculating C rates, *eg.* C/5 = $3Q/5$ = 233 mAh $g^{-1}$/5 h = 46.6 mA $g^{-1}$, where $Q$ is the charge.

Electrochemical impedance spectroscopy was carried out on a BioLogic VSP potentiostat/galvanostat. Impedance measurements were performed on two-electrode coin cells between 900 kHz and 100 mHz using a 10 mV input. Impedance spectra were collected at every 0.2 V vs. $Li/Li^+$ between +1.0 V and +3.2 V vs. $Li/Li^+$ on electrodes that had been previously cycled with galvanostatic rate testing between +1.0 V and +3.5 V vs. $Li/Li^+$. A one hour potentiostatic hold was applied before impedance measurements, during which the current dropped below 50 $\mu$A/g.

Powder diffraction data to establish sample purity were collected on a Panalytical Empyrean diffractometer with a $CuK_\alpha$ source ($\lambda$ = 1.5406 Å). The materials were ground and loaded on a silicon zero diffraction plate. Rietveld refinements to the previously published structure[47] were carried out with TOPAS.[50] VESTA was used for visualization of the crystal structure.[51]

Particle sizes and morphologies were studied using an FEI Apreo C scanning electron microscope. The powder samples were pressed onto double-sided copper tape and sputter-coated with gold for 60 s. Images were collected with a voltage of 15 kV and a current of 0.8 nA.

For *operando* X-ray diffraction, the electrode mixture was pressed into a 15 mm diameter pellet and placed into a custom electrochemical cell with a Be window. A glass fiber separator (Whatman, GF/D) was soaked in 1 M $LiPF_6$ (Sigma Aldrich), and the counter electrode was a polished Li metal disc pressed into a stainless steel current collector. The cell was cycled galvanostatically at a rate of C/10 (assuming 3 Li per formula unit) for one complete cycle. X-ray diffraction patterns were collected repeat-

edly using the Panalytical Empyrean diffractometer referenced above, from $2\theta = 13^\circ$ to $50^\circ$ over 17 min. intervals. The amorphous background (due to the glass fiber separator) and the signal for each scan was separately smoothed and fit using Tikhonov regularization.[52].

Samples for X-ray photoelectron spectroscopy (XPS) were prepared by discharging/charging the cast electrodes described earlier to the desired voltages in a Swagelok cell. These cells were then disassembled inside of an Ar-filled glovebox, the electrodes were removed and washed for 2 hours in dimethyl carbonate to remove $LiPF_6$ from the electrolyte, with subsequent centrifuging and drying in the glovebox atmosphere overnight. A section of the electrode was cut and the copper foil side of the disk was gently pressed onto the XPS sample holder using double-sided tape. A custom-built, capped XPS holder was used, equipped with a Viton seal and a screw-down lid that could be removed after the sample achieved vacuum in the XPS antechamber. All samples were measured using a Thermo Fisher Escalab $Xi^+$ XPS equipped with a monochromatic Al anode ($E = 1486.7$ eV). Samples were etched using a cluster gun for 40 s to clean the surface and improve count intensity. Survey scans were measured at 100 eV pass energy, and high-resolution scans were measured in the V $4p$, W $4f$, and Li $1s$ regions at 20 eV pass energy. Ex-situ spectra were referenced to the F $1s$ peak from LiF at 685.5 eV and the pristine spectrum was referenced to adventitious carbon at 285 eV.[53–55] CasaXPS was used to fit the data using Shirley backgrounds and GL(30) peak shapes. High resolution scans of V and W were fit using appropriate spin-orbit splitting and peak area ratios.[56]

Density functional theory (DFT) – based electronic structure calculations were performed using the Vienna ab initio Simulation Project VASP $v$5.4.4[57–59] employing projector augmented wave potentials[60, 61] with energy convergence better than

$10^{-6}$ eV. PAW potentials were selected based on the version 5.2 recommendations. Simulations were found to be well-converged for an energy cutoff of 500 eV and an automatically generated $k$-mesh with the length-density parameter $\ell = 50$ ($\ell = 50$ corresponds to 14×5×5 and 4×4×13 Γ-centered meshes for the primitive cell and the conventional cell displayed in the text, respectively). PBE[62] and SCAN[63] functionals were employed for calculations on the $V_3O_7$ model structure. The SCAN functional often provides improvements over PBE accuracy for systems with localized electrons, and previous studies have found improvements with SCAN estimates of magnetic moments specifically for transition metal oxide battery materials.[64] However, in these simulations, for ferromagnetic initialization with and without spin-orbit coupling, we find no stable magnetization in either structure regardless of functional choice. PBE and SCAN densities of states (DOS) and charge densities are visually indistinguishable and only the results obtained with the SCAN functional are reported in the text. The projected density of states was post-processed using LOBSTER.[65–68] Mapping of the bond valence in the space of the crystal structure was carried out using the script PYABSTANTIA.[69] All visualization involving crystal structures were carried out using VESTA.[51]

## 2.4 Results and Discussion

Preparation of the Conv. material through the solid state methods described previously results in a jet-black pellet, a dramatic color change from the unreacted starting materials. The black color was maintained upon grinding. The FD resulted in loose powder similarly displaying a black coloration. When handling these materials side by side, the FD was fluffy and light, as opposed to the denser Conv. material.

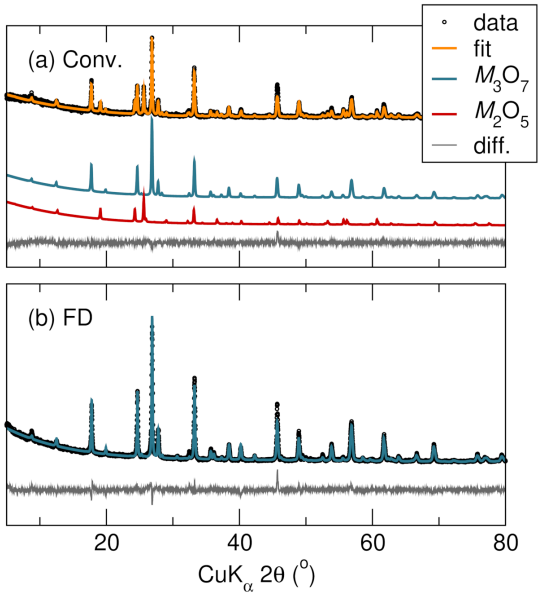


Figure 2.2: X-ray powder diffraction data for (a) the conventionally prepared material (labelled Conv.) and (b) the material prepared through the solution freeze-drying route (labelled FD), with the corresponding Rietveld fits to the appropriate crystal structure(s). The material made through the conventional route was refined to be 91 % of the target 3×3 block structure with the general formula $M_3O_7$ and 9 % the 4×4 block structure compound with the $M_2O_5$ formula in the same space group. The FD sample in (b) is single phase of the target 3×3 block structure. Refinement statistics can be found in the SI.

The structures were characterized with powder X-ray diffraction as shown in figure 2.2. Refinement statistics for both materials are included in the SI. After the first report of the $(W_{0.2}V_{0.8})_3O_7$ structure by Galy in 1964, solved from a single crystal, difficulties in the preparation of pure powders of the material have been reported.[29] After extensive optimization, the target crystal structure in the I4/$mmm$ space group could be obtained, containing 9 % of 4×4 Wadsley block defects. These defects are well established in the literature and commonly occur where some of the blocks have a different size than the main structure. [70, 71] The 4×4 block unit cell is presented in the SI. Because the fundamental structure and chemistry is unchanged with the small inclusion of the block defects, the analyses will not be significantly impacted. Particles obtained from the FD route yielded a single phase corresponding to the 3×3 structure as seen in figure 2.2(b). This phase pure sample was possible for a number of reasons, most notably, mixing stoichiometric solutions of aqueous precursors allows for mixing on the atomic scale, as opposed to mixing on micron-sized length scales associated with reactions between bulk oxide powders. It is additionally important to note that lyophilizing the solution provided a much finer control of the stoichiometry, due in part to the poor solubility of the V precursor. Flash-freezing prevents the precipitation of V that would otherwise occur due to poor solubility in water. Besides agreeing well with the single crystal structure of Galy[47], XPS survey scans and energy-dispersive x-ray spectroscopy measurements (figures presented in the SI) showed very close agreement of the measured V:W ratio to the expected ratio of 4:1.

Because solution-based methods provide diffusion pathways on the atomic scale, the FD preparation method allows for much shorter heating times compared to the Conv. preparation. Short calcination times equate to smaller particles seen in figure 2.3 where scanning electron microscopy reveals the Conv. particles to have a short

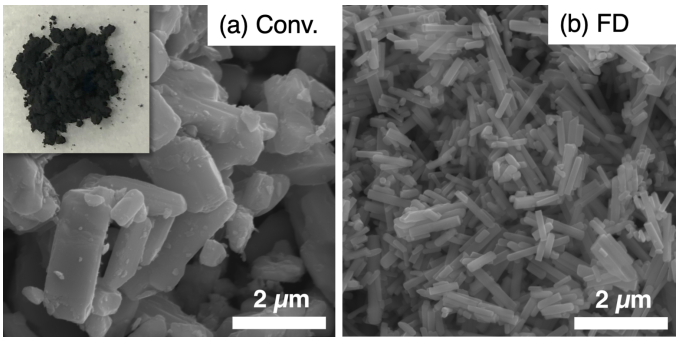


Figure 2.3: Scanning electron micrographs: (a) the conventionally prepared material (Conv.) displaying multiple-micron sized particles and (b) material prepared through the freeze-drying route (FD), displaying narrow lath-shaped particles up to a few microns in length but under 100 nm in width. A higher magnification image of the FD material can be found in the SI. The inset in (a) is a photograph of the as-prepared Conv. material showing the color associated with a partially filled $d$ band.

rod-like morphology on the order of 1 $\mu$m to 2 $\mu$m in the shortest direction. The inset of figure 2.3(a) shows the resulting jet-black powder upon grinding the pellet. Figure 2.3(b) shows how the FD preparation resulted in much smaller, rod-like particles about 100 nm in the shortest direction. A higher magnification of the FD particles is shown in the SI. The rod-like morphology is consistent with earlier transmission electron microscopy work on these compounds.[70]

Electrochemical lithiation revealed very comparable cycling between the Conv. and FD particles, and therefore the majority of the electrochemistry presented here focuses on the FD material. Additional electrochemistry of the Conv. material is included in the SI. At a C/5 rate on first discharge, more than 1 Li/TM is inserted. The impressive capacity retention by both large and small particles points to the crystal structure of $(W_{0.2}V_{0.8})_3O_7$ being conducive to the mobility of lithium.

Cyclic voltammetry was performed at different rates to determine an optimum voltage window for the electrochemistry, in addition to understanding the evolution of the redox peaks at varying sweep rates [Figure 2.4 (a)]. To avoid anomalous capacity

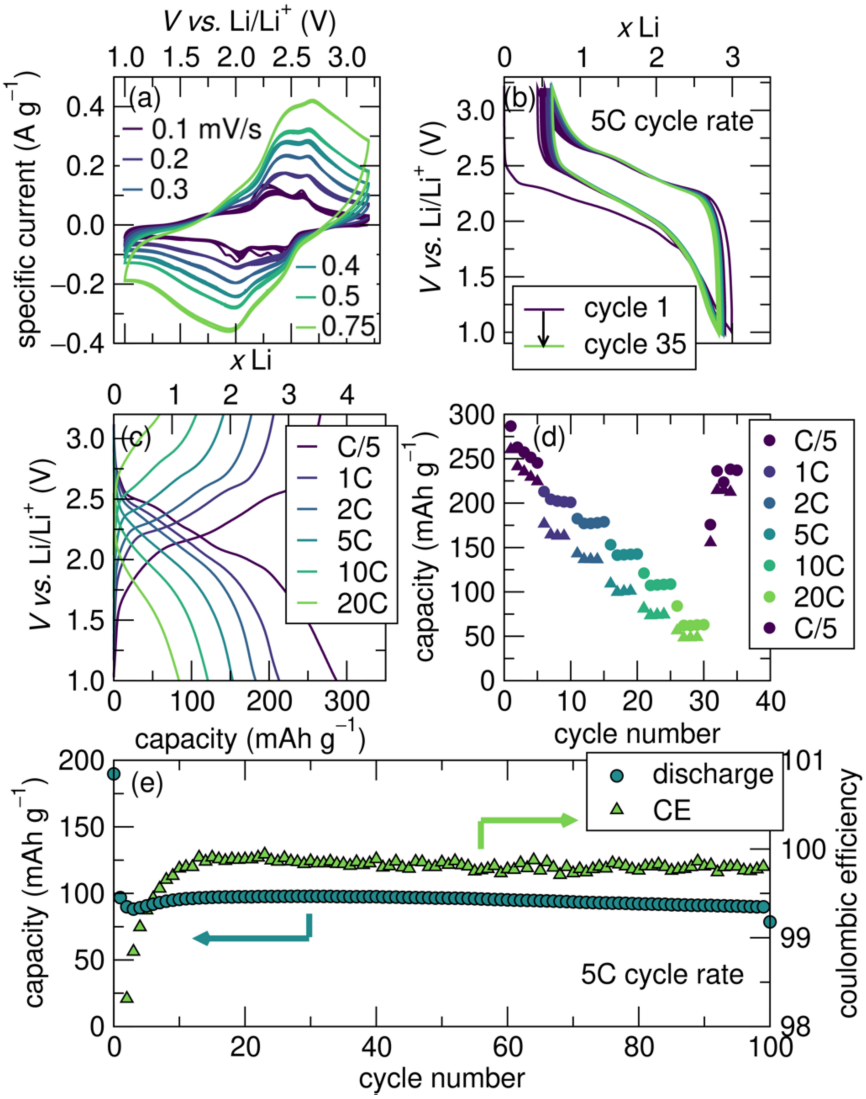


Figure 2.4: Electrochemistry of the FD $(W_{0.2}V_{0.8})_3O_7$ sample. (a) Variable rate cyclic voltammetry performed at sweep rates from 0.10 mV $s^{-1}$ to 0.75 mV $s^{-1}$. (b) Galvanostatic cycling at a 5C rate shows slight irreversible capacity loss after the first cycle and moderate polarization. (c) Galvanostatic cycling at rates from C/5 to 20C, and its recovery. (d) Summary of rate performance during discharge as a function of cycle number from data depicted in (c). Circles represent the FD material and triangles representing the Conv. material are displayed to compare rate performance between the different sizes of particles. (e) Extended cycling at a 5C rate. The FD material shows high capacity retention and Coulombic efficiency over 100 cycles.

contributions from lithium storage in carbon and electrolyte decomposition, a lower cutoff voltage of 1 V was selected. [72] Cyclic voltammetry reveals two major peaks on both reduction and oxidation. There is minimal redox activity until 2.4 V, where the first peak occurs, followed by an additional redox peak at 2 V. We note that the cyclic voltammetry reveals a significant amount of charge stored at potentials above 2 V, which differentiates this material from other, usually niobium-containing shear structures in the same family that typically store the majority of charge below 2 V.

Galvanostatic cycling at a 5C rate displayed in figure 2.4 (b) shows that after the first cycle, features of the discharge/charge curves are highly reproducible, with some capacity loss after the first cycle. The structure of the discharge curve displays three main regions, related to the trends we see in the cyclic voltammetry. At first, there is a steep voltage drop to 2.4 V where a small amount (0.25 Li) of lithium is incorporated into the structure. This leads to a small plateau that extends as a moderately sloping region until 2 V where 2.25 Li is inserted. Both of these redox events are consistent with the voltages observed from the cyclic voltammetry. The slope angles downward at this point until the 1 V cutoff where an additional 0.5 Li is incorporated. We observe moderate polarization between the discharge and charge curves.

The material exhibits impressive rate capabilities, demonstrated in figure 2.4 (c). At the slowest C/5 rate, we observe the three regions of the discharge/charge curves described earlier. As the cycling rate is increased to 20C, the discharge curve becomes smooth and sloping, and the bulk of the capacity is instead stored below 2 V, as opposed to the slower rates where more charge is stored above 2 V. Figure 2.4(d) compares the variable rate galvanostatic cycling of the small particles to the micron-sized particles. Upon returning to slow rates after more rapid cycling, both materials recover most of the capacity observed at the beginning of cycling. The large Conv. particles show

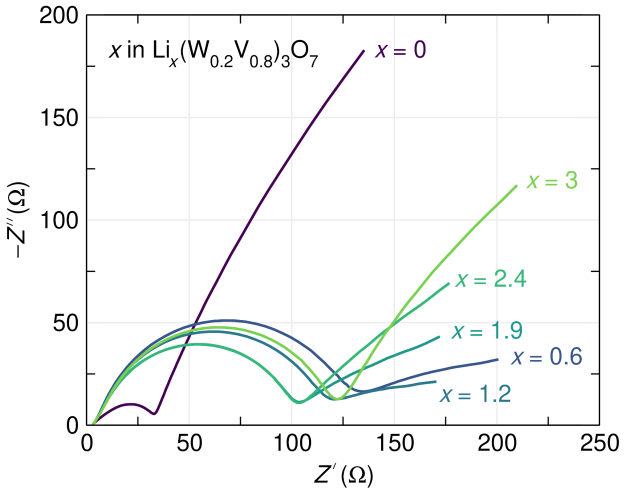


Figure 2.5: Electrochemical impedance spectra of $(W_{0.2}V_{0.8})_3O_7$ slurry electrodes as a function of Li content. The charge transfer resistance increases upon initial insertion of $Li^+$ but otherwise remains relatively constant at stoichiometries between $x = 0.6$ and $x = 3$ in $Li_x(W_{0.2}V_{0.8})_3O_7$. The spectra were collected on an electrode that had been previously cycled through galvanostatic rate testing so that initial SEI formation does not affect the data.

a comparable charge storage capacity at low and high rates, while the FD material shows the largest kinetic advantage at intermediate rates. As seen in figure 2.4 (e), $(W_{0.2}V_{0.8})_3O_7$ retains stable capacity at a 5C rate over 100 cycles.

Highly electrically conducting electrodes, or ones that turn into electrical conductors upon lithiation have the advantage of permitting fast cycling. Evidence for the effective electrical conductivity of $(W_{0.2}V_{0.8})_3O_7$ is seen from electrochemical impedance on the full cell. Potentiostatic electrochemical impedance spectroscopy was used to measure the charge transfer resistance of FD $(W_{0.2}V_{0.8})_3O_7$ slurry electrodes at different stages of lithiation (figure 2.5). The initial insertion of 0.6 $Li^+$ per unit cell results in an increase in the charge transfer resistance from about 30 Ω to 130 Ω. Additional lithiation results only in minor changes, and the electrode maintains a moderate charge transfer resistance of 100 Ω to 130 Ω up to insertion of 3 $Li^+$ per unit cell. These data suggest that the electrical resistivity of $(W_{0.2}V_{0.8})_3O_7$ remains reasonably low across the

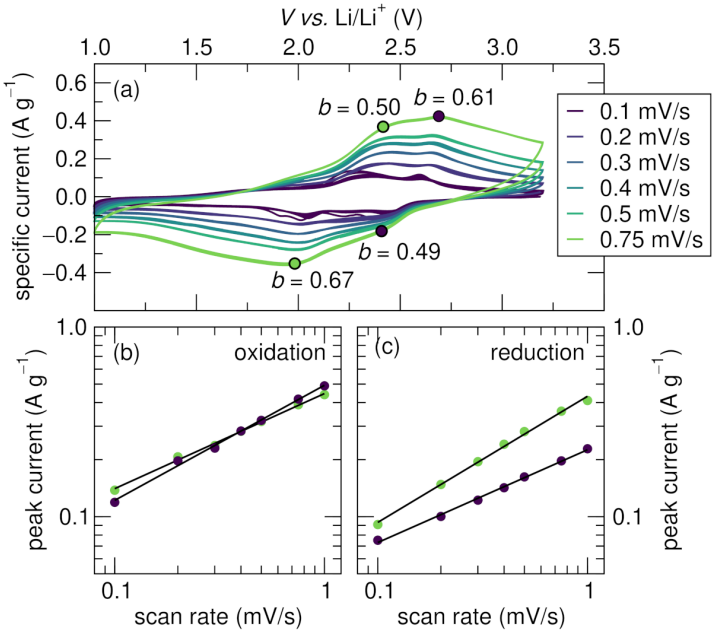


Figure 2.6: (a) Cyclic voltammetry of FD material at varying sweep rates, used to obtain the exponent $b$ for the different peaks in the voltammograms (indicated on the figure). (b) Power law fits for each oxidation peak based on the relationship between the scan rate and the current. (c) The corresponding fits for each reduction peak.

full range of electrochemical cycling.

In order to understand the nature of Li insertion and de-insertion, a kinetic study was carried out using the established relationship between the peak currents, $I_p$, in cyclic voltammetry to the voltage scan rate, $v$, through the power law: $I_p = av^b$, where $a$ and $b$ are constants. The exponent $b$ extracted for each redox peak is then indicative of the underlying diffusion mechanism, with $b = 0.5$ corresponding to semi-infinite diffusion, and $b = 1.0$ corresponding to a non-diffusion controlled process.[36, 73] $(W_{0.2}V_{0.8})_3O_7$ has two obvious redox peaks on both reduction and oxidation in the range of voltages scanned, as see in figure 2.6(a). By extracting the peak currents and fitting to the power law equation above, as demonstrated for the oxidation peaks in figure 2.6(b) and the reduction peaks in figure 2.6(c), the various values of the exponent $b$ are obtained, which are presented against the respective redox peaks in

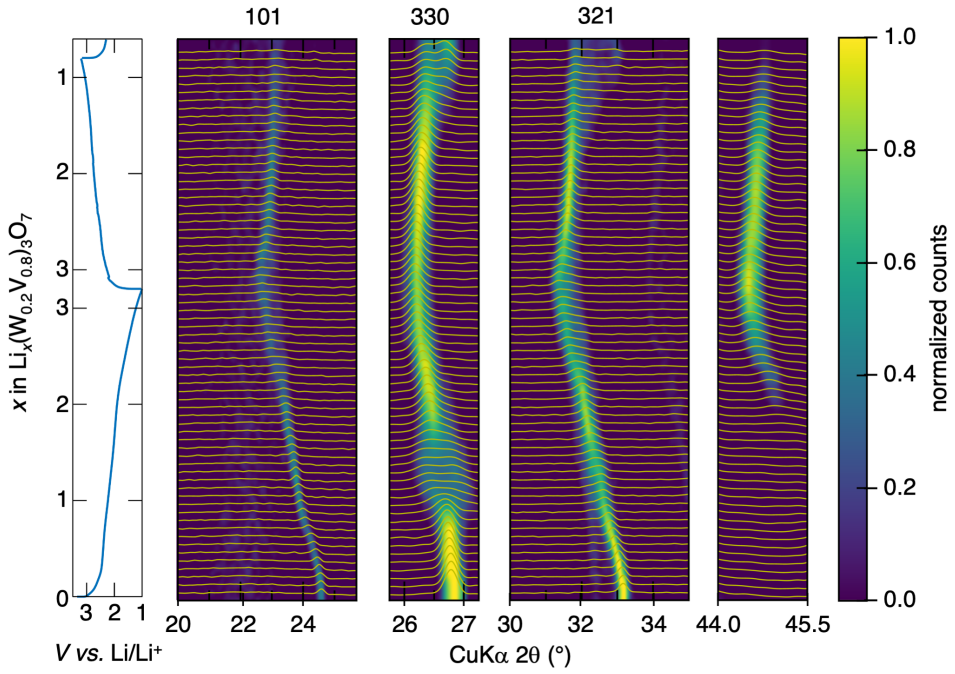


Figure 2.7: Select regions in the *operando* X-ray diffraction patterns of the FD $(W_{0.2}V_{0.8})_3O_7$ material during the first galvanostatic cycle at a rate of C/10. The corresponding electrochemistry is shown on the left most panel.

figure 2.6(a). The values of $b$ for all redox processes are close to 0.5, which indicates processes limited by bulk semi-infinite diffusion. This strongly points to the electrode materials storing charge though conventional electrochemical Li insertion rather than for example, capacitive storage taking place at the interface.

*Operando* X-ray powder diffraction of $(W_{0.2}V_{0.8})_3O_7$ performed at a C/10 rate provides insightful information about the evolution of the structure during lithium insertion and extraction. Select diffraction peaks during cycling are displayed in panels in figure 2.7. Data collected over the full $2\theta$ range is presented in the SI, along with a summary of the Rietveld refinements during lithiation. $(W_{0.2}V_{0.8})_3O_7$ appears to display mostly solid solution behavior. At the start of Li insertion and up to 1 Li/formula unit, a slight expansion of the unit cell is observed in the presented reflections. After this point, the (330) peak splits in the composition range between 1 Li per formula to

2 Li per formula. The peak splitting is attributed to the existence of a narrow two-phase region that then disappears above 2 Li per formula and then reappears on the following discharge cycle. Shortly after the disappearance of the peak splitting at (330), a new diffraction peak emerges at $2\theta \approx 45^\circ$. Along with the (110), (330), and (321) peaks that are tracked, this new peak similarly indicates unit cell expansion with increasing lithiation, followed by contraction as Li is removed. This feature indicates a phase change that disappears at the end of charge. At full discharge, the $a$ and $b$ planes expand by only 2.5 % while the $c$ plane expands by 6.4 %. We see an overall volume expansion of 13 %, in good agreement with previous chemical insertion on related compound $W_{0.2}V_{2.8}O_7$.[30] The refinements of the lithiated material are summarized in the SI as is the evolution of the cell parameters and cell volume with lithiation. The observed expansion on the basis of the number of electrons per transition element is relatively large compared with what has been observed in related Nb-rich oxides. This may in part help understanding why the high-rate cycling of $(W_{0.2}V_{0.8})_3O_7$ results in reduced storage capacity compared with compounds in the structurally related the Nb–W–O series.[39]

The structural evolution of this material seen through *operando* powder diffraction explicitly shows how $(W_{0.2}V_{0.8})_3O_7$ behaves as a battery material, in agreement with the analysis of the exponent $b$ in the variable-rate cyclic voltammetry. In the parent $ReO_3$ structure, Li conduction through the three-dimensional octahedral network is hampered due to rotation and tilting of the solely corner-connected octahedra. When there are edge-sharing features associated with crystallographic shear, rotation and tilting are prevented and Li transport is not impeded.[44, 74] However, the channels in the structure created by octahedral corner-sharing create highways for Li diffusion.

Both constituent transition metals are capable of multielectron redox, with a max-

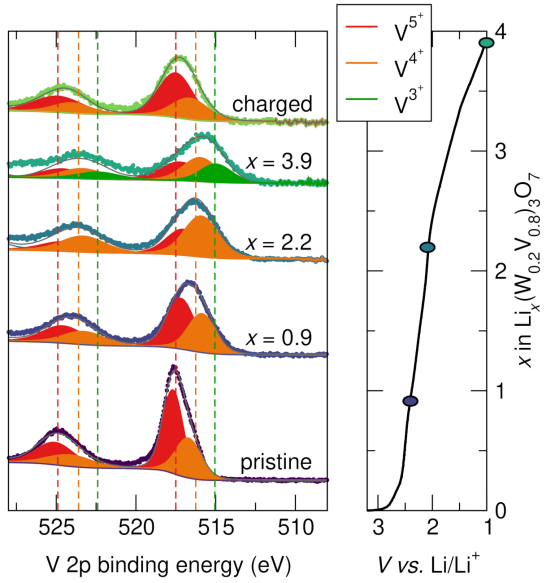


Figure 2.8: X-ray photoelectron spectra displaying the region of V $2p$ spin-orbit doublets $2p_{3/2}$ and $2p_{1/2}$ for the Conv. material. The total fit and contributions from the different oxidation states are indicated. On the right is the first galvanostatic discharge for Li insertion with the points indicating where the ex-situ XPS spectra were acquired.

imum theoretical capacity of 342 mAh $g^{-1}$ if 4.4 $e^{-1}$ are inserted (where we assume $W^{6+}$ reduces to $W^{4+}$, $V^{4+}$ reduces to $V^{3+}$, and $V^{5+}$ reduces to $V^{3+}$ ), based off initial oxidation states of the transition metals according to the equation $(1-y)V_2O_5 + (1+y)VO_2 + yWO_3 \rightarrow W_yV_{3-y}O_7$. Although this level of lithiation is not observed experimentally in the voltage ranges employed, the electrochemistry shows that 1.3 $Li^+$/TM are inserted at a C/5 rate, indicating that at least one of the transition metals is participating in a multielectron redox process. Ex-situ XPS allows this to be understood, however is not quantitatively relatable to the bulk oxidation states because of surface sensitivity to oxidation. Figure 2.8(b) and figure 2.9(b) display spectra at different states of charge for V and W respectively in the Conv. material. The pristine material appears to be a combination of $V^{5+}$ and $V^{4+}$ but only $W^{6+}$. As 0.9 Li inserts into the structure, further reduction of the $V^{5+}$ species to $V^{4+}$ is observed. After 2.2 Li inserts, the proportion of $V^{5+}$ to $V^{4+}$ inverts and the majority of V states are $V^{4+}$. At full discharge with insertion

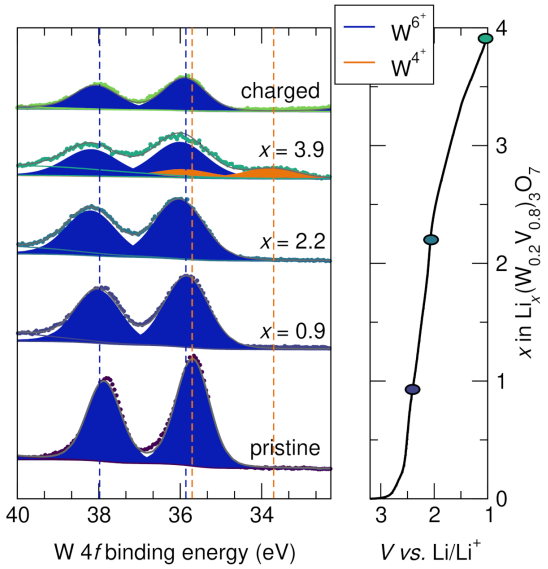


Figure 2.9: (left) X-ray photoelectron spectra of the W $4f$ binding energy region displaying the lower-energy W $4f_{7/2}$ and higher binding energy W $4f_{5/2}$ spin-orbit doublets. The grey line on each spectrum shows the total fit that combines the fits from each of the individual oxidation states. (right) First galvanostatic discharge for Li insertion into Conv. $(W_{0.2}V_{0.8})_3O_7$ material. States of charge corresponding to XPS spectra are overlaid on discharge curve.

of 3.9 Li, 27 % of the V is reduced to $V^{3+}$. Upon charge, the V oxidizes back to $V^{5+}$ and $V^{4+}$, but with a slightly higher ratio of $V^{4+}$ than observed in the pristine material. This could be attributed to part of the irreversible capacity loss seen after the first cycle.

In contrast to V, W reduction is quite different. W remains in its $W^{6+}$ oxidation state almost until full discharge where 23 % of the W is reduced to $W^{4+}$. There appears to be no evidence in the XPS signatures for any intermediate $W^{5+}$ state[75] which could suggest a tendency to valence-skip in this structure type. W returns to being fully oxidized after charging. These results confirm multielectron redox in both of the transition metals. As confirmed with XPS, the pristine $(W_{0.2}V_{0.8})_3O_7$ begins in a non-$d^0$ state due to a fraction of partially reduced V [figure 2.8 (b)]. This is what results in the compound, even prior to lithiation, displaying some evidence of electrical conduction and being black in color.

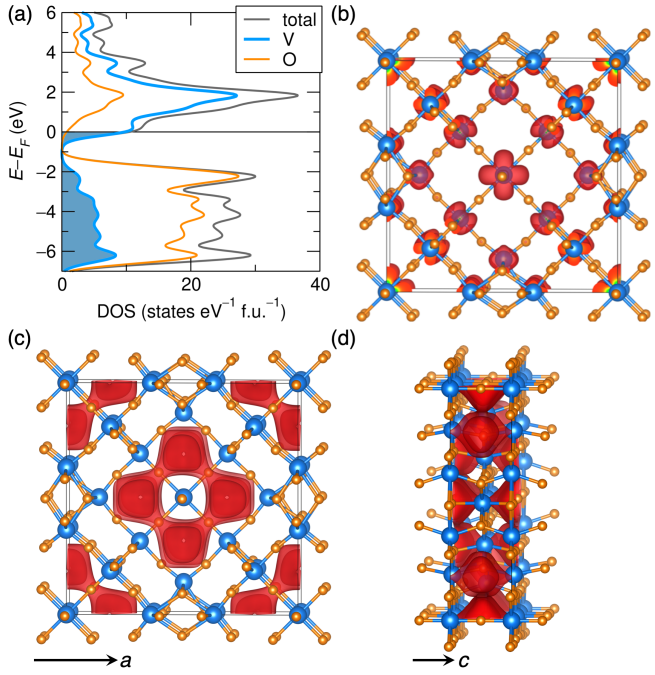


Figure 2.10: (a) Density of states for model compound $V_3O_7$ showing contributions from filled vanadium states at the Fermi level. (b) Charge density isosurface level of 0.005 e Å$^{-3}$ depicted within the unit cell of $V_3O_7$ showing the 1 d electron in the formula prefers the middle of the 3×3 block. (c) and (d) View of the bond valence difference map for Li in the space of the structure of $V_3O_7$ displayed for an isosurface value $\Delta v$ =0.1 valence units. The calculation of the DOS was made by Samuel M. L. Teicher.

As discussed above, although the samples were transferred from the glovebox using an air-free sample holder, some surface oxidation can occur which skews measurements towards higher oxidation states. This means that we cannot expect the XPS to quantitatively reflect the bulk oxidation state, but it should still be an excellent indication of the redox states present in the material as a function of Li content.

Density-functional theory-based electronic structure calculations are employed to provide qualitative understanding these 3×3 block structured materials as Li hosts. A complete analysis of the electronic structure of the parent $(W_{0.2}V_{0.8})_3O_7$ compound must account for the combination of electron correlation and disorder (the latter enhancing the former) which is beyond the scope of this work. However, calculations on the isostructural model compound $V_3O_7$ provide some useful insights. From the densities of state displayed for $V_3O_7$ figure 2.10(a), we see a combination of oxygen, but primarily transition metal states at the Fermi energy, arising from the formally, 1 $d$ electron for every three V, which is also consistent with what is observed in the XPS of the starting $(W_{0.2}V_{0.8})_3O_7$ compound. The as-calculated structure does not stabilize magnetization, even with the DFT simulations performed using the SCAN functional, which usually enhances magnetic localization. The partial charge density in figure 2.10(b) corresponds to a visualization of states in the energy range around $E_F$. The data suggests that the electron prefers the central metal site on an octahedron that is purely corner-sharing. This has also been noted in other shear phases, for example in $Li_xPNb_9O_{25}$ where the initial doped electrons localize (albeit magnetically in that case) on the central corner-connected octahedron.[42] As stated above, W/V substitution is likely to further hinder electron transport due to disorder and potentially yield some local moment behavior in the magnetism.

Bond valence mapping provides a simple means of estimating ion transport path-

ways and mechanisms for mobile ions placed arbitrarily within a 3D crystal structure. For each location in the 3D space of the structure, the absolute value of the difference $\Delta v$ between the valence calculated for the probe ion (here $Li^+$) at that site and its actual electrostatic valence (1 for $Li^+$) is mapped.[76, 77] It is possible to relate this valence difference $\Delta v$ to energies of defect formation and defect migration, allowing for rough predictions of the activation energy required for ion transport.[76, 77] Isosurfaces for a value of $\Delta v$=0.1 in valence units for the model compound $V_3O_7$ are displayed in panels (c) and (d) of figure 2.10. This isosurface illustrates probable 3D lithium migration paths in the structure. Empirically, it has been noted that the activation energy in eV is equivalent to approximately $2\times\Delta v$ in units,[78] so the displayed isosurface, forming channels down the $c$ axis of the structure, indeed suggests a low energy pathway for $Li^+$ migration. This is consistent with other, prior work showing in related shear structures that ion conduction occurs most rapidly in the center of the blocks in related shear structures.[79] $ReO_3$ has itself been shown to display an activation energy of migration for $Li^+$ of 0.1 eV,[80] which is in line with the values presented here. More detailed DFT studies to complement experimental investigations by impedance spectroscopy and NMR are necessary to establish the complete picture.[81]

## 2.5 Conclusion

Electrochemical insertion studies of $(W_{0.2}V_{0.8})_3O_7$ show that this vanadium-rich shear-structured Wadsley–Roth phase is a promising high-rate electrode material. While both the larger conventionally synthesized particles and smaller particles obtained by solution freeze-drying and calcination have capacity retention at up to 20C, there appears to be a clear advantage at all rates in having smaller particles. Distinct from other,

mostly niobium-containing shear structured compounds, the pristine material is a black powder that begins with some finite $d$ state population and therefore could be an intrinsically better electrical conductor than comparable $d^0$ oxides. Multielectron redox of both W and V lead to high specific capacities, while slight and reversible structural changes allow for capacity retention over one hundred cycles. This compound stores more charge at higher voltages than most other reported Wadsley–Roth compounds and points to promising directions for tuning the voltage in this high-performance class of electrode materials.

# Chapter 3

# Relating Crystallographic Features to Rate Performance in Wadsely-Roth Materials for Lithium-ion Batteries

## 3.1 Abstract

Wadsley-Roth shear structures represent a promising and high performance class of high-voltage Nb- and W-based anode materials that intrinsically avoid SEI formation, are capable of mulitelectron redox, and suppress large lattice expansion. Currently, there is huge momentum to design faster charging batteries. Wadsley-Roth materials, typically described by their block size, have been found to display outstanding charge storage at fast rates. Within this class of materials, however, there is significant diversity in terms of block size and block arrangement. It is understood that these materials as a class are all generally high performance, but what differentiates them between each other and why? Through data aggregation and visualization, we quantitatively

relate the role of shear to rate performance. We find that the structures which have block arrangements with lower amounts edge-sharing polyhedra are capable of higher capacity retention at fast rates. Our findings suggest there is an optimal threshold for the amount of shear for high-rate Wadsley-Roth materials, too little and the structure will have insufficient stability, too much and the structure will have insufficient channels for Li transport. We develop more nuanced understanding on the relationship between crystallographic features and high-rate properties, informing future material design strategies for fast-charging Li-ion batteries.

## 3.2 Introduction

Countless battery-reliant technologies will benefit by enabling faster charging cells.[4, 82] Charging Li-ion batteries at high currents requisite by fast charging is well known to lead to a snowball of undesired, potentially dangerous, and ultimately catastrophic consequences. These include, but are not limited to; functional fatigue,[18] lithium plating,[15, 16, 83] and dendrite growth.[84] Engineering the material morphology[19] and improving cell design are powerful tools to mitigate some of the aforementioned problems, but these engineering advances are exhausting the amount of possible improvement. There are often intrinsic and fundamental limitations dictated by the crystal structures of the active materials. At the atomic level, the crystal structure, combined with the constituent elements, ultimately determines the Li mobility,[85] electron mobility,[86] and the thermodynamically set potential.[20, 87, 88]

It is likely that more dramatic improvements in fast charging capabilities will stem from optimized crystal structures.[89] Other cell additives, such as polymer binders,[90] also stand to drive improvements in charge rate, but the active materials will continue

to remain as the critical limiting factors. Graphite anodes in particular are prone to dendrite growth[15, 16] and cell failure at fast rates,[91] mainly due to large volume changes[18] and low lithiation potentials.[72, 92] This has motivated the advancement of Wadsley-Roth shear structures as higher voltage anodes. These materials are a fascinating family of primarily Nb- and W-based shear structures that were first discovered in the 1960s[22–25] and have since experienced a large resurgence in research.[32, 33, 39]Notable advantages include a higher operating voltage that avoids SEI formation and the ability of Nb and W to exist in a wide range of oxidation states. This tolerance allows for coveted multi-electron redox, a hugely efficient means to increase the gravimetric capacity.

The Wadsley-Roth structures distinguish themselves crystallographically with their polyhedral connectivity, exemplified in Figure 3.1. Fundamentally, these materials are composed of corner-sharing $ReO_3$-type blocks, connected with edge-sharing planes of polyhedra. The $ReO_3$-type blocks create channels that impart a high Li-ion mobility, while the edge-sharing planes restrict polyhedral rotation and limit lattice expansion.[43, 93] Figure 3.1(a) showcases a $3 \times 3$ block structure, while Figure 3.1(b) shows a larger $4 \times 4$ block structure with an identical block arrangement. Figure 3.1(c) and Figure 3.1(d) illustrate the two types of edge sharing shear connectivity in this particular block arrangement. There is great diversity in terms of the size and arrangement of the blocks, which are mainly dependent on the precise composition. Broadly, the capacities and rate capabilities of these materials are exceptional, but it is challenging to understand mechanistic and performance differences between various compositions because the majority of studies on Wadsley-Roth materials focus on one or two specific materials.

Capitalizing on the wealth of data that has already been published on these ma-

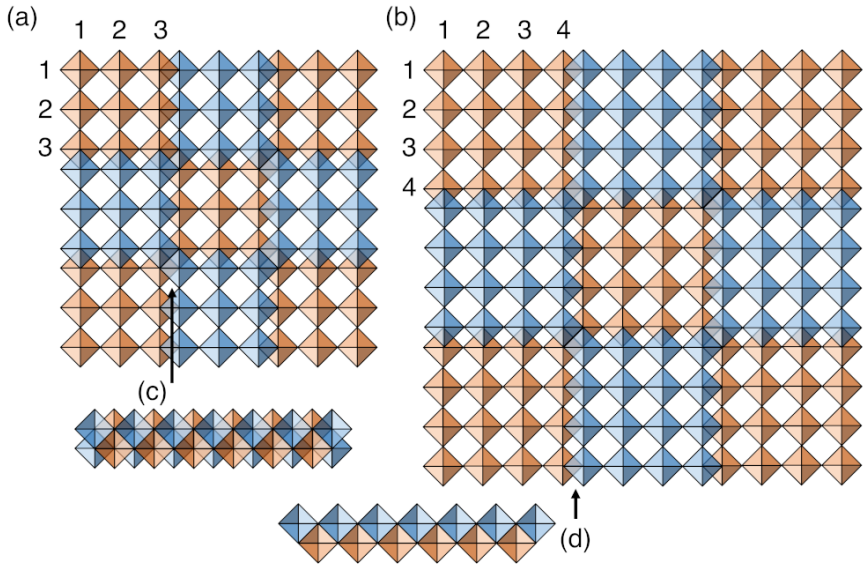


Figure 3.1: Schematic of two Wadsley-Roth shear structures comprising of (a) $3\times3\times\infty$ blocks and (b) $4\times4\times\infty$ blocks of corner-connected octahedra that are offset and connected with shear plans of edge-sharing octahedra. The two different colors used for the blocks of octahedra indicate that blocks are offset in the viewing plane. Both structures have identical block arrangements, and only differ in the size of the block, indicated on the top-left-most block of each structure. This particular block arrangement has two types of edge-sharing connectivity. A double-chain of edge-sharing octahedra are found at the block corners, illustrated in (c), and a single chain of edge-sharing octahedra are found at block edges and illustrated in (d).

terials, we aim to provide meaningful insight into performance and design principles through data aggregation and visualization. Comparison of the maximum experimental capacities shows that the majority of these materials are capable of multi-electron redox at slow rates, underscoring their overarching high gravimetric capacities. Although most structures in this family are referred to by their block size, we interestingly find that block size does not seem to be the most appropriate descriptor for differentiating their electrochemical performance. Instead, the data suggest that structures with a lower density of edge-sharing polyhedra (i.e. lower shear) are capable of higher capacity retention at fast charge rates. These findings suggest that there is a tradeoff between structural stability and Li diffusivity. It additionally underscores the important insights to be gained from understanding Li sites and filling preferences from first principles calculations. We quantitatively show the important relationship between crystal structure and rate performance, informing future design of intrinsically fast-charging materials.

## 3.3 Experimental Methods

### 3.3.1 Data Digitization

All data featured in this work were manually extracted from the literature.[94–113] Publications were selected through a series of extensive literature searches in an effort to ensure cohesiveness between material preparations and reasonable electrochemical testing protocols. For example, the electrode mass loadings from all data sources fall into a similar range, summarized in the Supplementary Information (SI). For each publication, six descriptors were extracted; 1) the electrode mass loading, 2) electrode

area, 3) electrode compositions, 4) particle sizes, 5) Wadsley-Roth block dimensions, and 6) maximum experimental capacity. Additionally, variable rate cycling data were extracted from figures using the WebPlot-Digitizer program.[114] Maximum experimental capacities were recorded from the second cycle capacity, to ensure irreversible losses from the first cycle are accounted for in the overall results.

To compare the relative capacity retention from increasing cycling rate, the percent capacity retained between 1C and 10C cycling rates were calculated for each compound. If data for these two specific rates were not available in a publication, capacities were interpolated using a linear regression model of the natural log of gravimetric capacity versus C rate.

### 3.3.2 Quantifying Structural Features

To quantify structural features, crystallographic information files (.cif) were analyzed using the Python package Pymatgen. For calculating structural packing efficiencies, an average coordination number for each ion type was calculated from the crystal structure. The average oxidation state of each ion type was calculated through Pymatgen. The overall packing efficiency for each structure was obtained through linear interpolation of tablulated Shannon-Prewitt ionic radii, using the average oxidation state and average coordination number of each element.

Edge sharing density for each structure was calculated by dividing the number of polyhedral edge sharing features by the unit cell volume. The nearest neighbor anions to each cation were obtained by Pymatgen's CrystalNN algorithm; one edge sharing feature was counted for each pair of cations that shared two nearest neighboring anions. Periodic boundary conditions were used to capture inter-unit cell edge sharing on

all faces of a single unit cell. These values were confirmed through manual counting of edge-sharing features in a unit cell for a select number of materials.

### 3.3.3 Calculating Theoretical Capacities

The theoretical one- and two-electron capacities of each material were calculated to compare with experimentally measured capacities. Experimentally accessible oxidation states for each transition metal were referenced from published Shannon-Prewitt radii. The one-electron theoretical capacity was obtained by accounting for one electron for each redox-active transition metal species. Similarly, the two-electron theoretical capacity was obtained by accounting for two electrons for each redox-active transition metal that was capable of multielectron redox.

## 3.4 Results and Discussion

Although Wadsley-Roth materials all share the same two basic corner- and edge-sharing octahedra features, there is still great diversity regarding the constituent elements and block arrangements in this material family. A subset of these materials are presented in Figure 3.2. Figure 3.2(a) shows the precise crystal structure and composition used to derive the Wadsley-Roth schematic in Figure 3.1(a). $(W_{0.2}V_{0.8})_3O_7$ has the highest operating voltage in the Wadsley-Roth family. A notable subgroup of Wadsley-Roth materials contain both W and Nb, and one composition from this subgroup is displayed in Figure 3.2(b). Figure 3.1(c) shows $TiNb_2O_7$, one of the most thoroughly studied Wadsley-Roth materials and first known material in this class to be commercialized.[5, 115] Figure 3.1(d) displays $PNb_9O_{25}$, an example material that

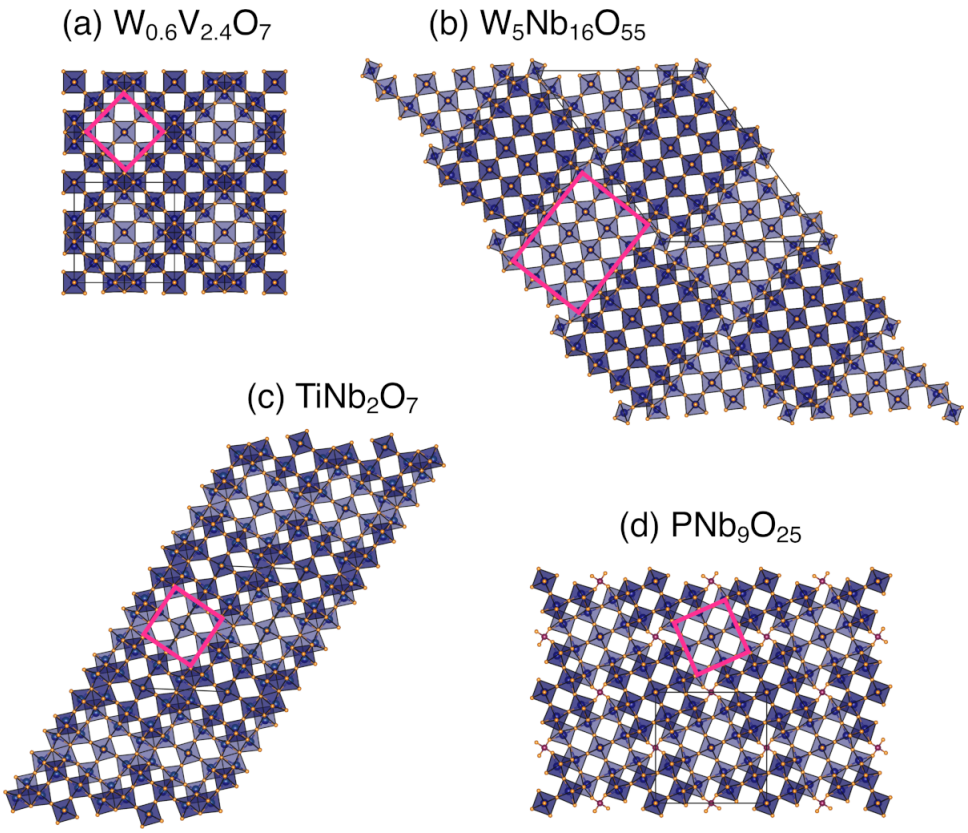


Figure 3.2: Example crystal structures from the Wadsley-Roth family including (a) $(W_{0.2}V_{0.8})_3O_7$ (b) $W_5Nb_{16}O_{55}$ (c) $TiNb_2O_7$ and (d) $PNb_9O_{25}$.

contains both a non-redox-active element and a block arrangement that includes a tetrahedral site. These structures do not encompass all possible crystallographic arrangements, but are used used here to broadly highlight subsets of the class generally.

The voltage profile of a lithium ion electrode material provides important insight to the underlying chemistry. The voltage profiles for fifteen different Wadsley-Roth materials were extracted from published literature at both slow and fast rates, and displayed in Fig. 3.3. Fig. 3.3(a) shows an overlay of the voltage profiles as a function of capacity. At slow rates, we see that despite variances in crystal structures and chemistries, the voltage curves nearly collapse onto a shared profile. Generally, as lithium is inserted into these materials, the voltage drops rapidly to 1.7 V, is then followed by an

extended shoulder region, and then concludes with a sloping voltage profile until the lower voltage cutoff. The ubiquitous nature of the Wadsley-Roth discharge curves be rationalized from two standpoints. First, the electrochemical redox is dominated by Nb redox couples for the majority of these materials and so we would expect similar operating voltages. Second, the similarity in the structure of the discharge curves is likely due to the fact that these materials are comprised of similar crystallographic building blocks with akin lithium sites and lithium filling preferences. Notably, one slow rate voltage curve deviates from this trend and sits approximately 1 V higher than the others. That voltage curve belongs to one of the few Wadsley-Roth materials that does not contain Nb, namely $(W_{0.2}V_{0.8})_3O_7$, studied through *operando* calorimetry[116] for its high rate cycling capabilites. [117] All of the reported materials have notably large capacities at slow rates that fall between 200 mAh $g^{-1}$ and 300 mAh $g^{-1}$. At faster cycling rates, the discharge curves largely retain the same three distinguishable regions seen during slow cycling rates, albeit curtailed with lower overall capacities. The resemblance between the discharge curves at both slow and fast cycling rates points to the overall effectiveness of these materials as outstanding high rate electrode materials.

Retained capacity is generally considered the accepted figure of merit for battery electrode materials. However, for the same set of overlaid discharge curves, we also show the data as voltage versus Li per redox active transition metal in Fig. 3.3(b). Nb is stable in an octahedral coordination environment as $Nb^{5+}$, $Nb^{4+}$, and $Nb^{3+}$. Wadsley-Roth materials are generally comprised of $Nb^{5+}$ in the pristine materials, allowing for possible reduction of two valence states down to $Nb^{3+}$. This type of flexibility in oxidation states permits for so-called multi-electron redox, where more than one lithium ion can be inserted per transition metal, leading to significantly higher capacities than typical electrode materials that are not capable of reversible reduction by more than one

valence state. Fig. 3.3(b) highlights the ability of these materials to store more than one lithium per redox active transition metal at slow cycling rates. At fast rates, these materials are still able to store between 0.5 to 1 lithium per redox active transition metal. Although the maximum capacities at slow rates fall into a fairly narrow range, we note that there is a more noticeable spread in maximum capacities at fast rates. There are crystallographic features that likely play more nuanced and important roles with diffusion kinetics, manifesting more readily at faster cycling rates. We explore this topic later in the text.

The maximum experimental capacities of various Wadsley-Roth materials are presented in Fig. 3.4, along with their corresponding theoretical one- and two-electron capacities. The materials are ordered from left to right by highest two-electron theoretical capacity. The theoretical capacities of nearly all of the reported Wadsley-Roth materials are close to 400 mAh $g^{-1}$. The reported maximum experimental capacity for each material is overlaid as a black point on each bar. We find that many of these materials have been shown to store over one electron per transition metal, although not all. For example $VNb_9O_{25}$ is calculated to have the highest theoretical capacity based off two electrons per transition metal. However, it has been found to experimentally store less than one electron per transition metal. Interestingly, isostructural $PNb_9O_{25}$ is capable of storing significantly more.[42] The notably poor experimental capacity of $TiTa_2O_7$ can be attributed to irreversibility in Li insertion.

$TiTa_2O_7$ stands out as having both the lowest theoretical and experimental capacity, although it is isostructural with $TiNb_2O_7$, one of the highest capacity Wadsley-Roth materials. At a C/5 cycling rate, $TiTa_2O_7$ and $TiNb_2O_7$ allow for the initial insertion of 4.2 and 4 Li ions per formula unit respectively. The reversible capacity, however, shows that $TiTa_20_7$ can reversibly insert only 2.25 Li per formula unit, compared to 3

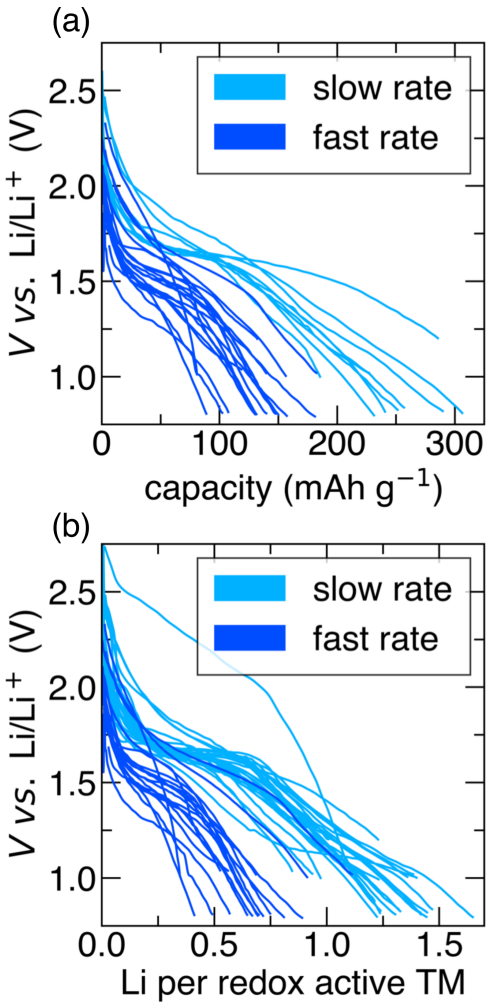


Figure 3.3: Discharge profiles of various Wadsley-Roth phase compounds obtained from literature, plotted against gravimetric capcacity (a), or Li inserted per redox-active transition metal (b). Here, slow rate denotes 0.1C and fast rate denotes 10C; 1C and 5C were respectively substituted if data for 0.1C or 10C rates were not published.

for $TiNb_2O_7$. Compilation of this data more readily shows key differences in maximum charge storage for related materials.

It is important to note that although great care was taken to ensure the comparability of experimental conditions between electrochemistry studies, these data come from different research groups and therefore the insight we aim to draw is more qualitative in nature. Theses materials are mainly based on the same Nb redox couple, and so it is likely that the differences in electrochemical performance instead stem from crystal structure variations. By strategically comparing compiled electrochemistry data to crystallographic structural information, we aim to better understand why some materials perform better than others, in order to develop design strategies in this promising class of anodes. Because all Wadsley-Roth materials are built from the two main crystallographic motifs outlined in Figure 3.1, we have adopted a method to quantitatively account for these motifs.

It is well understood that sufficient Li channels or percolation pathways are critical for facile ion mobility. The corner-connected $ReO_3$-type block component in these structures creates a relatively open structure with clear channels. To compare the "openness" of the various crystal structures, we calculate the packing efficiencies of each as a type of proxy for the relative ease of ion transport. Our results show that the Wadsley-Roth structures all have similar packing efficiencies, with a mean of 28.2% and a standard deviation of 0.7%. To account for the edge-sharing features in these crystal structures, we define a metric termed "edge-sharing density" that quantifies the number of edge-sharing features per volume. As opposed to the nearly universal agreement in packing efficiency, the edge-sharing density metric shows much greater variation between crystal structures, with a mean of 7.5 edges $m^{-3}$ and standard deviation of 4.7 edges $nm^{-3}$. These data are plotted in the SI. We note that $GeNb_{18}O_{47}$ strongly deviated from this

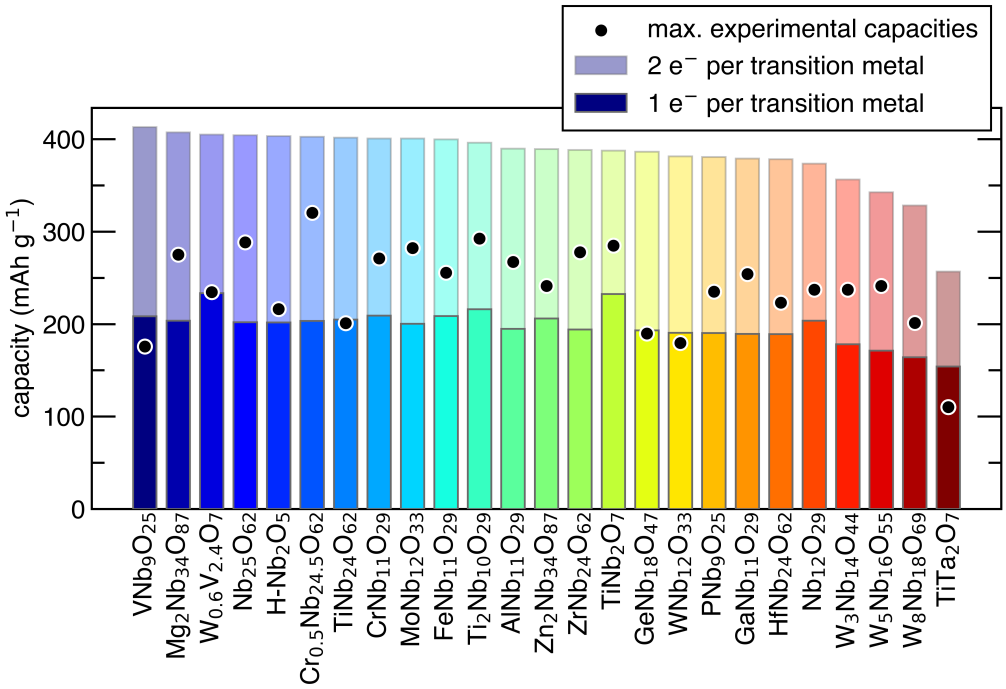


Figure 3.4: Published maximum experimental capacities of various Wadsley-Roth materials, overlaid on one-electron maximum and two-electron maximum theoretical capacities.

mean (statistical outlier with 95% confidence) due to unique tight-packed Ge-O metal clusters at the corners of tiled sections. These data suggest that there are clearly differences in the amount of edge-sharing features in the Wadsley-Roth family, and that those features are not significantly impacting the "openness" of the crystal structure.

The electrochemical performance of these materials at slow rates do not show obvious differences from their maximum reported experimental capacities. Because Wadsley-Roth materials are championed for their unusually remarkable fast charging capabilities, differentiating their performance will center around analysis of high C rate electrochemistry. Figure 3.5(a) shows the capacity retention at a one hour charge rate (1C). We find that there is a larger spread in capacity retention than from slower rate

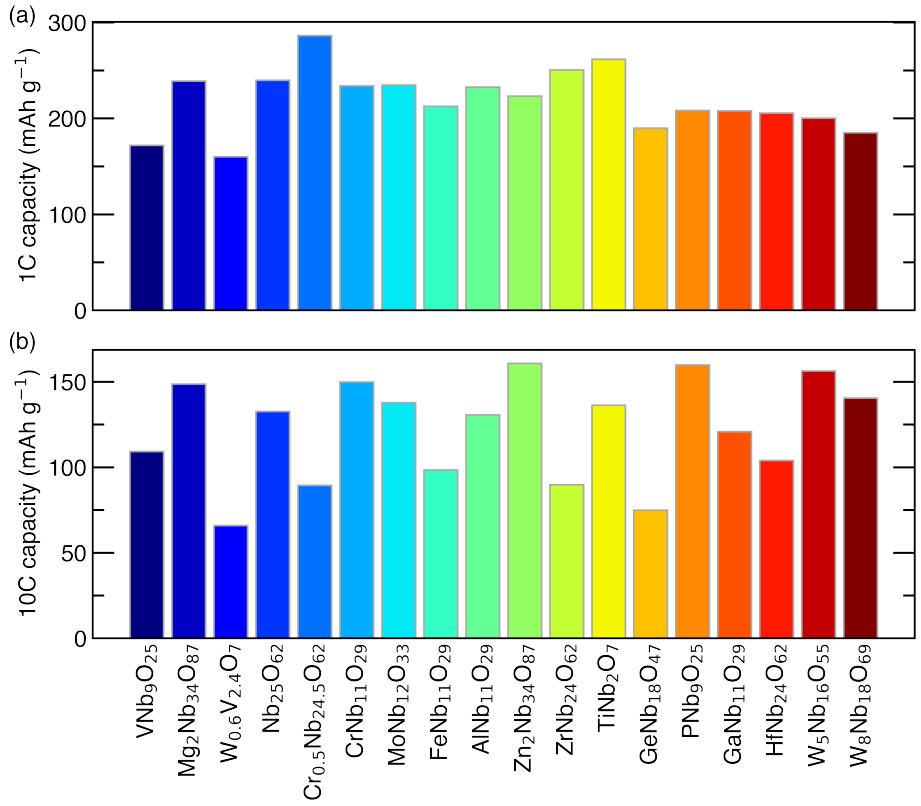


Figure 3.5: Published experimental capacities of various Wadsley-Roth materials at (a) a 1 hr (1C) cycling rate and (b) a 6 min (10C) cycling rate.

cycling, but it is still difficult to tease out convincing distinctions between materials. Instead, differences in absolute capacity retention are more apparent when comparing their capacity retention at a six minute charge (10C) in Figure 3.5(b). At this much faster cycling rate, these data show a more sizable spread in absolute gravimetric capacity.

### 3.4.1 Capacity retention to evaluate performance

Capacity differences at moderate 1C and faster 10C rates for this set of materials provide valuable information when comparing absolute numbers, but quantitative con-

clusions relating crystal structure to electrochemical performance is more limited because these data were collected from a variety of different research groups. In an effort to more confidently link crystallographic features to electrochemical performance, we define a normalized metric that is self-consistent from an experimental perspective. We calculated a "Capacity Retention %", namely a percentage difference in capacity from the 1C and 10C cycling rates. In this way, we can better compare the intrinsic quality of rate performance between materials, which was not possible by solely looking at the absolute capacity values. Those absolute values convolute both small discrepancies in experimental methods between groups and slight differences in each materials' theoretical capacity. Capacity retention as a percent value does not tell us definitively what the "best" material is, but it can give us an indication of what crystallographic features may contribute to more optimal rate performance. This understanding is important to draw more nuanced insight into design principles for Wadsley-Roth materials which have been largely overlooked.

As mentioned previously, the most common descriptors used to structurally differentiate Wadsley-Roth materials are the block dimensions and block arrangement. Block size is an extremely important way to understand and concisely describe crystal structures within the Wadsley-Roth family, giving critical information about these structures such as the number of channels and transition metal connectivity. Figure 3.6 shows, however, that block size alone is an insufficient metric to explain the large range observed in percent capacity retention from 1C to 10C. We are partially restricted by the relatively limited number of materials within this family, but also a strong propensity for certain block sizes for the materials that are reported. Looking only at the extremes in percent capacity retention, we see that the two largest block size materials, $Nb_{16}W_5O_{55}$ ($4 \times 5$) and $Nb_{18}W_8O_{69}$ ($5 \times 5$), represent the materials that have the high-

est percent capacity retention between their 1C and 10C cycling rates. On the other hand, one of the $3 \times 3$ block structures, $GeNb_{18}O_{47}$, has the lowest percent capacity retention. Despite these clear extremes, the intermediate data show large spreads for the same $3 \times 3$ and $3 \times 4$ block sizes. Within the same category of $3 \times 4$ block size, there is a range in capacity retention of 30%. Previous literature has asserted that large block sizes result in high $Li^+$ diffusion[45], however these data show that certain compositions with smaller block sizes can have comparable capacity retention to larger block sizes. For example, $3 \times 3$ block structure $PNb_9O_{25}$ has an identical percent capacity retention to $5 \times 5$ block structure $Nb_{18}W_8O_{69}$. Because of the factors mentioned previously regarding the size and scope of our data set, we are motivated to look beyond block size to find a structural descriptor that can provide more meaningful insight as to understanding why some materials have better intrinsic rate performance than others.

Wadsley-Roth materials are distinguished by their block size, but block arrangement can be equally important for differentiating materials. Block arrangement can have important implications for the polyhedral connectivity, types of crystallographic sites (including tetrahedral sites), and importantly, the amount of shear and edge-sharing features. As discussed previously, there is a large range in the edge sharing density in these materials. Figure 3.7 shows the percent capacity retention plotted against the edge sharing density. These data show a compelling trend emerge, emphasizing the importance of determining a structural descriptor that more broadly encompasses the richness of the structural diversity in these materials. The materials representing the extreme data points in this plot are consistent with the extremes in Figure 3.6, but now the intrinsic rate performance of materials within the same block size category can be better rationalized. We find an inverse correlation between percent capacity retention and volumetric edge sharing density. The trend shows that materials with a lower edge-

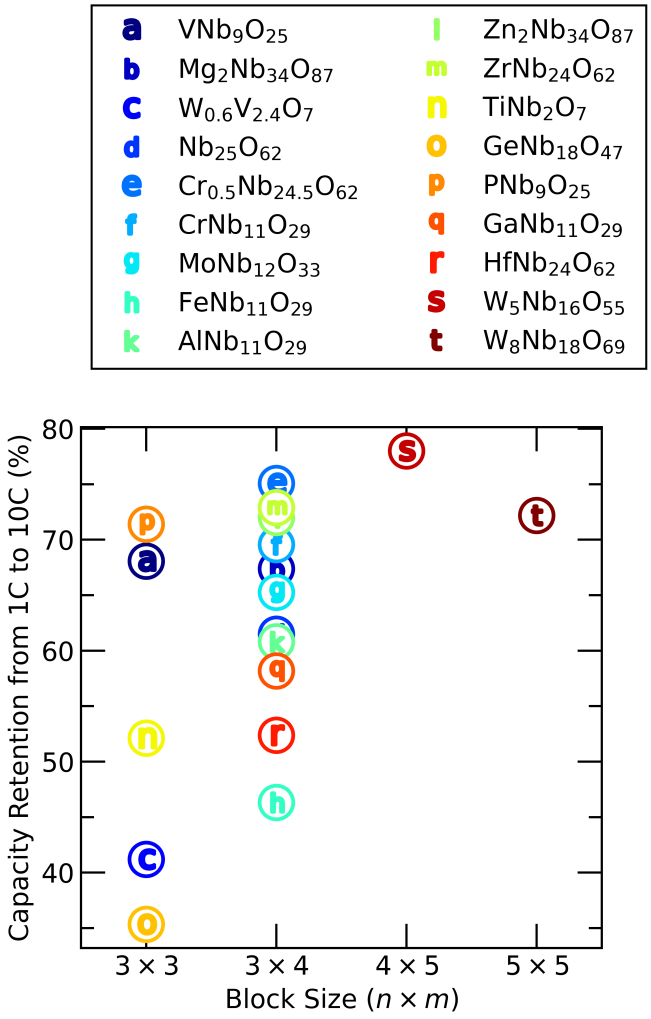


Figure 3.6: The percent capacity retained between 1C and 10C cycling rates for various Wadsley-Roth materials, plotted against the Wadsley-Roth block size.

sharing density generally have a higher percent capacity retention from a 1C to 10C cycling rate. Capacity retentions of greater than 60% were limited to materials with less than 7 edges shared per $nm^3$. $Nb_{16}W_5O_{55}$ was found to have a percent capacity retention of nearly 80%. That is, this material is capable of storing a similar amount of charge in one hour as it can in six minutes. We also see that $GeNb_{18}O_{47}$ had the largest edge sharing feature density of all calculated compounds, corresponding with the lowest percent capacity retention.

### 3.4.2 A note on nanostructuring

The percent capacity retention metric also offers valuable insight into the benefits of nanostructuring Wadsley-Roth materials. Nanostructured Wadsley-Roth materials are frequently investigated as a means to improve electrochemical performance, especially for high-rate cycling. When the percent capacity retention from 1C to 10C for bulk and nanostructured materials are compared, we find that for a given material chemistry, nanostructured morphologies typically yield a 10% to 20% increase to capacity retention, relative to their bulk counterparts. These data can be found in the SI. However, it is clear that nanostructuring is not necessary in order to achieve high capacity retention. Both bulk and nanostructured materials are capable of capacity retentions of 75%. As previously reported for individual materials, we confirm with a larger data set that impressive cycling performance is achievable without complicated nanostructuring processes.

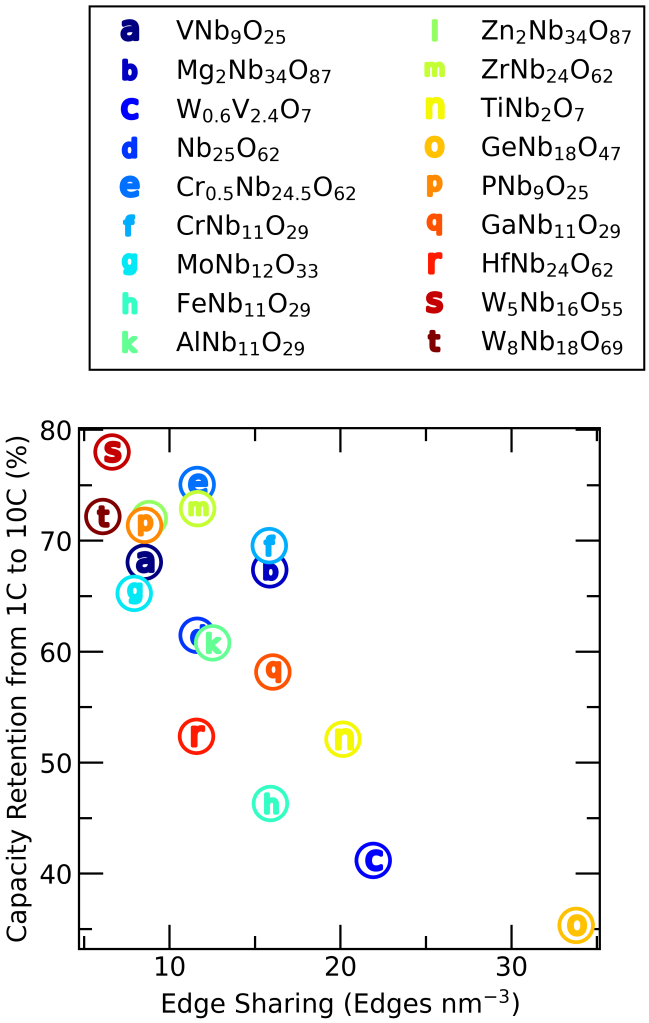


Figure 3.7: The percent capacity retained between 1C and 10C cycling rates for various Wadsley-Roth materials, plotted against the calculated density of crystallographic edge-sharing features.

## 3.5 Conclusion

Materials in the Wadsley-Roth family are exciting candidates for lithium-ion battery anodes, due to their high capacities and fast-charging capabilities. The high capacities of these materials are a direct reflection of their ability to undergo multielectron redox. Similarities in their voltage plateaus are indicative of related underlying charge storage mechanisms. Despite similar charge storage mechanisms, we have shown that there are measurable differences in their fast-charging capabilities, notably when comparing the capacity retention percent between 1C and 10C. We find that although block size is generally an important descriptor from a crystallographic perspective, it does not sufficiently capture other key crystallographic attributes that result from unique block arrangements. By defining a new metric that we term edge-sharing density, we show that the capacity retention percents from 1C to 10C increase with decreasing edge-sharing density. Further work is necessary to more completely develop our understanding of this finding, likely stemming from Li diffusion kinetics and filling preferences. By analyzing experimental electrochemical data of Wadsley-Roth materials, we find that the relative amount of edge-sharing features directly influences the rate performance, providing a clear design strategy when selecting and developing fast-charging electrode materials.

# Chapter 4

# Metal-Metal Bonding as an Electrode Design Principle in the Low-Strain Cluster Compound $LiScMo_3O_8$

## 4.1 Abstract

Electrode materials for $Li^+$–ion batteries require optimization along several disparate axes related to cost, performance, and sustainability. One of the important performance axes is the ability to retain structural integrity though cycles of charge/discharge. Metal-metal bonding is a distinct feature of some refractory metal oxides that has been largely underutilized in electrochemical energy storage, but that could potentially impact structural integrity. Here $LiScMo_3O_8$, a compound containing triangular

Reproduced with permission from K. E. Wyckoff, J. L. Kaufamn, S. W. Baek, C. Dolle, J. J. Zak, J. Bienz, L. Kautzsch, R. C. Vincent, A. Zohar, K. A. See, Y. M. Eggeler, L. Pilon, A. Van der Ven, and R. Seshadri. Metal-Metal Bonding as an Electrode Design Principle in the Low-Strain Cluster Compound $LiScMo_3O_8$ *J. Am. Chem. Soc.* 144(13), 5841–5854 (2022). 

clusters of metal-metal bonded Mo atoms, is studied as a potential anode material in $Li^+$—ion batteries. Electrons inserted though lithiation are localized across rigid $Mo_3$ triangles (rather than on individual metal ions), resulting in minimal structural change as suggested by *operando* diffraction. The unusual chemical bonding allows this compound to be cycled with Mo atoms below a formally +4 valence state, resulting in an acceptable voltage regime that is appropriate for an anode material. Several characterization methods including potentiometric entropy measurements indicate two-phase regions, which are attributed through extensive first-principles modeling to $Li^+$ ordering. This study of $LiScMo_3O_8$ provides valuable insights for design principles for structural motifs that stably and reversibly permit $Li^+$ (de)insertion.

## 4.2 Introduction

Improving reversibility and lifetime of $Li^+$–ion electrode materials necessitates understanding structure-property relationships in electrode materials.[87] Increasing reliability and performance is imperative towards broader adoption of $Li^+$–ion battery-reliant technologies such as electric vehicles and portable electronics.[4, 82] The poor cycle life of active materials in $Li^+$–ion batteries is often associated with structural degradation of the electrode.[118] The surface of a typical active material develops an interphase, that can evolve during cycling and contribute to irreversible $Li^+$ loss.[119] Particles fatigue over time from repeated expansion and contraction of the structure with lithiation and delithiation, respectively.[120] Repeated volume changes induce strain, causing particle cracking and lead to myriad issues, including contact and porosity loss, that negatively impact charge and ion transport.[121, 122] The interphase degradation mechanism is significantly amplified with cracking since it additionally

forms on all freshly exposed surfaces.[123] These serious failure mechanisms have motivated efforts to directly probe compositional and structural responses through scanning transmission electron microscopy[124] and strain measurements.[125] Even the promising Ni-rich layered cathode systems such as NMC811 suffer from degradation processes attributed to high interfacial lattice strain between the surface and bulk of the structure.[126]

Strategies to mitigate this type of failure mechanism vary widely, but all center around the principle of minimizing large volume changes during cycling. Engineering the electrode morphology has been shown to be successful at preventing lattice strain through using an intergrown rocksalt structure in a layered cathode.[127] Improved polymer binder design is also being explored.[128, 129] Nanoscaling particles[8, 11, 130] and optimizing disorder[131] have been established as ways to suppress phase transitions and circumvent the innate volume expansion of certain crystal structures. Normally, delithiation of $LiCoO_2$ intrinsically causes a significant expansion of the $c$ lattice parameter.[132, 133] Judicious doping of certain materials, such as Al in $LiNi_{1-x}Al_xO_2$, is suggested to be effective at preventing large volume changes.[134]

Fast charging capabilities are highly desirable, but rapid $Li^+$ insertion can exacerbate particle cracking.[18] Efforts to improve ion transport include nano-structuring the active material through high energy ball milling or optimized synthetic routes to decrease $Li^+$ ion diffusion distances.[6, 7, 19] Carbon coating is used to improve electron transport between particles.[12] Although these approaches for both mitigating volume expansion and improving transport can be very effective, they mask the undesirable properties associated with the crystal structure itself. It is critical then to understand and identify crystallographic motifs on the atomic scale that intrinsically provide both good ion and electron transport pathways, while maintaining a rigid structural

framework that prevents significant lattice expansion.

Crystallographic shear phases, including the Wadsley-Roth structures[23, 24, 32, 135, 136] possess crystallographic shear and have emerged as a promising and broad class of materials that display exemplary performance as electrodes. These materials are diverse in elemental constitution and block size, and even large particles of these materials are capable of impressive rates. [33, 37–40, 42, 45, 117, 137–140] Computational and experimental efforts have suggested that a combination of corner and edge-sharing polyhedra promote metallic conductivity and fast $Li^+$–ion diffusion, while suppressing large structural changes.[43, 74, 93]

In this work we seek to explore other kinds of structural motifs that allow stable and reversible capacity retention. We turn to oxide compounds of Mo, the chemistry of which is varied and rich, in part because Mo is able to exist in a wide range of oxidation states, coordination geometry, and structural motifs.[141–143] Some of the first ternary oxides of $Mo^{4+}$ were reported in 1957, with Mo–Mo bonding in triangular $Mo_3$ clusters and the formula $A_2^{II}Mo_3^{IV}O_8$, with the wide range of divalent cations Mg, Mn, Fe, Co, Ni, Zn, and Cd.[144] $LiScMo_3O_8$, the compound studied here, was discovered while exploring the possibility of using a monovalent and trivalent ion to replace two divalent cations.[145] Postulated site preferences based on cation charge and size in this series were confirmed from structural studies.[146, 147] This $LiRMo_3O_8$ class of materials has garnered somewhat limited attention for $Li^+$ insertion, with electrochemical studies on the structural analogues $LiHoMo_3O_8$[148] and $LiYMo_3O_8$.[149] The Chevrel phases $M^{II}Mo_6S_8$,[150] have in contrast, been extensively studied for $Mg^2+$,[151] $Na^+$,[152] and $Li^+$batteries.[153] Recent work on $NaMoO_2$ showed reversible Na intercalation.[154]

$LiScMo_3O_8$ serves as an effective model system for understanding and probing the

effects of delocalized redox in Mo cluster compounds. Redox reactions are conventionally believed to proceed on individual atoms and ions, with some impact from the surrounding environment.[20] In contrast, the redox presented here occurs here on a cluster of atoms, that collectively create the molecular orbital states that are implicated. This has a number of important structural and electronic implications, with the $MoO_3$ clusters potentially serving as an electron reservoir. One of the many consequences is that the voltage range found for $Li^+$ insertion and de-insertion is more in line with a working voltage more appropriate for an anode than the higher voltages more typically associated with the $Mo^{4+}/Mo^{6+}$ redox couple.[155]

The combination of experimental investigations and density functional theory (DFT) based calculations reveal the importance of $Li^+$ ordering in this system and its effect on the electrochemical properties. Stable and reversible cycling is demonstrated at rates up to 10 C. Minimal structural changes are observed in *operando* X-ray diffraction across the lithiation range employed. Evidence for phase coexistence regions are attributed to $Li^+$ ordering using potentiometric entropy measurements, as is also supported through extensive computational modeling including the enumeration of structural energetics with varying $Li^+$ content. Studies of battery materials in recent years has pointed to the need for better insights into the nature of bonding and the concept of oxidation state in battery materials.[156–159] Here we show that a deeper understanding of metal-metal bonding as an electronic and crystallographic motif could lead to materials with stable $Li^+$ cycling and minimal structural changes.

## 4.3 Experimental Methods

**Preparation of $LiScMo_3O_8$** $LiScMo_3O_8$ was prepared through a two-step synthesis process first involving conventional solid state calcination, followed by purification using a dilute acid wash. The starting materials were $Sc_2O_3$(Sigma Aldrich, 99.995%), $Li_2MoO_4$(Sigma Aldrich, 99.9%), Mo (Sigma Aldrich, 100 mesh, 99.9%), and $MoO_2$ (Sigma Aldrich, 99%). $Li_2MoO_4$ was dried overnight at 120 °C, Mo was heated overnight at 900 °C in 5% $H_5$/Ar, and $MoO_2$ was heated overnight at 400 °C in 5% $H_5$/Ar. The preparation steps for the precursor powders are key to ensuring purity by removal of water in the case of the salt $Li_2MoO_4$, and correct oxidation states in the case of the Mo and $MoO_2$. The cleaned starting materials were ground together in the exact molar ratio in an agate mortar for 20 minutes. The mixed powder was pressed into a 600 mg pellet, placed into an alumina crucible, and sealed in a silica tube that was back-filled with a partial pressure of Ar. The tube was heated at 790 °C for 24 hours, and water-quenched to room temperature. The reacted pellet was ground to a fine powder and washed in a 2 M $HNO_3$ solution with a 2 hour soak time. The acid wash was necessary to remove trace amounts of residual $MoO_2$. The powder was then washed three times with deionized water to remove any remaining acid traces. The washed powder was then heated gently in a vacuum oven to evaporate residual water. The purified material was stored under inert atmosphere. To confirm sample purity, powder diffraction data were collected at the high-resolution beamline 11-BM at the Advanced Photon Source at Argonne National Laboratory ($\lambda$ = 0.458118 Å). Rietveld refinements to the previously published structure[146] were performed using TOPAS Academic v.6.[50] All visualization involving crystal structures was carried out using VESTA.[51]

**Microscopy** A powder sample of $LiScMo_3O_8$ was dispersed in ultrapure water and subjected to an ultrasonic bath for 5 min to separate the particles. The suspension was then either drop-cast on a Si wafer for SEM investigation or nebulized by an ultrasonic evaporator onto a TEM grid with an ultrathin carbon support film. SEM investigation was carried out using a FEI Quanta SEM, operated at 20 kV. TEM data was acquired with an image-side aberration corrected FEI Titan with CEOS corrector, operated at a primary energy of 300 keV. The spherical aberration was tuned to be 2 $\mu$m and images were acquired using a 4k CMOS camera (TVIPS XF416) in suitable zone axes. Data were analyzed with GMS 3 and imageJ.

**Electrochemistry** Electrochemial studies were performed on composite films cast on copper foil in an 80:10:10 (wt-%) ratio of active material:conductive carbon(TIMCAL Super P): polyvinylidene fluoride (PVDF). The active material and carbon were ball milled together in a small canister for 30 minutes, and then combined with PVDF dissolved in NMP to form a slurry. The mixture was mixed in a FlackTek speed mixer at 2000 rpm for 30 minutes. The slurry was cast using a 120 $\mu$ doctor blade and dried in a vacuum oven at 100 °C. The electrodes were punched into 10 mm diameter disks with a loading between 1 mg cm$^{-2}$ to 2 mg cm$^{-2}$. Swagelok cells were used for electrochemical testing and were fabricated in an Ar-filled glovebox with 1 M $LiPF_6$ in EC/DMC 50/50 v/v (Sigma Aldrich) with a polished Li foil counter electrode and glass fiber separator (Whatman GF/D). Cells were discharged to 1.2 V and charged to 3.0 V using BioLogic potentiostats VMP1 and VMP3. One additional $Li^+$ per formula unit was assumed to insert into the crystal structure for calculating C rates.

***Operando* X-ray diffraction** *Operando* X-ray diffraction was collected using a custom Swagelok-type cell with a Be window approximately 120 $\mu$m thick, allowing X-ray

penetration into the cell while cycling. X-ray diffraction data were collected using a laboratory-source Panalytical Empyrean diffractometer with Cu-K$\alpha$ radiation in Bragg-Brentano geometry. The same Li foil counter electrode, electrolyte, and composite ratio [80:10:10 (wt-%) active:SuperP:PVDF] were used as previously described. The only exception was that the slurry was cast to a slightly thicker 150 $\mu$m layer, directly onto Celgard separator, to improve diffraction counts. The cast electrode was placed face down onto the Be window, and a Whatman glass fiber separator was placed on top to keep the electrode and Celgard from curling or folding before the cell assembly was finished. The cell was flooded with 1M $LiPF_6$ in 50/50 EC/DMC (Sigma Aldrich). $LiScMo_3O_8$ was cycled versus $Li^+$ using a BioLogic SP-200 potentiostat at a C/15 rate. A pattern was collected every 20 minutes during the discharge.

**Electrochemical impedance spectroscopy** Electrochemical impedance spectroscopy was performed on a BioLogic VSP potentiostat/galvanostat. Measurements were made on two-electrode coin cells between 1 MHz and 100 mHz using a 15 mV input. The cells were cycled at a C/20 rate, stopped at various amounts of $Li^+$ insertion, followed by collection of the impedance spectra.

**X-ray photoelectron spectroscopy** X-ray photoelectron spectroscopy samples were prepared by discharging/charging the cast electrodes outlined earlier to the desired voltages. The sample preparation methodology is described elsewhere.[117] All samples were measured using a Thermo Fisher Escalab Xi+ XPS equipped with a monochromatic Al anode (E=1486.7 eV). A cluster gun was used for 40 s to clean the surface and improve count intensity for all samples. Survey scans were measured at 100 eV pass energy, and high-resolution scans were measured in the Sc and Mo regions at 20 eV pass energy. *Ex situ* spectra were referenced to adventious carbon at 284.8 eV.

CasaXPS was used to fit the data using Shirley backgrounds and GL(30) peak shapes. High resolution scans of Sc and Mo were fit using appropriate spin-orbit splitting and peak area ratios.

**Raman spectroscopy** Raman spectra were collected on a Horiba XploRA One confocal Raman microscope. All spectra were collected with a 638 nm diode laser, a diffraction grating with groove density 1200 gr $mm^{-1}$, and 1% laser power ($\approx$0.29 mW) to minimize laser damage to the electrode surface. The hole and slit were fixed at 500 and 50 $\mu$m, respectively. The laser was focused using a 50$\times$ (numerical aperture 0.50) objective, which yielded a nominal spatial resolution of approximately 780 nm. *Operando* measurements were performed by focusing the laser on the front-side of the cathode in a custom spectroelectrochemical cell with a nylon body, stainless steel current collectors, and a borosilicate glass cover slip window (0.17 mm - 0.25 mm thickness). The cell stack was assembled with a slurry-cast electrode prepared as described previously, a Celgard 2400 separator with a 3/32" hole punched out, a polished Li foil anode with a 5/32" hole punched out, and 4 drops (65.8 $\pm$ 0.78 mg) of electrolyte. The electrolyte was the same composition as that used for the cycling experiments diluted by a factor of 10 to yield 0.1 M $LiPF_6$ to limit interference from fluorescence. Spectra were collected with a 3 s acquisition time and 200 accumulations continuously while the cell was cycled galvanostatically at $C/10$ based on 1 $e^-$ between 1.2 V and 3 V. The microscope was refocused once during the experiment towards the end of the first charge cycle (i.e. after approximately 27 h).

**Potentiometric entropy measurements** The open circuit voltage $U_{ocv}(x,T)$ and the entropic potential $\partial U_{ocv}(x,T)/\partial T$ of the coin cells with the $LiScMo_3O_8$ anode and lithium metal counter electrode were measured as functions of $Li^+$ composition $x$

with a potentiometric entropy measurement technique using the apparatus described previously.[160] The potentiometric entropy measurements consisted of imposing a series of constant current pulses at a rate of C/10 for 30 minutes at 20 °C each followed by a relaxation period of 4.5 hours, ensuring that equilibrium had been reached and that $\partial U_{ocv}(x,T)/\partial T$ was less than 1 mV/h. During the relaxation period, a step-like temperature profile was applied to the coin cell from 15 °C to 25 °C in 5 °C increments with a thermoelectric cold plate (TE technology, CP-121). The temporal evaluation of the cell voltage was recorded with a potentiostat (Biologic, VSP-300). Before recording the open circuit voltage $U_{ocv}(x,T)$ and imposing the next temperature step, we verified that the cell had reached thermodynamic equilibrium by making sure that the temperature difference between the cold plate and the top of the coin cell was less than 0.1 °C and that the time rate of change of the open circuit voltage $\partial U_{ocv}(x,T)/\partial T$ was less than 1 mV/h.

From the Nernst equation, the open circuit voltage $U_{ocv}(x,T)$ of the battery system is defined as[161]

$$U_{ocv}(x,T) = -\frac{\mu^{+}_{\mathrm{Li}}(x,T) - \mu^{-}_{\mathrm{Li}}(x,T)}{e} \tag{4.1}$$

Here, $e$ is the unit charge and $\mu^{+/-}_{\mathrm{Li}}(x,T)$ is the $Li^+$ chemical potential of the cathode (superscript "+") and anode (superscript "−"). By definition, $\mu^{+/-}_{\mathrm{Li}}(x,T)$ can be expressed as the partial molar Gibbs free energy, i.e.,[161]

$$\mu^{+/-}_{\mathrm{Li}}(x,T) = \frac{\partial g^{+/-}(x,T)}{\partial x} \tag{4.2}$$

where $x$ is $Li^+$ composition in the electrode and is defined as the fraction of the number of moles of $Li^+$ $N_{\mathrm{Li}}$ intercalated per number of moles of molecular units of active material $N_{+/-}$ in the electrode such that $x = N_{\mathrm{Li}}/N_{+/-}$. Furthermore, under isobaric

conditions, based on Maxwell's relations, the molar entropy of each electrode $s^{+/-}(T)$ can be expressed as[162]

$$s_{+/-}(x,T) = -\frac{\partial g_{+/-}(x,T)}{\partial T} \tag{4.3}$$

Thus, Based on the Clairaut's theorem, taking the derivative of Eq.(4.1) with respect to temperature $T$, the equation can be written in terms of the molar entropy $s^{+/-}(x,T)$, i.e.,

$$\frac{\partial U_{ocv}(x,T)}{\partial T} = \frac{1}{e}\left[\frac{\partial s_{+}(x,T)}{\partial x} - \frac{\partial s_{-}(x,T)}{\partial x}\right] \tag{4.4}$$

For the coin cells investigated in this study, the Li metal counter electrode was considered to be an infinite $Li^+$ reservoir with no lattice rearrangement upon lithiation/-delithiation[163]. Therefore, the partial molar entropy of $Li^+$ metal electrode $\partial s^{\mathrm{Li}}(x,T)/\partial x$ can be assumed to be independent of $x$ and constant when holding the temperature and pressure constant, i.e., $\partial s^{\mathrm{Li}}(x,T)/\partial x = s_o^{\mathrm{Li}}(T)$[164, 165]. Therefore, the entropic potential of the coin cell can be written as

$$\frac{\partial U_{ocv}(x,T)}{\partial T} = \frac{1}{e}\left[\frac{\partial s_{\mathrm{LSMO}}(x,T)}{\partial x} - s^{\mathrm{o}}_{\mathrm{Li}}(T)\right]. \tag{4.5}$$

where superscripts "Li" and "LSMO" refer to the $Li^+$ metal counter electrode and $LiScMo_3O_8$ working electrode respectively. Thus, the the measured $\partial U_{ocv}(x,T)/\partial T$ depends on the partial molar entropy of $LiScMo_3O_8$ since $s_o^{\mathrm{Li}}(T)$ is independent of $x$. In other words, analyzing $\partial U_{ocv}(x,T)/\partial T$ measurements provides insights in the physicochemical phenomena occurring in the $LiScMo_3O_8$ electrode.

**Computational Methodology** Mapping of the bond valence in the space of the crystal structure was carried out using the script PyAbstantia.[69]

Electronic structure calculations using density functional theory (DFT) were performed with the Vienna *ab initio* Simulation Package (VASP).[166–169] All calculations used projector augmented wave (PAW) pseudopotentials (Li sv, Sc sv, Mo sv, and O),[170, 171] a plane-wave energy cutoff of 650 eV, and the SCAN meta-GGA exchange-correlation functional.[172, 173] The Brillouin zone was sampled with Γ-centered Monkhorst-Pack meshes[174] of densities along each reciprocal lattice vector of 30 Å and 40 Å for total energy and density of states calculations, respectively. For total energy calculations, structures were relaxed using a force convergence criterion of 0.02 eV/Å and final static calculations were run using the linear tetrahedron method.[175] All calculations were spin-polarized, with ferromagnetic initialization of moments unless otherwise stated.

Symmetrically distinct $Li^+$-vacancy orderings in $Li_xScMo_3O_8$ were enumerated using the Clusters Approach to Statistical Mechanics (CASM) software package.[176–179] All available tetrahedral and octahedral sites in the $Li^+$/Sc layer were considered for $Li^+$ occupation, except those sharing faces with the Sc sites, yielding two distinct tetrahedral sites and three equivalent octahedral sites per primitive cell. Additionally, we did not consider configurations with face-sharing between $Li^+$ sites. Energies were calculated for 295 configurations.

Voltage was calculated via the Nernst equation (Eq. 4.1), with the chemical potential of $Li^+$ metal in the body-centered cubic structure used as the reference anode chemical potential.

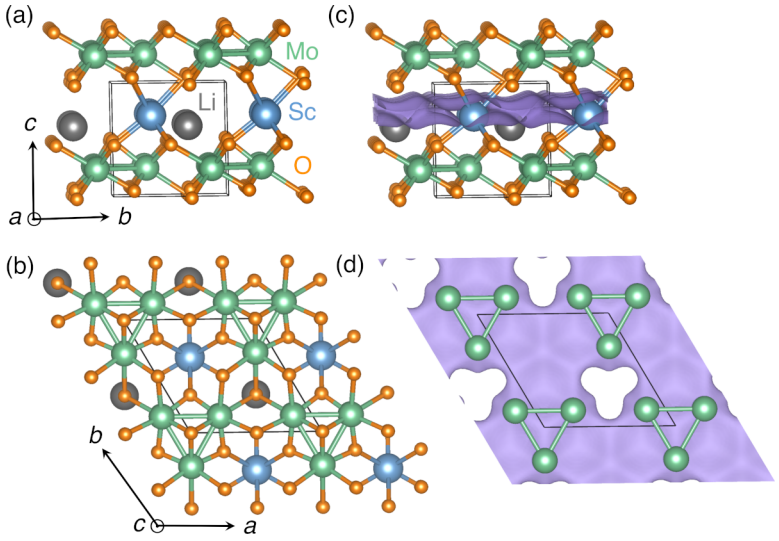


Figure 4.1: Crystal structure of $LiScMo_3O_8$ (space group is $P3m1$, No. 156) contains alternating layers of triangular clusters of metal-metal bonded Mo atoms and $Li^+$/Sc. $Li^+$ is tetrahedrally coordinated. (a) Side view and (b) top view of structure. (c, d) Side view and top view of the structure, respectively, with the bond valence difference map (purple isosurface) for $Li^+$ in the space of the structure displayed for an isosurface value $\Delta v = 0.2$ valence units.

## 4.4 Results and Discussion

### 4.4.1 Crystal and Electronic Structure

Careful examination of the crystal structure of $LiScMo_3O_8$ is critical for understanding its electrochemical, structural, and electronic properties. The Mo cluster compounds get their namesake from a distinct structural motif, namely a kagomé lattice built of triangular clusters of metal-metal bonded Mo atoms. Figure 5.1(a) shows how this distinct motif is separated by an alternating layer of $Li^+$/Sc. In the Mo layer, $MoO_6$ octahedra form $Mo_3O_{13}$ clusters that share some O between clusters. Although formally $Mo^{4+}$, Mo-Mo bonding accounts for the 6 d electrons in this electron precise structure. Traditional redox chemistry is typically considered on an individual atom. In this case, the metal-metal bonded Mo atoms provide a center for delocalized redox

within the cluster, which is a much more unconventional mechanism. We surmise that these clusters have a profound impact on the structural stability of the material with $Li^+$ insertion, and the overlapping d orbitals may have the potential to dampen volume expansion due to the delocalized nature of their electrons. Figure 5.1(b) gives the top down perspective along the $c$ axis, illustrating how the Mo clusters are offset from the scandium atoms in the following layer. Each Mo is in a +4 oxidation state, sharing one electron with each neighboring Mo atom. Because of the lower starting oxidation state of Mo, we will not be able to access multielectron redox. This instead will provide a platform for a good anode potential using the $Mo^{4+}$ to $Mo^{3+}$ redox couple, in sharp contrast to other Mo-based oxides such as $MoO_3$ that fall in between conventional anode and cathode voltages.[180]

Bond-valence sum mapping is a useful tool to approximate ion transport pathways within a 3D crystal structure. The valence difference ($\Delta v$) between the probe ion, in this case $Li^+$, and the actual electrostatic valence, can be roughly related to the activation energy required for ion transport. Therefore, mapping the valence difference provides a means of visualizing possible $Li^+$ migration paths.[76] The isosurface for a $\Delta v = 0.2$ in valence units for $LiScMo_3O_8$ is shown in panel (c) and (d) of Figure 5.1. This isosurface illustrates a probable ion conduction region within the $Li^+$/Sc layer, suggesting low energy 2D diffusion. Unsurprisingly, the isosurface also indicates that there is no expected ion conduction through the metal-metal bonded Mo layers.

To understand the electronic structure of $LiScMo_3O_8$, density-functional theory-based structure calculations are utilized to provide qualitative insight about this material as a $Li^+$ host. The density of states, displayed in Figure 4.2, shows filled Mo d-states just below the Fermi level and a large band gap, indicating the starting material is an insulator. Any additional electrons would begin to fill the Mo d-states around 2 eV.

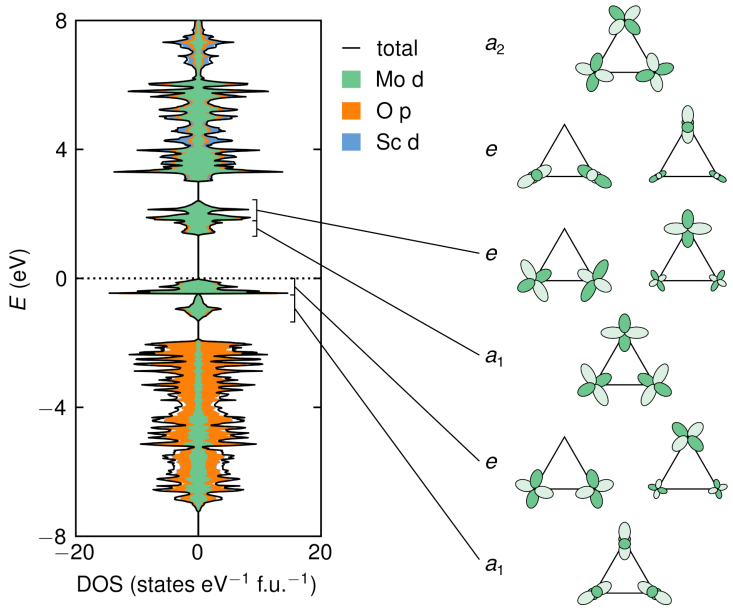


Figure 4.2: Spin-polarized density of states of $LiScMo_3O_8$ alongside the molecular orbitals formed by the Mo $t_{2g}$ orbitals. Molecular orbitals are ranked by energy in the order determined by Tsuge *et al.*[181] The DOS was calculated by Jonas L. Kaufman.

However, these states are very localized and the small dispersion indicates that even with $Li^+$ insertion, this material would not become a good conductor. Additionally, the large gap in the DOS between filled and unfilled states foreshadows a potential two-phase reaction. The higher energy states will not be able to continuously fill and therefore inserting $Li^+$ could thermodynamically favor a lower energy phase. The majority of states near the Fermi level comprise of Mo d-states.

A molecular orbital (MO) diagram can help to understand the nature of the Mo bonding in the context of the electronic structure more specifically. A qualitative MO diagram was worked out for equilateral $Mo_3$ triangles by Tsuge *et al.*[181] Figure 4.2 shows an adapted version of their proposed MO diagram, and how each specific energy level corresponds to the DOS. The six electrons for each cluster occupy the three bonding MOs. If there are more electrons, these occupy the upper $a_1$ or $e$ MOs that arise from more weakly interacting AOs. The metal d-orbitals of the clusters play an

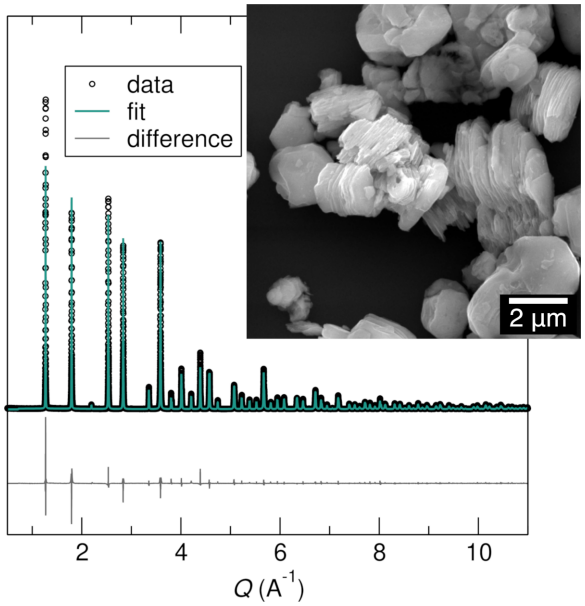


Figure 4.3: 11-BM synchrotron powder X-ray diffraction data for $LiScMo_3O_8$ shows a single phase of the target layered structure. Refinement statistics can be found in Table S1 in the Supporting Information. The inset displays a scanning electron micrograph of $LiScMo_3O_8$ crystallites with plate-like structure. The micrograph was taken by Christian Dolle.

important role with $Li^+$ insertion. As more electrons are inserted, they will occupy higher energy MOs.

Prior studies indicated some difficulty in obtaining a phase pure material.[146] Optimization of precursor powders, in conjunction with a purification step, allowed us to realize a phase-pure sample as a black powder. This structure was characterized with powder synchrotron X-ray diffraction, as shown in Figure 4.3. Refinement statistics are shown in Table S1 in the Supporting Information. Future work will use neutron diffraction to develop a more complete picture of the structure. Characterization of this material using electron microscopy reveals important insights at multiple length scales. SEM on the bulk powder particles shows micron-sized particles that are comprised of highly crystalline sheets stacked on top of each other. The anisotropic morphology of these particles allows for access to $Li^+$ along the edges of the sheets, but not through

the faces.

Looking more closely at the crystalline sheets in Figure 4.4(a), using aberration-corrected high resolution transmission electron microscopy, we see how these thin sheets layer along the edge of a particle. We additionally use this technique to directly observe the atomic lattice along the [001] plane.[Figure 4.4(b)] The resulting image resolves the expected hexagonal tiling characteristic of the kagomé-structured Mo sheets. The inset simulation using our model structure blends seamlessly with experiment.

### 4.4.2 Electrochemistry

We first aim to understand the charge storage properties of this material through a variety of electrochemical cycling experiments displayed in Figure 7.19. Figure 7.19(a) shows variable rate galvanostatic cycling. At the slowest rate, as $Li^+$ intercalates into $LiScMo_3O_8$, a large, flat plateau occurs at 1.5 V. This plateau region extends as nearly an additional 1.25 $Li^+$ are inserted and the stoichiometry is $Li_{2.25}ScMo_3O_8$. A more subtle plateau occurs immediately after, followed by a relatively smooth sloping regime until maximum lithiation. This material is capable of storing an additional 2 $Li^+$ at slow rates, for a capacity close to 120 mAh $g^{-1}$. Upon charging, the material displays no polarization for the matching short and long plateau at 1.5 V, but notably contains an additional unsymmetrical plateau slightly above 2 V. As the cycling rate is increased, the length of the plateau gradually diminishes up to a 10C rate. Although $LiScMo_3O_8$ does not store a significant amount of charge at fast rates, we show as a proof of concept that it is capable of cycling quickly and that the material is able to recover again at slow rates. Because $Li^+$ can only diffuse through the edges of these micron-sized sheets, it is possible that the particle morphology is limiting the capacity retention at fast rates.

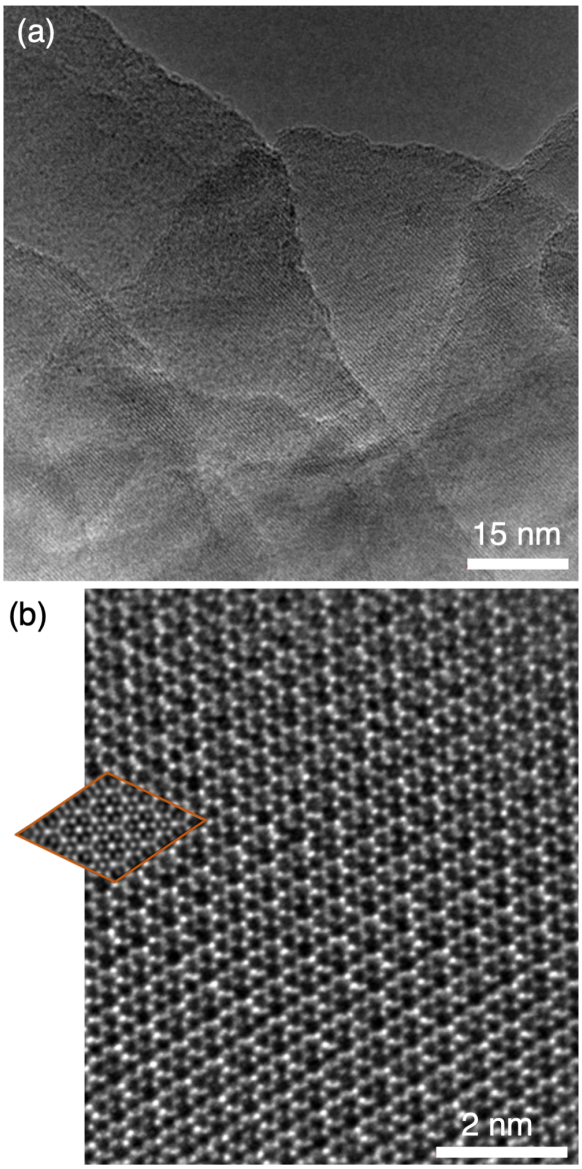


Figure 4.4: (a) Aberration-corrected high resolution transmission electron microscopy (HRTEM) shows how the thin, crystalline sheets overlap along the edge of a powder particle. (b) HRTEM also shows highly ordered hexagonal tiling characteristic of a kagomé-type network. The orange inset contains a HRTEM simulation of three stacked unit cells of $LiScMo_3O_8$ along the [001] direction. The simulation parameters include an energy of 300 keV, a defocus spread of 3 nm, a $C_s$ of $+2\,\mu$m, and a slice thickness of 0.1 nm. The TEM was collected by Christian Dolle.

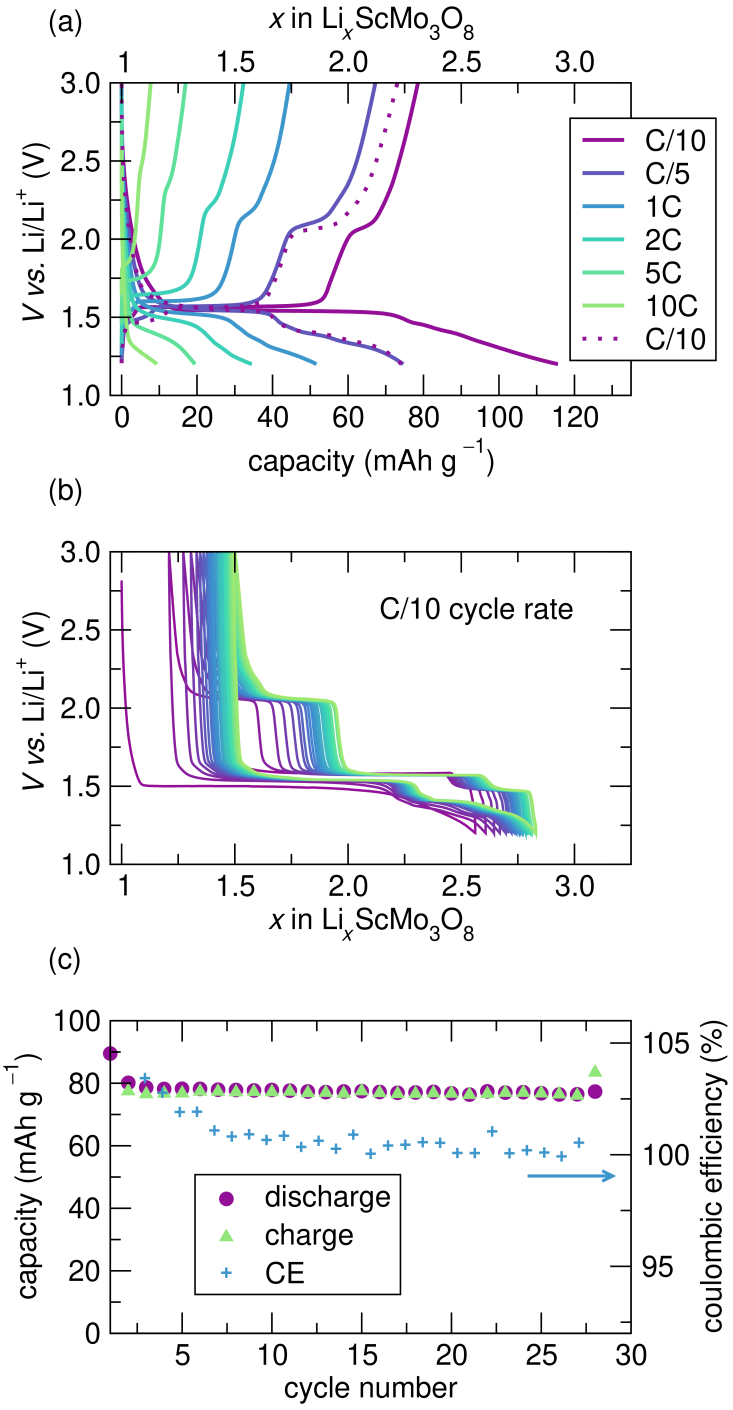


Figure 4.5: Electrochemistry of $LiScMo_3O_8$. (a) Galvanostatic cycling at rates from C/10 to 10C and its recovery. (b) Galvanostatic cycling at a C/10 rate shows slight irreversible capacity loss after the first cycle but highly reversible features. (c) summarizes the rate retention capability of $LiScMo_3O_8$ from the galvanostatic cycling in figure(b).

While outside of the scope of this fundamental study, it is proposed here that the rate capability could be greatly increased with morphology optimization.

Extended cycling of $LiScMo_3O_8$ shows highly repeatable and reversible features in the voltage curve. Figure 7.19(b) overlays the discharge curves at a C/10 rate over 30 consecutive cycles. After the first cycle, there is clearly some initial capacity loss, but the major features, notably the plateaus, remain highly reproducible with no changes to the voltage. Figure 7.19(c) summarizes the extended cycling, highlighting its stable capacity retention. The coulombic efficiency hovers around 100%. The initial points over that threshold are possibly due to some small side reaction, but this does not significantly affect the reversibility or capacity. Electrochemical impedance spectra of slurry electrodes as a function of $Li^+$ content indicate that the charge transfer resistance remains constant over the lithiation range investigated, consistent with the calculated electronic structure of the starting material. (Figure S1 in the Supporting Information)

As $Li^+$ inserts into the structure, delocalized redox on the Mo clusters should result in a reduction of the Mo oxidation state. Following the equation $LiScMo_3O_8 + x\,Li^+ + x\,e^{-1} \rightarrow Li_{1+x}ScMo_3O_8$ the theoretical capacity would be 172 mAh $g^{-1}$ if 3 $e^-$ per formula unit are inserted ($x = 3$), where we assume each $Mo^{4+}$ reduces to $Mo^{3+}$. We probe this expected change in chemical bonding through *ex situ* X-ray photoelectron spectroscopy (XPS). Although experimentally only 2 $e^-$ per formula unit are inserted, we are able to both qualitatively and quantitatively observe a marked evolution of the Mo chemical bonding environment. Figure 4.6 (a) shows the spectrum of the pristine material, where all Mo atoms are in the expected +4 oxidation state, showcasing the characteristic doublet of the d orbital. After insertion of 1.84 $Li^+$, Figure 4.6 (b) displays the drastic change in spectrum with the emergence of an additional doublet at lower binding energy, signifying coexistence of both $Mo^{4+}$ and $Mo^{3+}$ states. This sample was

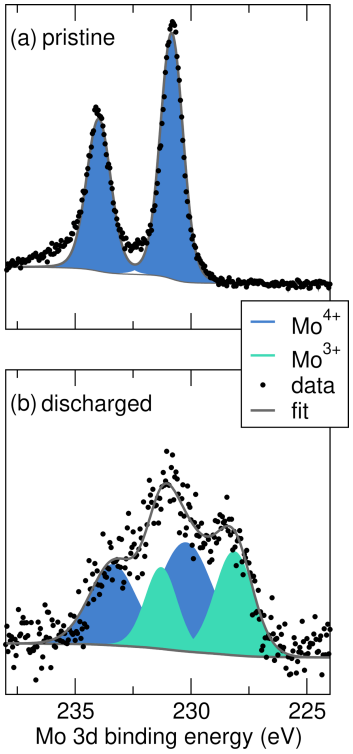


Figure 4.6: X-ray photoelectron spectra displaying the Mo 3d binding energy region for (a) pristine $LiScMo_3O_8$ and (b) discharged material ($Li_{2.84}ScMo_3O_8$). The pristine material contains only $Mo^{4+}$ while the discharged material contains both $Mo^{3+}$ and $Mo^{4+}$. The binding energy of the $Mo^{4+}$ peaks do not match precisely, due to the unusual metal-metal bonding feature in the structure.

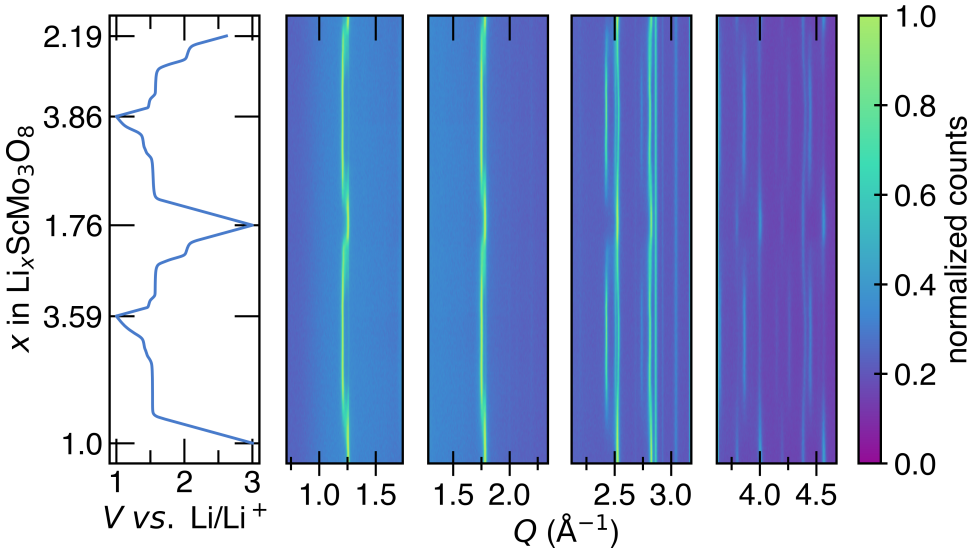


Figure 4.7: *Operando* X-ray diffraction of $LiScMo_3O_8$ during the first two galvanostatic discharge/charge cycles at a C/15 cycling rate. The electrochemistry is shown in the left-most panel, inserting over two additional $Li^+$ to $Li_{3.59}ScMo_3O_8$ on the first discharge. Select regions of the diffraction patterns are shown as a heat map to better visualize the evolution of the diffraction peaks.

discharged to $Li_{2.84}ScMo_3O_8$, therefore we would expect 62% of the Mo atoms to be $Mo^{3+}$ by balancing the oxidation states. Experimentally we measure this value to be 41% through quantification in CasaXPS software. These values could deviate due to a combination of surface sensitivity to oxidation and more importantly, complexity arising due to the presence of metallic states. It is notable that the clusters allow reduction to the $Mo^{3+}$ oxidation state, resulting in a lower working voltage than the $Mo^{6+}/Mo^{4+}$ couple.

The structure of a voltage curve gives direct insight into chemical changes of a system. There is a relation between the Gibbs free energy and voltage curve, so phase transformations will have clear signatures in the profile, manifesting as a plateau.[182] Because the electrochemistry of this system shows such clear plateaus, we expect there to be phase transitions. *Operando* X-ray diffraction is used to understand the evolution of the structure with lithiation. Figure 4.7 shows a heat map of select panels highlight-

ing the major diffraction peaks as over 2 additional $Li^+$ are slowly inserted. We observe subtle changes and shifts to these peaks, consistent with a two-phase reaction. The full data range can be found in Figure S2 and Figure S3 in the Supporting Information. Most layered electrode materials exhibit greater signs of expansion, but the *operando* diffraction data show only slight strain in the structure.

A series of X-ray diffraction spectra were extracted from the *operando* data set to allow for comparison between the experimental and simulated diffraction patterns. Figure 4.8 shows select panels comparing the experimental and simulated diffraction patterns as function of lithiation. We see slight shifts and the emergence of new peaks, consistent with a two-phase reaction. There is good agreement between experiment and simulation, and the emergence of new peaks is captured well by the calculations. The full simulated $Q$ range can be found in Figure S6 in the Supporting Information. Figure 4.8(e) compares experimentally observed unit cell volumes to calculated volumes of predicted ground state structures from DFT. These extensive calculations are discussed in detail in the following section. Going from $LiScMo_3O_8$ to $Li_3ScMo_3O_8$, calculations predict a small volume expansion of 2%, which is comparable to the typical prediction error for bulk solids of the DFT functional used (SCAN).[183, 184] The *operando* and experiments shows 3% change in volume with lithiation, in line with calculations predicting minimal perturbation to the structure.

From a structural standpoint, X-ray diffraction does not show any major changes with $Li^+$ insertion, but XPS concludes that Mo is being reduced on the clusters. Raman spectroscopy allows us to probe the vibrational modes in crystal structures associated with bonding. We use *operando* Raman spectroscopy to better understand what changes are happening to the crystal structure of $LiScMo_3O_8$, since the changes are subtle and dominated by bonding of the Mo clusters. Figure 4.9 shows Raman spectra

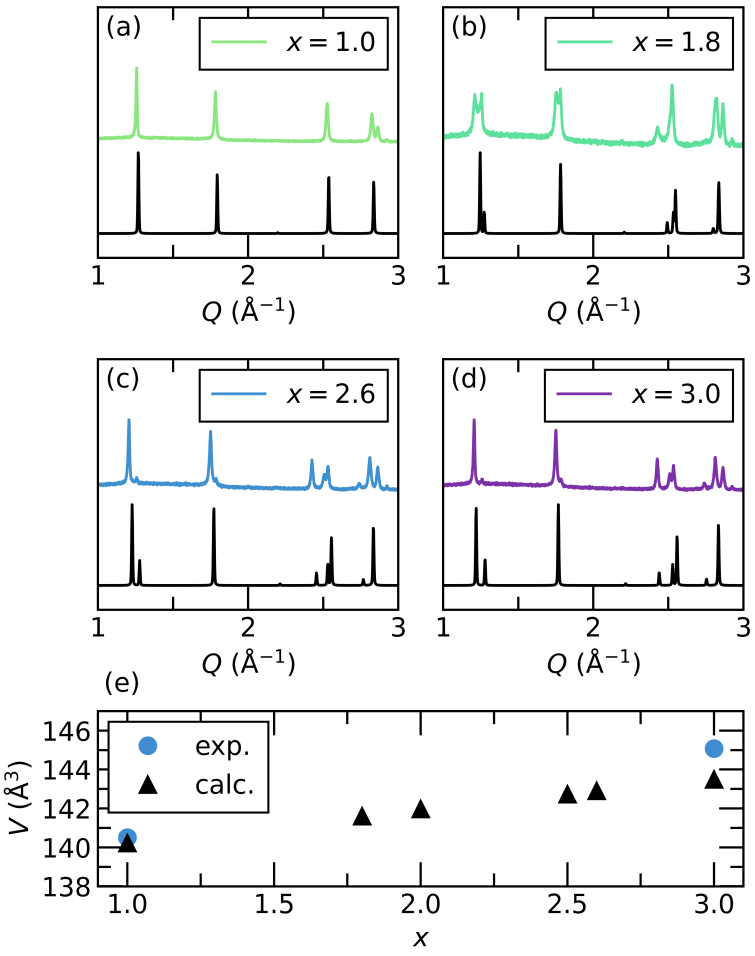


Figure 4.8: Select panels comparing the extracted X-ray diffraction pattern for $Li_xScMo_3O_8$ from the *operando* experiment and the DFT simulated diffraction pattern below for corresponding lithiation values (a) $x = 1.0$ (b) $x = 1.8$ (c) $x = 2.6$ and (d) $x = 3.0$. There is relatively good agreement between the experimental and simulated diffraction. (e) Comparison of the calculated volumes of lowest energy structures determined from DFT, and experimentally measured unit cell volumes from *operando* lab diffraction. DFT predicts low volume expansion, which is confirmed with the data set showing a volume expansion of 3%.

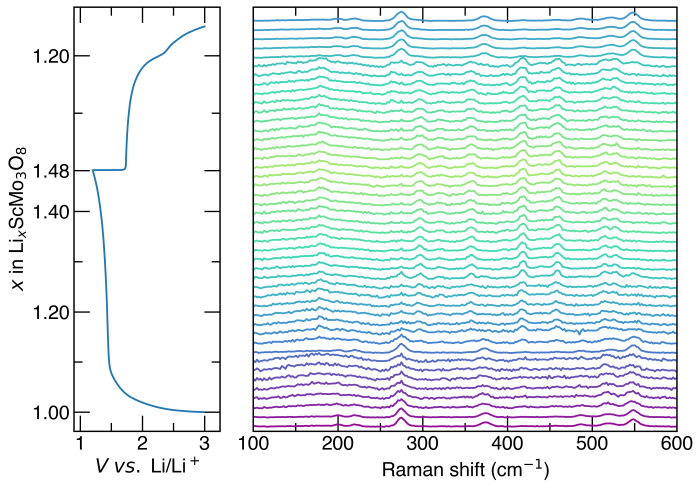


Figure 4.9: *Operando* Raman spectroscopy of $LiScMo_3O_8$ during the first galvanostatic cycle at a C/20 cycle rate. The corresponding electrochemistry is shown in the left panel, where 0.48 $Li^+$are inserted to form $Li_{1.48}ScMo_3O_8$.

as a function of $Li^+$ content during discharge and charge. A smaller amount of $Li^+$ was inserted than desired due to non-optimized electrochemistry in the custom *operando* cell. (Figure S5 in the Supporting Information) Despite this, we are still able to gain important insight about the changes to the Mo bonding with lithiation.

The initial spectrum measured in *operando* matches well with the *ex situ* spectrum measured *ex situ* (Figure S6 in the Supporting Information), which confirms that the modes are related to the active material. Although it is difficult to accurately assign Raman modes, we use literature on similar systems containing Mo clusters to interpret the data. Literature indicates that the 370 $cm^{-1}$ mode corresponds to a Mo cluster breathing mode.[149, 185–187] After 0.1 $Li^+$ inserts, this peak shifts to lower wavenumbers. In the context of the MO diagram (Figure 4.2), as $Li^+$ inserts, electrons begin to fill a higher energy antibonding orbital of the Mo cluster. This would weaken the Mo-Mo bonds and result in a softer stretch, which is observed experimentally. As the cell is charged and $Li^+$ is removed, the same peak abruptly shifts back to the original position.

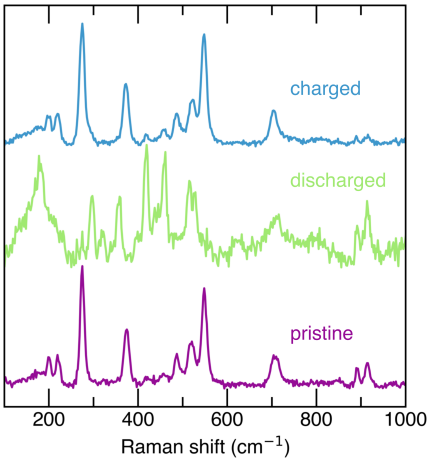


Figure 4.10: Select *operando* Raman spectroscopy spectra from Figure 4.9, displaying the pristine spectrum, the fully discharged spectrum, and the fully charged spectrum. The similarity between the pristine and fully charged spectra indicate the reversibility of the Raman modes.

Adding $Li^+$ changes the local symmetry of the material, resulting in different allowed and forbidden Raman modes. However, we observe similar modes between $LiScMo_3O_8$ and $LiZn_2Mo_3O_8$, allowing the modes associated with the $Mo_3O_{13}$ molecular units to be identified.[185] And although we cannot assign all the new modes, they do revert back to those observed in the pristine spectra. An expanded comparison of the pristine, discharged, and charged spectra in Figure 4.10 underscore the highly reversible nature of the $Mo_3$ breathing mode and experimentally indicate the structural importance of the Mo clusters and their d-orbital overlap for $Li^+$ insertion.

### 4.4.3 Entropic potential measurements and $Li^+$ ordering

This material shows clear plateaus in the electrochemistry, indicating phase coexistence. Diffraction experiments indicate slight evolution of the crystal structure, consistent with two-phase regions. To better understand the nature of the phase coexistence, we combine insights from experimentally obtained entropic potential measure-

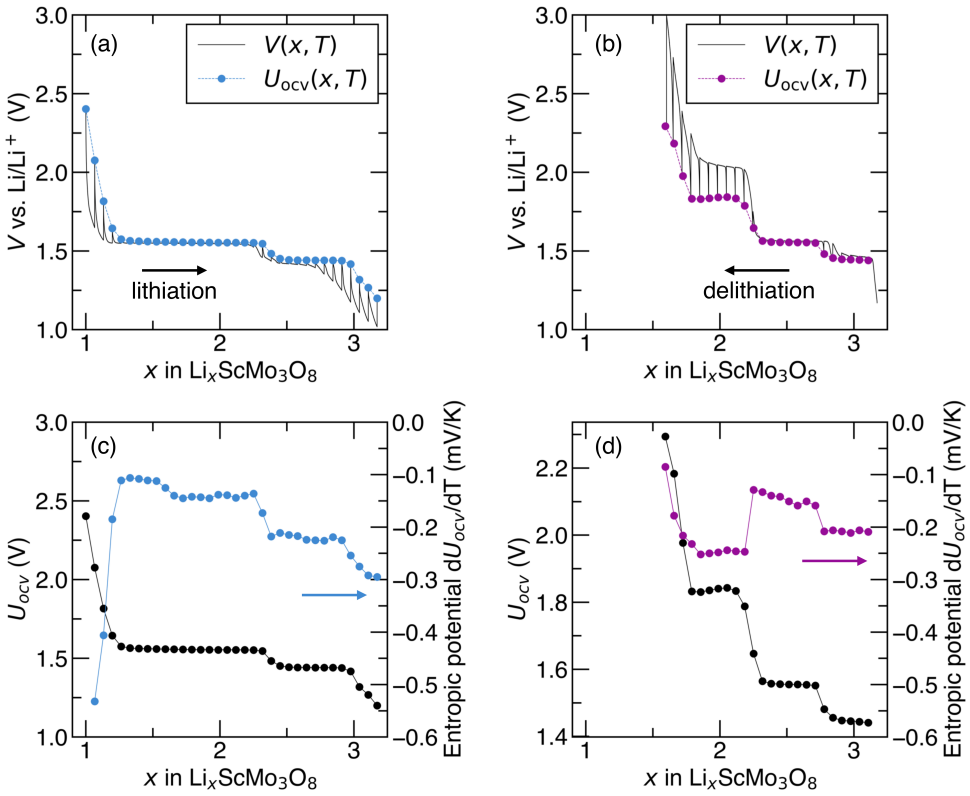


Figure 4.11: Open circuit voltage $U_{ocv}(x,T)$ and operating voltage $V(x,T)$ during (a) lithiation, (b) delithiation, and $U_{ocv}(x,T)$ and entropic potential $\partial U_{ocv}(x,T)/\partial T$ during (c) lithiation, (d) delithiation as functions of $Li^+$ composition $x$ in $Li_xScMo_3O_8$ at a rate of C/10 and at 20 °C. The calorimetry data was collected by Sun Woong Baek.

ments and extensive DFT-based calculations, conclusively determining that $Li^+$ ordering drives these features. Figures 4.11(a) and 4.11(b) plot the open circuit voltage $U_{ocv}(x,T)$ and the operating voltage $V(x,T)$ during lithiation and delithiation, respectively. GITT consists of applying constant current pulses, followed by a relaxation period at 20 °C to allow the system to reach equilibrium, allowing observation of the dynamic behavior of $V(x,T)$ and measurement of thermodynamic properties such as $U_{ocv}(x,T)$. During lithiation, the $U_{ocv}(x,T)$ curve clearly shows two plateaus, corresponding to two separate phase coexistence regions. The overpotential, defined as [$V(x,T)$ - $U_{ocv}(x,T)$], was much smaller in the first voltage plateau at 1.6 V compared to the second voltage plateau at 1.4 V, suggesting relatively fast kinetics of $Li^+$ intercalation in the former[188]. Disparate from lithiation, $U_{ocv}(x,T)$ the delithiation process features three voltage plateaus at 1.8 V, 1.6 V, and 1.4 V [Figure 4.11(a)]. Once again though, the overpotential in the voltage plateau at 1.6 V was much smaller than that in the voltage plateaus at 1.8 V and 1.4 V, again indicating relatively fast kinetics of $Li^+$ deintercalation at that voltage.

Figure 4.11(c) plots the open circuit voltage $U_{ocv}(x,T)$ and the entropic potential $\partial U_{ocv}(x,T)/\partial T$ at 20 °C as functions of $x$ in $Li_xScMo_3O_8$ at a rate of C/10 during lithiation. At the beginning of lithiation, for $x \leq 1.25$, both $U_{ocv}(x,T)$ and $\partial U_{ocv}(x,T)/\partial T$ exhibit smooth sloping curves, indicating $Li^+$ intercalation in a homogeneous solid solution.[189] For $1.25 \leq x \leq 2.25$, $U_{ocv}(x,T)$ was constant at 1.6 V, suggesting two-phase coexistence. However, $\partial U_{ocv}(x,T)/\partial T$ measurements show two distinct plateaus in the same region. Therefore, it is likely that there are two instances of phase coexistence in the regions $1.25 \leq x \leq 1.6$ and $1.6 \leq x \leq 2.25$. $\partial U_{ocv}(x,T)/\partial T$ was slightly larger for for the first region than the second one, suggesting a transition to a more ordered structure. Both $U_{ocv}(x,T)$ and $\partial U_{ocv}(x,T)/\partial T$ for $2.25 \leq x \leq 2$ were constant

and independent of $x$, confirming a single two-phase coexistence region. After $x \geq 3$, both $U_{ocv}(x,T)$ and $\partial U_{ocv}(x,T)/\partial T$ are sloping curves corresponding to lithiation in a homogeneous solid solution.

We similarly analyze $U_{ocv}(x,T)$ and $\partial U_{ocv}(x,T)/\partial T$ during delithiation (Figure 4.11(d)). At the beginning of delithiation, for $3.2 \geq x \geq 2.25$, both $U_{ocv}(x,T)$ and $\partial U_{ocv}(x,T)/\partial T$ feature two plateaus, analogous to those observed during lithiation and identical in magnitude. This is an indicator of structural reversibility. At the end of delithiation ($2.25 \geq x \geq 1.6$), $U_{ocv}(x,T)$ contains another plateau at 1.8 V. Here, the measured $\partial U_{ocv}(x,T)/\partial T$ is smaller than that at 1.6 V during lithiation. The smaller $\partial U_{ocv}(x,T)/\partial T$ indicates a smaller partial molar entropy, suggesting the transition on delithiation is more ordered than that at the same voltage on lithation. Entropic potential measurements enhance our understanding of phase coexistence in this system, while DFT is used to ascertain the more fine mechanistic details.

DFT calculations were performed to explore $Li^+$ ordering preferences with varying composition $x$ in $Li_xScMo_3O_8$. The calculated formation energies of many distinct $Li^+$-ordered configurations and the resulting voltage profile are shown in Figure 4.12, with the relaxed structures of select predicted ground state configurations shown in Figure 4.13. At $x = 1$, the synthesized $LiScMo_3O_8$ structure shown in Figures 5.1 and 4.13(a) is predicted to be stable. In this structure, the $Li^+$ exclusively occupy one of the two tetrahedral sites that do not share faces with Sc sites. The other such tetrahedral site lies directly above/below the centers of the $Mo_3$ clusters, rather than between them, and as a result is much less favorable for $Li^+$ occupation (1.05 eV per formula unit higher in energy at $x = 1$). At $x = 3$, the other composition extreme, all the octahedral $Li^+$ sites are filled, as shown in Figure 4.13(b). For $1 < x < 3$, the low-energy configurations display a mix of tetrahedral and octahedral $Li^+$, as indicated by the col-

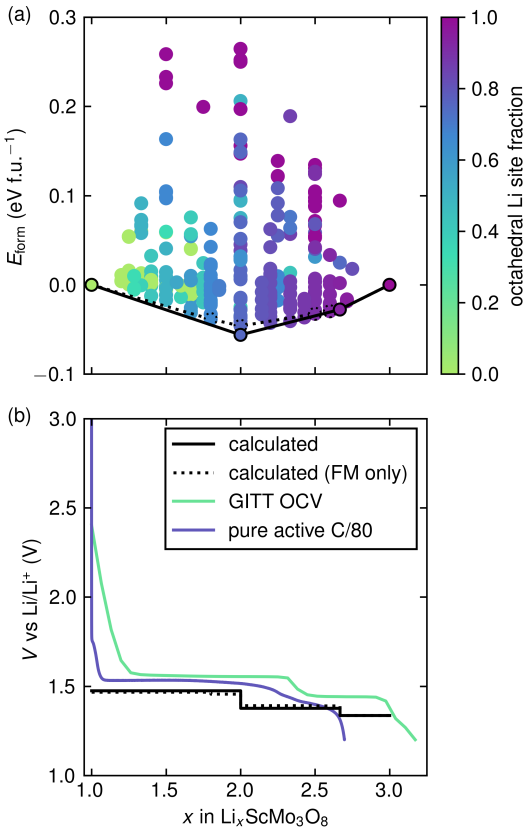


Figure 4.12: (a) Calculated formation energies of distinct $Li^+$-vacancy orderings in $Li_xScMo_3O_8$. Points are colored by the fraction of $Li^+$ in the structure that occupy octahedral sites (as opposed to tetrahedral sites). The solid black line is the convex hull of all calculated configurations, while the dotted black line is the convex hull of only those configurations that retained a ferromagnetic state. (b) Calculated equilibrium voltage profiles for all configurations (solid black line) and ferromagnetic configurations only (dotted black line). Two different experimental voltage profiles from lithiation are also shown. The calculations were performed by Jonas L. Kaufman.

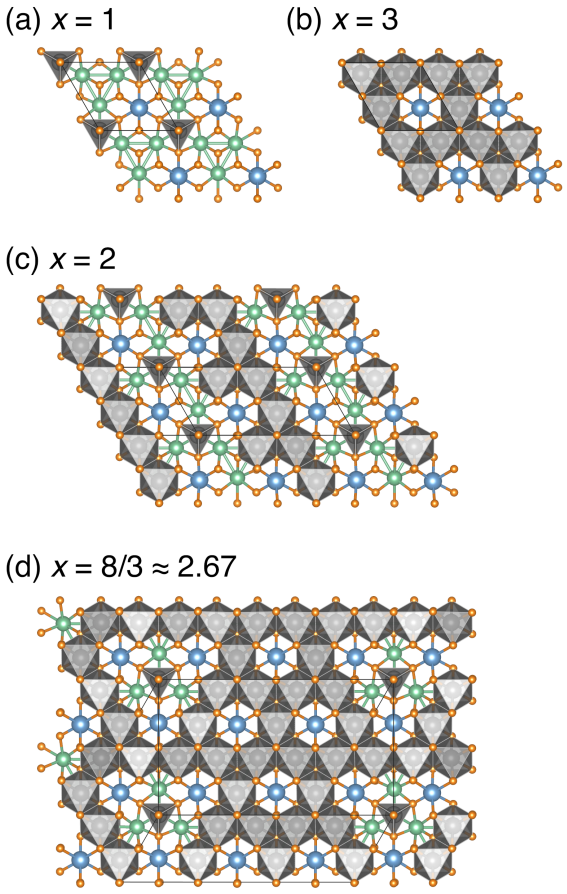


Figure 4.13: Relaxed structures of the calculated $Li^+$-vacancy-ordered ground state configurations in $Li_xScMo_3O_8$ at (a) $x = 1$, (b) $x = 3$, (c) $x = 2$, and (d) $x = 8/3$. Coordination polyhedra are shown for $Li^+$ only. Structures visualized using VESTA.[51] The calculations were performed by Jonas L. Kaufman.

ors in Figure 4.12(a). Simulated X-ray diffraction patterns for selected ground state structures are shown in Figure S6 in the Supporting Information. Small deviations in relative intensity and peak positions between the simulated and experimental diffraction patterns are attributed to the perfect ordering associated with DFT cells that are not representative of the actual experimental system.

Although all calculations were initialized with ferromagnetic (FM) moments, some configurations spontaneously relaxed to non-FM configurations of the $Mo_3$ cluster moments. Additionally, for the predicted FM ground state structure at $x = 2$ (Figure 4.13(c)), we recalculated its energy with an antiferromagnetic (AFM) ordering of the two distinct $Mo_3$ cluster moments, which lowered the energy by 10 meV per formula unit. This preference for AFM ordering is consistent with the reported magnetic behavior of the related material $Li_2ScMo_3O_8$.[190] However, as illustrated in Figure 4.12(b), including the non-FM configurations does not significantly alter the predicted voltage. The predicted voltage is overlaid with two experimental voltage curves, one from GITT (cast electrode) in Figure 4.11(a), and one from a pure active cell discharged very slowly. Both experimental voltages are in extremely good agreement with the calculated voltage. The second plateau of the pure active cell is slightly smoothed out, but the GITT curve captures both distinct plateaus. The apparent deviation in composition between the calculated and GITT voltage curves could indicate a slight overestimate of $x$ in the experiment or the existence of an additional ground state ordering above $x = 2$.

Examining the predicted ground state structures (Figure 4.13) reveals a common $Li^+$ ordering motif among them. Essentially, the low-energy structures between $x = 1$ and $x = 3$ seem to interpolate those endpoint orderings, with some $Li^+$ occupying tetrahedral sites and the rest occupying the octahedral sites that do not share faces

with the occupied tetrahedral sites. This always leaves three vacant octahedral sites around each occupied tetrahedral site. The tetrahedral $Li^+$ can be situated in various ways, such as rows [Figure 4.13(c)] or more isolated arrangements [Figure 4.13(d)]. As shown in Figure S7 of the Supporting Information, configurations that follow this $Li^+$ ordering motif generally lie lower in energy than those that do not. While we calculated all such motif-based configurations in supercells up to five times the volume of the primitive cell volume, it is quite possible that there are additional stable $Li^+$ orderings following this pattern in larger supercells. The entropic potential determined from calorimetry clearly shows phase coexistence regions. These DFT calculations explicitly attribute the phase coexistence to $Li^+$ ordering and filling motifs that give rise to two distinct voltage plateaus in electrochemistry, closely matching experimental results.

## 4.5 Conclusion

$LiScMo_3O_8$ serves as an effective model system for examining the possibility that metal-metal bonding can be used as a design principle for electrode materials. Electrochemical studies show highly reversible and stable cycling in a voltage range that is appropriate for use in $Li^+$–ion batteries. *Operando* X-ray experiments suggest minimal strain in the crystal structure with lithiation, pointing to the rigidity of the structure arising from metal-metal bonding between Mo. Diffraction also reveals a two-phase region expected from the voltage profile. Raman spectroscopy clearly show lowering of symmetry that would also correspond to a phase change, and softening of vibrational modes associated with the triangular $Mo_3$ clusters. Potentiometric entropy measurements explicitly show phase coexistence regions. The calculated voltage curve shows close agreement to experimental electrochemistry and provides powerful insight at the

atomic level. Notably, detailed electronic structure calculations suggest that phase coexistence is associated with $Li^+$ ordering, as is also supported by the entropic potential measurements. The $Mo_3$ clusters in $LiScMo_3O_8$ effectively minimize structural changes because of the distributed charge. Understanding this unusual electrode material inspires the search for related materials for stable, low-strain electrodes.

# Chapter 5

# Electrochemical Control of Magnetism on the Breathing Kagome Network of $Li_xScMo_3O_8$

## 5.1 Abstract

Controlling properties within a given functional inorganic material structure type is often accomplished through tuning the electronic occupation, which is in turn dictated by the elemental composition determined at the time of material preparation. We employ electrochemical control of the lithium content, with associated electronic occupancy control, to vary the magnetic properties of a material where a kagome-derived network of $Mo_3$ triangles carry the spin. In this case, Li is electrochemically inserted

Reproduced with permission from K. E. Wyckoff, L. Kautzsch, J. L. Kaufamn, B. R. Ortiz, A. Kallistova, G. Pokharel, J. Liu, K. M. Taddei, K. M. Wiaderek, S. H. Lapidus, S. D. Wilson, A. Van der Ven, and R. Seshadri. Electrochemical Control of Magnetism on the Breathing Kagome Network of $Li_xScMo_3O_8$ *Chem. Mater.* 35(13), 4945–4954 (2023). 

into $LiScMo_3O_8$, a layered compound containing a breathing Mo kagome network. Up to two additional Li can be inserted into $LiScMo_3O_8$, transforming it into $Li_3ScMo_3O_8$. $Li_2ScMo_3O_8$ prepared by electrochemical lithiation is compared to the quantum spin liquid candidate compound $Li_2ScMo_3O_8$ prepared through high-temperature solid-state methods, that has a slightly different structural stacking sequence but a similar kagome-derived network. Magnetic measurements are supported by first-principles calculations, showing that electrons remain localized on the Mo clusters throughout the doping series. As $x$ is varied in $Li_xScMo_3O_8$, the measurements and calculations reveal the evolution from a diamagnetic band insulator at $x = 1$ to a geometrically frustrated magnet at $x = 2$, back to a diamagnetic insulator at $x = 3$. These results indicate a likelihood of strong coupling between the degree of Li disorder and charge/magnetic ordering over the $Mo_3$ clusters.

## 5.2 Introduction

While superficially appearing to comprise disjoint domains of investigation, magnetic materials and materials for electrochemical energy storage share a mutual reliance on the interplay between crystal and electronic structure, and oxidation state. Furthermore, these are often centered around d-block metals. A powerful example of this symbiosis is demonstrated by $LiCoO_2$, which was originally studied for its magnetic properties,[191] before it emerged much later to become the iconic cathode material.[192] Magnetic studies have continued to inform on the nature of several oxide cathode and anode materials.

In particular, magnetic studies have greatly impacted our understanding of complex mechanisms in a host of different material systems by probing electron spin.[193] De-

tailed study of the electronic phase diagram of $Li_xCoO_2$[194], $Li_{1-x}Fe_xMn_{1-x}PO_4$[195], and $LiNi_{0.8}Mn_{0.1}Co_{0.1}O_2$[196] using magnetometry has illuminated the sensitive influence of Li content on the complex electronic property evolution in these materials. In some members of the Wadsley-Roth family of fast-charging anode materials, magnetic measurements have been instrumental in supporting a hypothesized insulator to metal transition during cycling.[40, 42] Advances in *operando* magnetometry have additionally revealed important insights towards design strategies in Sn-based alloy anodes.[197] On the device side, magnetic sensing has been shown to be a highly sensitive and quantitative technique for ascertaining cell health.[198]

Here we describe an electrode system based on a compound that can display geometric magnetic frustration and is closely related to candidate quantum spin liquid compounds, where electrochemical lithium insertion dramatically impacts magnetic properties. Geometrically frustrated networks, where all magnetic exchange pathways cannot be satisfied simultaneously, often give rise to complex and unconventional magnetic ground states. Ising spins on a triangular lattice lead to a large number of degenerate ground states.[199] This degeneracy has proved to be a defining characteristic of frustrated magnets,[200] leading to a wide variety of behaviors such as quantum spin liquid states,[201] and possible superconductivity.[202, 203] Kagome networks are the maximally frustrated structures in 2D, and can be found in a variety of crystal structures. Characterized by corner-sharing triangles, the kagome network can be comprised of a wide variety of transition metals, such as Cu,[204] Mo,[205] Sn,[206] and V[207].

Mott insulator phases in the $(A_nB_m)Mo_3O_8$, with two-dimensional slabs of a breathing $Mo_3$ kagome network, serve as a useful platform to study and understand quantum cluster magnets [Figure 5.1]. Kagome nets are defined by fully corner-connected

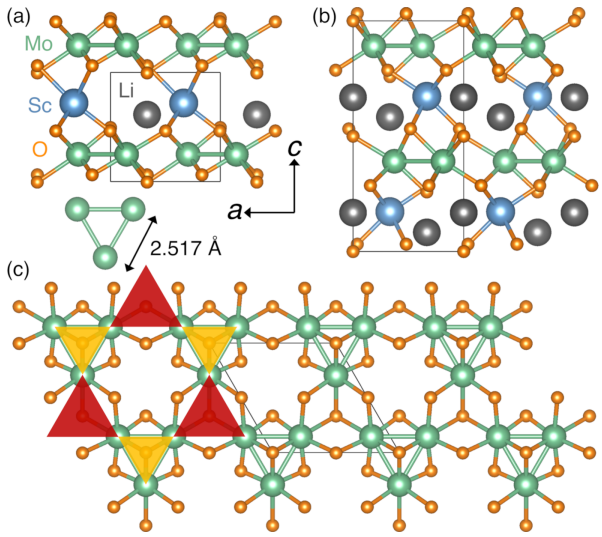


Figure 5.1: (a) Crystal structure of $LiScMo_3O_8$ (space group is $P3m1$, No. 156, O1 stacking) contains alternating layers of triangular clusters of metal-metal bonded Mo (green) atoms and $Li^+$ (grey)/Sc (blue). $Li^+$ is tetrahedrally coordinated. (b) Crystal structure of $Li_2ScMo_3O_8$ (h.t.) (space group is $P6_3mc$, No. 186, O2 stacking) contains slightly offset layers of triangular clusters of metal-metal bonded Mo atoms and $Li^+$/Sc. $Li^+$ is tetrahedrally coordinated.(c) Top view of two Mo-based breathing kagome-derived layers, indicated by the corner-connected smaller and larger triangles from $LiScMo_3O_8$, that is common to both structures.

equilateral triangles, and the term "breathing" here implies that alternate triangles are larger and smaller. The bonding scheme of these kagome networks allows for unpaired electrons to delocalize across clusters, as opposed to individual transition metals, and can serve as a structural platform to study exotic magnetism in extended solids. These Mo-based breathing kagome networks showcase notable diversity in magnetic behavior, even with seemingly minor variations in composition and structure.[208, 209] $LiZn_2Mo_3O_8$ is a cluster magnet that displays magnetic behavior[205] that is as-yet not well-understood. It has been postulated that the magnetic behavior may show features of a resonating valence-bond state,[210, 211] dimerization,[212], or plaquette charge order.[213, 214]

Recently, we showed that the breathing kagome-network compound $LiScMo_3O_8$, [Figure 5.1(a)] a diamagnetic insulator because of complete localization of two d electrons *per* Mo within Mo–Mo bonds, is an effective anode material for Li-ion batteries.[215] The related compound $Li_2ScMo_3O_8$, [Figure 5.1(b)] with an extra d electron for every 3 Mo also possesses a Mo-based breathing kagome network, shown in Figure 5.1(c), and is reported to be a frustrated cluster magnet,[190] with little sign of long range magnetic order down to $T = 0.5$ K. $Li_2In_{1-x}Sc_xMo_3O_8$ in contrast, where Sc is replaced by the smaller, isoelectronic In, has been noted to show antiferromagnetic long-range order through muon spin rotation experiments.[216]

Here, we have prepared the series of samples $Li_xScMo_3O_8$ in $x = 1.0$ to 2.85 by electrochemical insertion, and studied the evolution of magnetic properties *ex-situ*, across the series. Low temperature data show unusual behavior in electrochemically lithiated $Li_2ScMo_3O_8$ (e.c.) compared to high temperature $Li_2ScMo_3O_8$ (h.t.) phase, which has a distinctly different structure. Notably, the layer stacking in $Li_2ScMo_3O_8$ (e.c.) is O1 like the parent compound $LiScMo_3O_8$ [Figure 5.1(b)], while the layer stacking

in $Li_2ScMo_3O_8$ (h.t.) is O2. In neither case is the Li expected to be stable in prismatic coordination.[217] Density function theory-based electronic structure calculations have been carried out that aid in the interpretation of the magnetic moment evolution. Through electrochemistry we can realize magnetic states that we otherwise would not be able to access through conventional synthetic routes, with the potential to lead to discovery of more applied functionality in the future.[218]

## 5.3 Experimental Methods

### 5.3.1 Preparation of $LiScMo_3O_8$ and $Li_2ScMo_3O_8$

Pristine $LiScMo_3O_8$ was prepared through a conventional high-temperature solid state reaction of precursor oxide powders in a sealed vitreous silica tube. Trace quantities of $MoO_2$ were removed with a dilute nitric acid wash to produce the pure target compound. A more detailed procedure can be found elsewhere.[215] $Li_2ScMo_3O_8$ was prepared in a similar manner using identical precursor oxide powders in the appropriate stoichiometry. For this composition, the nitric acid wash was not necessary. Both materials were black powders. Structural studies of the pristine compounds $LiScMo_3O_8$ and $Li_2ScMo_3O_8$ were carried out using neutron powder diffraction on the NOMAD beamline at Oak Ridge National Laboratory.

### 5.3.2 Electrochemical lithation of $LiScMo_3O_8$

A wide range of electrochemically lithiated samples were prepared using $LiScMo_3O_8$ as the starting material. Swagelok cells were used to prepare large quantities of lithiated material $Li_xScMo_3O_8$ in precise 0.25 Li increments. It is customary to prepare

battery cells with additives such as binder and conductive carbons to improve transport and performance. For this study, all additives were omitted to maximize signal and avoid possible undesired magnetic contributions. Therefore, approximately 80 mg of pure starting $LiScMo_3O_8$ material was pressed in a 10 mm die to 4 tons to create a fragile, but thin and compact disk pellet. This pellet was delicately placed into a half assembled Swagelok cell. A glass fiber separator (Whatman GF/D) was gently placed on top of the pellet. This assembly was then pumped into an Ar-filled glovebox to complete the cell fabrication. Electrolyte (1 M $LiPF_6$ in ethylene carbonate/dimethyl carbonate (EC/DMC) 50/50 v/v Sigma Aldrich) was evenly dispersed on top of the separator. The quantity varied slightly, but enough electrolyte was used to just soak the separator. Polished Li foil was used as the counter electrode and only light pressure was used to close the cell to avoid pellet disintegration. The cells were then discharged to insert Li at very slow rates, ranging from C/80 (80 hour discharge) to C/130 (130 hour discharge). The C rate was determined assuming 2 Li insert into the structure. Cells were discharged using a VMP3 BioLogic potentiostat. Each electrochemically lithiated composition was prepared in a different Swagelok cell.

Samples for the low temperature neutron study on the WAND$^2$ beamline at ORNL were prepared in a very similar manner. There were two main differences. Importantly, the sample size was increased from approximately 80 mg in small Swagelok cells to upwards of 300 mg using larger custom Swagelok cells. The custom larger Swagelok cell design is identical to the smaller Swagelok, except for the body diameter. The smaller typical Swagelok cells have a diameter of 13 mm and the larger Swagelok cells used in this study have a diameter of 20 mm. The pellet preparation is identical for both cells in terms of diameter and mass of the pellet. The advantage for the larger cell comes because only one 80 mg pellet can fit in the normal Swagelok while it is possible

to fit approximately three of those same pellets in the large Swagelok. With this design, we can retain similar experimental parameters, but get larger yields of *ex-situ* powder. Second, instead of natural Li as the counter electrode, isotopically enriched $^7$Li was used to increase scattering quality. An overlay of representative discharge curves can be found in the Supporting Information (SI).

Following completion of electrochemical Li insertion, the cells were then pumped back into an Ar-filled glovebox and kept strictly air-free for preparation, storage, and all characterization techniques to avoid any possible sample decomposition. The cells were carefully taken apart and the lithiated pellets were removed and left to dry overnight. Then they were crushed and lightly ground, moved into a centrifuge tube, and washed in EC:DMC to remove any residual surface salts. The effluent was poured off and the powders were vacuum dried for 2 hr to 3 hr, followed by gentle grinding in an agate mortar and pestle, resulting in a fine, black powder. These electrochemically lithiated powders were the basis of all future measurements.

### 5.3.3 Diffraction data collection and reduction

Structural studies of the pristine compounds $LiScMo_3O_8$ and $Li_2ScMo_3O_8$ were carried out by collecting neutron total scattering data on the NOMAD beamline at Oak Ridge National Laboratory. For the current experiment, about 100 mg powder samples were loaded into 3 mm thin-walled quartz capillaries.[219, 220] Two 24 min scans (at 290 K) were collected for each sample and then summed together to improve the statistics of the data. Scattering signal from the empty quartz capillaries measurements was subtracted as background from the sample measurement and data were normalized by the scattering intensity from a 6 mm vanadium rod to account for incident spectrum profile and detector efficiencies.

Rietveld refinements to the previously published structures[146] were carried out in the TOPAS v6 software.[50] Time-of-flight (TOF) data were converted to $d$-spacing data using the conventional second order polynomial TOF = ZERO + DIFC$\times d$ + DIFA$\times d^2$, where the parameters ZERO and DIFC were determined from refinement of a standard NIST Si-640e data set and held fixed, while the parameter DIFA was allowed to vary during refinements to account for sample displacement. A back-to-back exponential function convoluted with a Pseudo-Voigt function was used to describe the peak profile.[221] Lorentz factor is corrected by multiplying $d^4$.[222]

Structural studies of the lithiated $Li_2ScMo_3O_8$ (e.c) material were carried out on the WAND$^2$ HB-2C beamline at HFIR at Oak Ridge National Laboratory. Electrochemically lithiated powder at this composition was pressed into a 6 mm pellet and placed in a sealed vanadium can inside of a glovebox. The sample was measured in field-cooled warming conditions at a field of $H$ = 3 T at temperatures ranging from $T$ = 2 K to $T$ = 30 K. Measurement time at each condition was correlated to the number of counts to ensure comparable data sets. Order parameters were calculated by integrating the intensity of each peak at every measured temperature.

*Operando* powder diffraction measurements were carried out at beamline 11-BM at the Advanced Photon Source at Argonne National Laboratory. All measurements were performed in an AMPIX cell[223] at room temperature in transmission geometry at wavelength ($\lambda$ = 0.458924 Å). Pressed pellet electrodes were made in a 6:2:2 (active: SuperP: PTFE) mass ratio. The electrode weighed 21.1 mg and was 10 mm in diameter. The AMPIX cell was assembled in an argon glovebox using lithium metal as the counter electrode, a glass fiber seperator (Whatman), and 1.0 M $LiPF_6$ dissolved in 1:1 v/v ethylene carbonate/diethyl carbonate (EC/DEC). The cell was cycled at a C/15 rate. The diffraction patterns for $Li_2ScMo_3O_8$ (e.c.) and $Li_3ScMo_3O_8$ (e.c.) were ex-

tracted from this data set and background subtracted from a blank AMPIX cell. Rietveld refinements were performed using the calculated $Li_2ScMo_3O_8$ (e.c.) and $Li_3ScMo_3O_8$ (e.c.) ground state structures. All visualization involving crystal structures was carried out using VESTA.[51]

### 5.3.4 Characterization

Magnetic measurements were carried out on a Quantum Design MPMS3 SQUID magnetometer. Powder masses of approximately 5 mg were measured in polypropylene capsules. All samples were packed in an Ar-filled glovebox and kept in a vacuumed transfer container until just prior to MPMS loading. DC susceptibility measurements were collected in both field-cooled warming (FCW) and zero-field-cooled warming (ZFCW) conditions with applied magnetic fields $H$ ranging from $H = 0.01$ T to $H = 5$ T in the temperature range $T = 2$ K to $T = 400$ K. Heat capacity measurements were carried out on a Quantum Design PPMS. The electrochemically lithiated powder was pressed inside of an Ar-filled glovebox to form a small pellet. This pellet was kept in a vacuumed transfer container until just before loading onto the heat capacity puck outside of the glovebox. The material was exposed to air for less than 1 min before PPMS measurement. Sintered pellets of $LiScMo_3O_8$ and $Li_2ScMo_3O_8$ (h.t.) were used to measure electrical resistivity in a Quantum Design PPMS. Gold wires were attached to the samples using silver paint to perform a four-point measurement.

### 5.3.5 Computational Methodology

Electronic structure calculations using density functional theory (DFT) were performed with the Vienna *ab initio* Simulation Package (VASP) [166–169]. The Li sv, Sc

sv, Mo sv, and O projector augmented wave (PAW) pseudopotentials [61, 170] were used with a plane-wave energy cutoff of 650 eV. Γ-centered Monkhorst-Pack $k$-meshes [174] were automatically generated with a density of 40 Å and integrated using the linear tetrahedron method [175]. The SCAN meta-GGA functional [172, 173] was employed to approximate the exchange-correlation energy.

## 5.4 Results and Discussion

### 5.4.1 Electronic structure

The crystal structure of $LiScMo_3O_8$ serves as the model platform for this study. $LiScMo_3O_8$ is a layered structure, with alternating layers of Mo and Li/Sc, as shown in Figure 5.1(a). The Mo layer is comprised of a Mo kagome network, built of metal-metal bonded $MoO_3$ clusters. In the alternating layer, Sc is octahedrally coordinated and Li is tetrahedrally coordinated. Bond valence sum mapping has shown that the Li/Sc layer has channels that allow for low-energy two dimensional Li diffusion pathways. It has also been shown recently that Li insertion into the structure is highly stable and reversible, with minimal changes or expansion of the network.[215] The starting oxidation state of Mo in this structure is $Mo^{4+}$, and previous electrochemistry of the compound shows that up to two additional Li can be inserted to achieve a total Li content of $Li_3ScMo_3O_8$. The parent structure is very similar to the more studied $Li_2ScMo_3O_8$ (h.t.) in Figure 5.1(b). $Li_2ScMo_3O_8$ is an established quantum spin liquid candidate with one unpaired $e^-$ per $Mo_3$ cluster.[190, 209, 216, 224] Compared to $LiScMo_3O_8$, the Mo layers in this structure are slightly offset from each other and the Li occupy both sublattices of tetrahedral sites, rather than just one. The Mo layer of

$LiScMo_3O_8$ is shown in Figure 5.1(c) with oxygen connectivity.

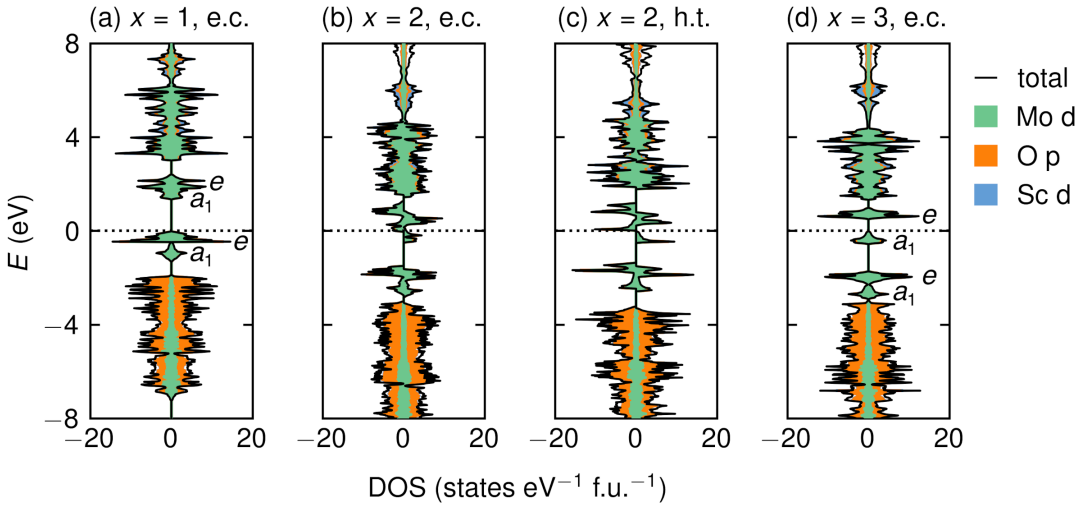


Figure 5.2: Spin-polarized density of states of $Li_xScMo_3O_8$ in either the electrochemical or high temperature structure at (a) $x = 1$, (b,c) $x = 2$, and (d) $x = 3$. The DOS calculations were performed by Jonas L. Kaufman.

To better understand the relationship between the crystal structure and electronic structure of $Li_xScMo_3O_8$, DFT-based electronic structure calculations are used to provide qualitative insight about this material at different Li, or doping, levels. The density of states for pristine $LiScMo_3O_8$ is shown in Figure 5.2(a), annotated with the corresponding energy levels. The density of states shows filled Mo d-states just below the Fermi level, a large band gap, and no unpaired $e^-$, indicative of an insulator. If one additional Li is inserted into the structure, the nominal composition becomes $Li_2ScMo_3O_8$ and results in one unpaired $e^-$ according to the energy level diagram displayed in Figure 5.3. The density of states for this composition is displayed in Figure 5.2(b) and shows that the spins become polarized. The states remain very localized, however, and the small dispersion indicates it is unlikely this material would be a good conductor.

Figure 5.2(c) shows the analogous density of states for the solid state preparation of $Li_2ScMo_3O_8$ (h.t.). Globally, the features in the density of states between $Li_2ScMo_3O_8$

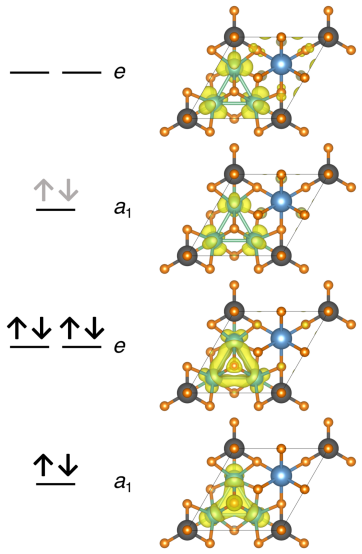


Figure 5.3: Left: Orbital energy level diagram for a single $Mo_3$ cluster, with black arrows showing the electron filling at $x = 1$ ($[Mo_3]^{12+}$) and gray arrows showing the additional electrons at $x = 3$ ($[Mo_3]^{10+}$). Right: Partial charge densities corresponding to the lower and upper $a_1$ and $e$ states of a $Mo_3$ cluster in $LiScMo_3O_8$. The partial charge densities were calculated by Jonas L. Kaufman.

(e.c.) prepared electrochemically and $Li_2ScMo_3O_8$ (h.t.) prepared through solid state methods are close in semblance. If two additional Li are inserted into $LiScMo_3O_8$ to get a composition of $Li_3ScMo_3O_8$, the $a_1$ energy level fills and the electrons pair up. The density of states in Figure 5.2(d) shows that the gap between filled and unfilled states is much smaller than the pristine material, but a localized and insulating state is still expected. Electrical resistivity measurements (shown in the SI) on $LiScMo_3O_8$ and $Li_2ScMo_3O_8$ (h.t.) indeed show that $LiScMo_3O_8$ is orders of magnitude more resistive than $Li_2ScMo_3O_8$ (h.t.), and that $Li_2ScMo_3O_8$ (h.t.) displays not metallic, but semiconducting behavior. The electronic structure calculations and energy level diagram will be an important point of reference as we experimentally explore electrochemical doping of the $LiScMo_3O_8$ structure.

Figure 5.3 illustrates the partial charge densities corresponding to the lower and upper $a_1$ and $e$ states of a $Mo_3$ cluster in $LiScMo_3O_8$. Parent material $LiScMo_3O_8$ begins

with the lower $a_1$ and $e$ states completely filled. The charge density for these states is localized on the $Mo_3$ cluster, distributed along their shared oxygen bonds and metal-metal bonds, respectively. As Li and electrons are inserted and fill the upper $a_1$ state, the charge density localizes on the individual Mo atoms.

### 5.4.2 Diffraction and Electrochemistry

Both the starting material $LiScMo_3O_8$ and $Li_2ScMo_3O_8$ (h.t.) were characterized with neutron powder diffraction at the NOMAD beamline located at Oak Ridge National Laboratory. Rietveld refinements of both materials show good agreement with the accepted structures and can be found in the SI. An *operando* cycling experiment was performed at beamline 11-BM at Argonne National Laboratory to understand the structural evolution of the material $LiScMo_3O_8$ with lithium insertion and deinsertion. Figure 5.4 shows the electrochemisty and corresponding diffraction data over two complete galvanostatic cycles. As lithium is inserted, diffraction data indicate that the structure experiences minimal changes. The slight shifts and emergence of new peaks are both reversible and consistent with phase-coexistence regions. Although these features agree well with a previous *operando* lab powder x-ray diffraction experiment,[215] higher resolution synchrotron data allows for Rietveld refinements to the calculated ground state structures.

The black arrows in Figure 5.4 indicate the diffraction data that was extracted from the *operando* cycling experiment, corresponding to compositions $Li_2ScMo_3O_8$ (e.c.) and $Li_3ScMo_3O_8$ (e.c.). Figure 5.5 shows the Rietveld refinements for both materials using their respective ground state structures determined from ab-initio calculations. Refinement of $Li_2ScMo_3O_8$ (e.c.) is displayed in Figure 5.5 (a) and Figure 5.5 (b) shows the refinement of $Li_3ScMo_3O_8$ (e.c.), close to the maximum lithiation amount. Com-

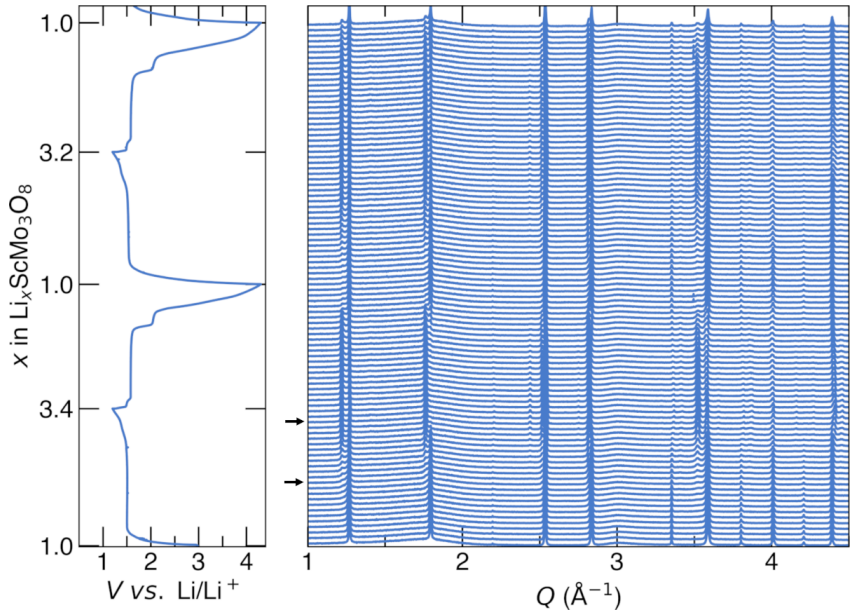


Figure 5.4: *Operando* synchrotron X-ray diffraction collected at 11-BM at APS of $LiScMo_3O_8$ during the first two galvanostatic discharge/charge cycles at a C/15 cycling rate. The electrochemistry is shown in the left panel. Arrows indicate the traces that were extracted from the data set and refined in Figure 5.5.

parison of these individual diffraction traces more clearly highlights the emergence of additional diffraction peaks at low $Q$. Agreement between the experimental and calculated structures confirms the nuanced differences in the crystal structures at different lithiation levels.

The crystal structures of the thermally prepared compounds $LiScMo_3O_8$ and $Li_2ScMo_3O_8$ (h.t.) are shown in Figure 5.6 (a) and Figure 5.6 (b), respectively. The intralayer view of these structures again showcases the differences in layer stacking, with offset Mo layers in the $Li_2ScMo_3O_8$ (h.t.) material. Refined crystal structures of electrochemically prepared compounds $Li_2ScMo_3O_8$ (e.c.) [Figure 5.6 (c)] and $Li_3ScMo_3O_8$ (e.c.) [Figure 5.6 (d)] from the data shown in Figure 5.5 are shown below the thermally prepared compounds. While $Li_2ScMo_3O_8$ (h.t.) has offset Mo layers, $Li_2ScMo_3O_8$ (e.c.) and $Li_3ScMo_3O_8$ (e.c.) retain the same layer stacking as parent material $LiScMo_3O_8$.

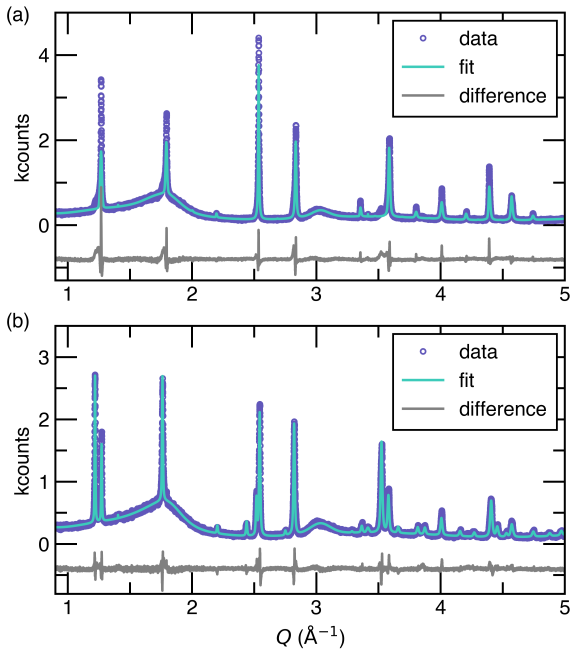


Figure 5.5: Rietveld refinements of (a) $Li_2ScMo_3O_8$ (e.c.) and (b) $Li_3ScMo_3O_8$ (e.c.) of *operando* synchrotron powder diffraction data collected at 11-BM at APS. These diffraction patterns were extracted from the *operando* AMPIX experiment and fit to the calculated ground state structures. The backgrounds were fit and only the lattice parameters and transition metal sites were allowed to refine. The refined crystallographic parameters can be found in the SI.

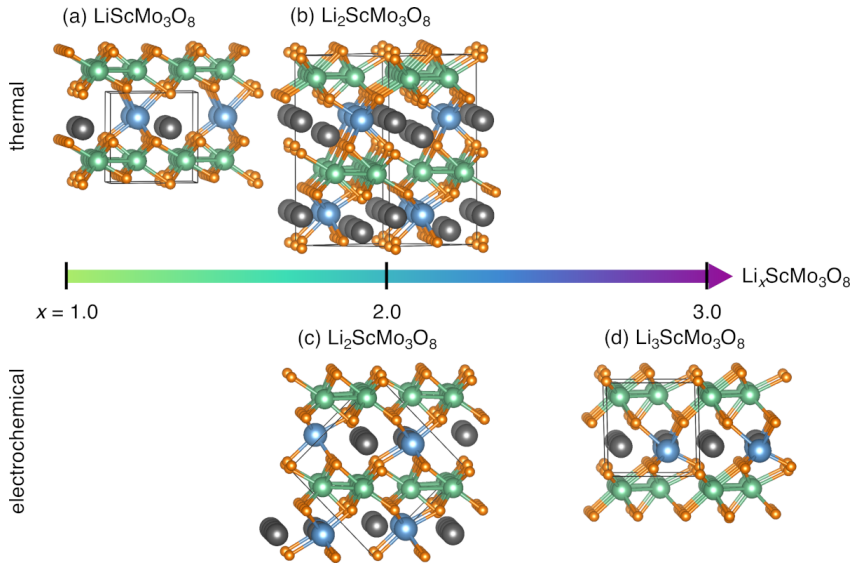


Figure 5.6: Diagram comparing the intralayer view of the discussed crystal structures. The top compounds (a) $LiScMo_3O_8$ and (b) $Li_2ScMo_3O_8$ (h.t.) are prepared through conventional high temperature methods and the compounds (c) $Li_2ScMo_3O_8$ (e.c.) and (d) $Li_3ScMo_3O_8$ (e.c.) are prepared electrochemically. $Li_2ScMo_3O_8$ (h.t.) shown in (b) has offset Mo layers with O2 stacking, while $LiScMo_3O_8$ in (a), and electrochemically prepared materials (c) $Li_2ScMo_3O_8$ (e.c.) and (d) $Li_3ScMo_3O_8$ (e.c.) have O1 stacking.

Figure 5.7 shows an analogous comparison of the breathing kagome networks of these materials. Notably, the Mo layers in $LiScMo_3O_8$ [Figure 5.7 (a)] are aligned, while the offset Mo layers of $Li_2ScMo_3O_8$ (h.t.) [Figure 5.7 (b)] with O2 stacking is prominent. Electrochemically prepared $Li_2ScMo_3O_8$ [Figure 5.7 (c)] and $Li_3ScMo_3O_8$ (e.c.)[Figure 5.7 (d)] have very similar breathing kagome networks as the parent material. A "breathing ratio" can be calculated to better understand bond distances and connectivity in this type of kagome network, defined by the bond distance of the larger triangles divided by the bond distance of the smaller triangles, $\lambda = d_{\triangledown}/d_{\triangle}$. The $\lambda$ for the starting material $LiScMo_3O_8$ is 1.27 and the $\lambda$ for $Li_2ScMo_3O_8$ (h.t.) is 1.28. From this standpoint, the kagome networks of these two materials are very similar and close to previous reports.[216] We find that electrochemical insertion of Li does not significantly alter $\lambda$. $Li_2ScMo_3O_8$ (e.c.) has a $\lambda$ of 1.27, while $Li_3ScMo_3O_8$ (e.c.) has a $\lambda$ of 1.24 . The slightly lower value of $\lambda$ indicates that this material is closer to an ideal kagome network, where the bond lengths would all be equal. As Li is inserted, electrons begin to populate the antibonding $a_1$ states, as discussed in the next section.

### 5.4.3 Magnetic properties

It is possible to directly insert additional Li into $LiScMo_3O_8$ by using Li metal as the counter electrode while discharging a battery cell. Samples were prepared by electrochemically inserting Li into $LiScMo_3O_8$ in $x = 0.25$ increments. As opposed to more traditional coin cells that handle cast electrodes with a low material loading (up to 10 mg cm$^{-2}$), Swagelok cells are amenable to much higher loading (up to 80 mg cm$^{-2}$) and can be disassembled in a glovebox to recover *ex-situ* material. The SI carries a depiction of an actual Swagelok cell, with a scheme of a typical internal battery stack. Galvanostatic cycling was used to apply a constant current until the specified Li content

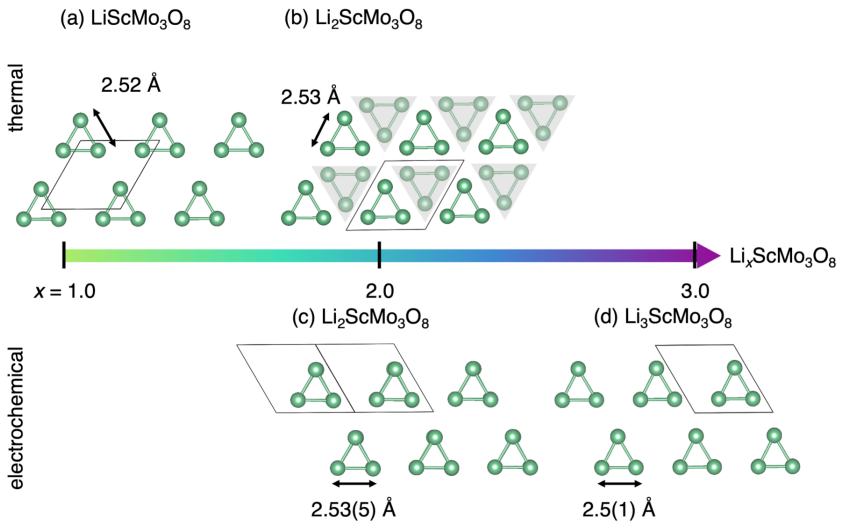


Figure 5.7: Diagram comparing the breathing kagome networks of the discussed crystal structures. Compounds (a) $LiScMo_3O_8$ and (b) $Li_2ScMo_3O_8$ (h.t.) are prepared through conventional high temperature methods and compounds (c) $Li_2ScMo_3O_8$ (e.c.) and (d) $Li_3ScMo_3O_8$ (e.c.) are prepared electrochemically. In (b), the two distinct layers of $Mo_3$ triangles are displayed with one of the layers being shaded. Average Mo–Mo bond distances are similar between the compounds.

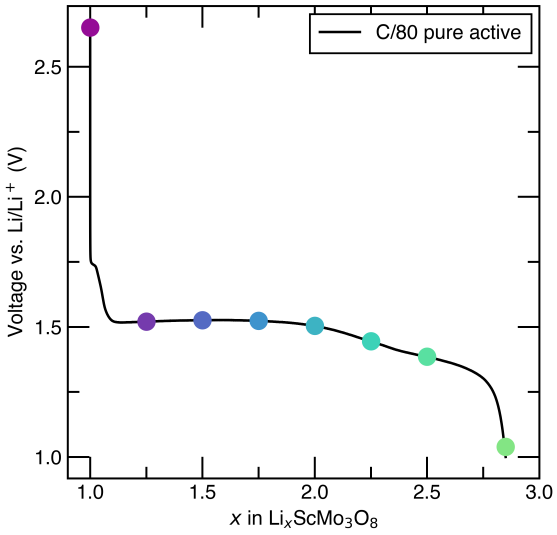


Figure 5.8: Electrochemical insertion of Li into $LiScMo_3O_8$ in a Swagelok cell. No binder or carbon was used for the electrochemistry. Each point on the discharge curve represents a single battery that was stopped in $x = 0.25$ increments. Galvanostatic cycling was performed at slow rates of C/80.

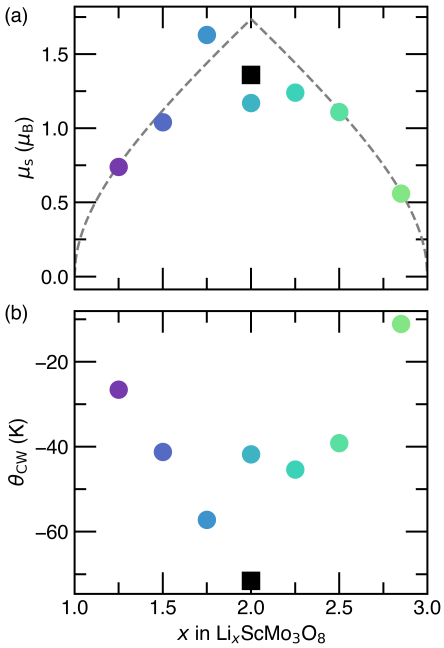


Figure 5.9: Summary of spin-only moment and Curie-Weiss temperatures extracted from Curie-Weiss fits as a function of $x$. Individual fits can be found in the SI. Colored points represent electrochemically lithiated $LiScMo_3O_8$ (e.c.) samples and the square black points represent the high temperature $Li_2ScMo_3O_8$ (h.t.) sample. (a) $\mu_s$ gives insight into the number of unpaired $e^-$ in the system. $\mu_s$ increases until approximately $x = 2.0$ and then collapses back to original value. The grey dashed line represents the calculated spin only magnetic moment for one unpaired $e^-$. (b) Curie-Weiss temperature ($\theta_{CW}$) as a function of $x$ shows increasing AFM exchange strength towards $x = 2$, decreasing past this point.

was reached. Figure 7.19 shows an actual discharge curve of pure active material at a slow cycling rate. Each point on the curve represents an individual battery cell and the shapes of all of the experimental voltage curves match the expected electrochemistry for this material, including the characteristic 1.5 V plateau.[215] The cells were brought back into the glovebox, disassembled, and prepared for subsequent characterization.

Combining the results of the Curie-Weiss fits with the calculated charge densities provides a comprehensive picture of electron filling and localization for this Mo-based

cluster magnet. SQUID magnetometry was used to measure the susceptibility of each electrochemically prepared sample at $H = 0.1\,\mathrm{T}$ between $T = 2\,\mathrm{K}$ and $T = 300\,\mathrm{K}$. An overlay of these susceptibility curves (shown in the SI) show clear evolution with varying Li content. At room temperature, the susceptibility is negative, consistent with diamagnetic behavior. As the Li content is increased, the susceptibility gradually increases until approximately $x = 2.0$. After this point, the susceptibility decreases, collapsing near the value of the original un-lithiated material. This is in qualitative agreement with the proposed energy level diagram.

Curie-Weiss fits to the susceptibility measurements can additionally provide more quantitative insight. Figure 5.9 summarizes the spin-only moments ($\mu_s$) and Curie-Weiss temperatures ($\theta_{\mathrm{CW}}$) as a function of Li content. The trend visualized in the raw susceptibility data is reflected in the Curie-Weiss spin-only moments shown in Figure 5.9(a). As Li is inserted into $LiScMo_3O_8$, $\mu_s$ increases, maximizing around $x = 2.0$. Upon further lithiation, $\mu_s$ decreases back down. This trend fairly accurately tracks with the calculated spin only magnetic moment for one unpaired $e^-$. Experimental agreement with the calculated moment definitively confirms an electronic picture in which inserted electrons remain localized on the $Mo_3$ clusters. We note that the $\mu_s$ value of the $Li_2ScMo_3O_8$ (e.c.), a colored point, and $Li_2ScMo_3O_8$ (h.t.), a black square, are similar, indicating that the overall Li and electron counts for both compounds are very close.

Figure 5.9(b) shows that the Curie-Weiss temperatures also show a decisive trend. For the entire series, $\theta_{\mathrm{CW}}$ is negative and decreases further with additional lithiation. The maxima in $\mu_s$ correlates to a minima in $\theta_{\mathrm{CW}}$, at values near $x = 2.0$. $\theta_{\mathrm{CW}}$ becomes less negative past this point. Negative $\theta_{\mathrm{CW}}$ values indicate that the exchange in this system is dominated by AFM interactions that get stronger as the number of un-

paired $e^-$ maximizes. Unlike the close agreement between the $Li_2ScMo_3O_8$ (e.c.) and $Li_2ScMo_3O_8$ (h.t.) samples for $\mu_s$, there is a notable difference in $\theta_{CW}$. This likely stems from key differences between the two compounds relating to a combination of Li and charge ordering which will be discussed later.

### 5.4.4 Low-temperature magnetic properties

We observe notable low-temperature magnetic behavior in electrochemically lithiated $LiScMo_3O_8$. As demonstrated previously, we observe high-temperature behavior consistent with electron localization. However, at low temperatures, intermediate Li compositions ($x = 1.25 \breve{} 2.50$ in $Li_xScMo_3O_8$) all display a prominent feature at 12 K in susceptibility measurements, namely an abrupt change in slope. All of the temperature-dependent susceptibility traces, offset along the $y$-axis for clarity, are displayed in the SI. As more Li and electrons are introduced into the system, the slope change becomes steeper and the feature onset subtly increases until approximately $x = 2.0$. This suggests a possible correlation of the feature with both the maxima in $\mu_s$ and minima in $\theta_{CW}$. Both the slope and onset temperature decrease until maximum lithiation at $x = 2.85$, when the upper $a_1$ state is nominally filled and the low-temperature feature disappears.

To gain more understanding related to the origin of this feature we compare electrochemically lithiated $Li_2ScMo_3O_8$ (e.c.) to high-temperature $Li_2ScMo_3O_8$ (h.t.). Figure 5.10(a) compares the low-temperature susceptibility of both compounds. $Li_2ScMo_3O_8$ (h.t.) shows no signs of long-range magnetic order to 2 K, consistent with literature on this quantum spin liquid candidate.[190] Conversely, $Li_2ScMo_3O_8$ (e.c.) displays a sharp slope change at 12 K. To confirm that the feature is a bulk property, heat capacity measurements in Figure 5.10(b) show a relatively broad peak that begins at the same

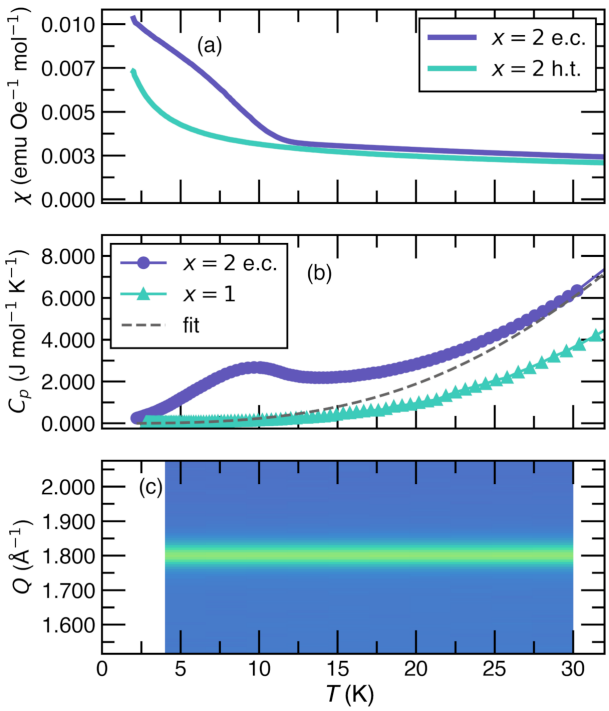


Figure 5.10: (a) Comparison of susceptibility measurements at $H = 0.1\,\mathrm{T}$ between the $Li_2ScMo_3O_8$ system prepared electrochemically (e.c.) and prepared through high--temperature solid state routes (h.t.). The h.t. sample is a reported quantum spin liquid and shows no long range magnetic order down to 2 K while the e.c. sample shows a feature, namely a prominent change in slope, at 12 K. (b) Heat capacity in zero applied field of the parent material $LiScMo_3O_8$ and $Li_2ScMo_3O_8$ (e.c.) shows a broad low temperature peak in the electrochemically lithiated sample. The dashed line is the fit of a model to a double-Debye function with two characteristic Debye temperatures. (c) Heat map of the integrated intensity of the $(31\bar{1})$ diffraction peak shows negligible changes in intensity in the temperature region of interest for the $Li_2ScMo_3O_8$ (e.c.) sample.

temperature as the slope change in susceptibility. The heat capacity of the parent material $LiScMo_3O_8$ is smooth down to 2 K. The heat capacity data of $Li_2ScMo_3O_8$ (e.c.) were fit to a double-Debye function from 120 K and extrapolated down to 0 K from the equation in Fortes et al.[225] The peak feature was excluded from the range. The parameters resulting from the fit of this function to $C_p$ are; $\theta_D^A = 717$ K, $\theta_D^B = 227$ K, $X = 0.89$, and $Y = 0.09$. The magnetic heat capacity was calculated by subtracting out the feature from the double-Debye fit. The integrated entropy as a function of temperature was found to be $S_m = 3.3\,\mathrm{J\,mol^{-1}\,K^{-1}}$ (figure displayed in the SI). For non-interacting spins that can be in one of two discrete states, the configurational entropy per mole would be $S_m = R\ln(2)$. This is an upper bound for the configurational entropy for discrete degrees of freedom. Even with a 20% error related to an undermeasurement of the sample mass, the integrated intensity would be $S_m = 4.3\,\mathrm{J\,mol^{-1}\,K^{-1}}$ , still considerably lower than the upper bound. Although this experimental value of $S_m = 3.3\,\mathrm{J\,mol^{-1}\,K^{-1}}$ is lower compared to the expected value of $S_m = R\ln(2) = 5.76\,\mathrm{J\,mol^{-1}\,K^{-1}}$ for a spin 1/2 system, the relative order of magnitude of the experimental magnetic entropy is consistent with a bulk property of this system. There are a number of possible reasons for a lower value, including spin-orbit coupling effects. With one $e^-$ distributed over three Mo atoms, any type of ordering in this system will be extremely subtle and difficult to fully establish. However, the heat capacity data qualitatively indicate a bulk transition, rather than possible impurity spins.

Despite the difficulty involved with the measurements and data interpretation, we turn to low-temperature neutron measurements in an effort to shed more light on a possible mechanism. There are no new magnetic peaks that appear below the feature temperature. A heat map of the integrated intensity of the $(31\bar{1})$ peak in Figure 5.10(c) shows negligible changes in intensity over the measured temperature range. The inten-

sity changes for all peaks can be found in the SI. We find that the integrated intensity of the diffraction peaks remain constant where there are clear features found in susceptibility and heat capacity. We have established that nominally, the composition, structure, and density of states for both compounds are closely related. This raises the question of what is driving a low temperature feature in the electrochemically prepared material but not in the material prepared at high temperatures.

### 5.4.5 Coupling between charge, spin, and Li ordering

Previously we established a comprehensive picture of Li ordering in $Li_xScMo_3O_8$, in which the Li ions occupy only tetrahedral sites at $x = 1$, only octahedral sites at $x = 3$, and a mixture at intermediate $x$.[215] We also confirmed a preference for AFM coupling of the $Mo_3$ cluster moments at intermediate Li compositions ($1 < x < 3$), which in some cases even emerges when they are initialized ferromagnetically in DFT. At off-stoichiometric compositions, we expect electrons to remain localized and for there to be a mixture of oxidation states of the $Mo_3$ clusters. Indeed, analyzing the low-energy configurations considered previously reveals clear charge ordering, which can be inferred from both the average Mo-Mo bond length and total magnetic moment of each cluster.[215]

One such configuration at $x = 2.5$, shown in Figure 5.11, serves as an example of the coupling between charge, spin, and Li ordering in this system. The Li are arranged in a row ordering, with rows of tetrahedrally coordinated Li between regions of octahedrally coordinated Li. Of the four unique $Mo_3$ clusters, two have an oxidation state of 10+ and two have an oxidation state of 11+. The latter are arranged directly next to one another and carry magnetic spins which are antiparallel (along one direction of the supercell), consistent with AFM coupling. Finally, counting the number of shared

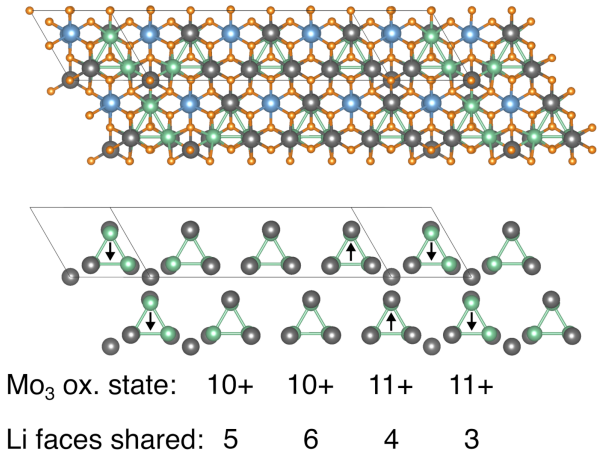


Figure 5.11: Full and simplified structure of a low-energy row ordering of Li at $x = 2.5$, annotated with the spin, formal oxidation state, and number of faces shared with Li octahedra (above and below) for each distinct $Mo_3$ cluster. These calculations were performed by Jonas L. Kaufman.

faces between Mo and Li octahedra reveals that the $[Mo_3]^{11+}$ clusters each share fewer Li faces than do the $[Mo_3]^{10+}$ clusters. This coupling serves to reduce the electrostatic energy penalty associated with face-sharing, as the clusters with higher oxidation state have fewer shared faces.

While this particular configuration is not expected to be a ground state of the true system, it illustrates the complex interplay between the different degrees of freedom. Even in the absence of long-range Li ordering, we expect that short-range Li ordering may couple to charge and spin ordering in a similar way. The role of Li ordering may explain differences in the magnetic behavior of the solid state and electrochemically prepared structures, since the two structures have different topologies of Li sites despite being composed of the same $Mo_3$ building blocks. In the $Li_2ScMo_3O_8$ (h.t.) structure, Li occupies only tetrahedral sites (which do not share faces with Mo octahedra) and each Mo has an identical environment. In the $Li_2ScMo_3O_8$ (e.c.) structure, due to the mixed tetrahedral/octahedral Li occupancy, some Mo share more faces with Li than others, spurring charge ordering at slightly off-stoichiometric $x$. Our results indicate that it is

highly likely that this low temperature feature must be related to spin-spin correlations induced locally by Li ordering into $[Mo_3]^{11+}$ clusters. Electrochemical lithiation makes it difficult to deconvolute the effects of intrinsic Li ordering versus inhomogeneous lithiation, but regardless, Li ordering lowers the symmetry of the structure, lifts degeneracy, and can relieve magnetic frustration. The lifting of degeneracy due to Li ordering is reminiscent of spin-Jahn-Teller−ordering in geometrically frustrated magnetic oxide spinels.[226]

## 5.5 Conclusion

We demonstrate the utility of electrochemistry to precisely control the electron filling in a magnetic material. $LiScMo_3O_8$ has a Mo-based kagome network and serves as an effective platform for this study because this material is both a good lithium ion conductor and is closely related to quantum spin liquid candidate $Li_2ScMo_3O_8$. Here, lithium was electrochemically inserted into the parent structure $Li_xScMo_3O_8$ from $x = 1.25$ to $x = 2.85$ by discharging a Swagelok cell versus Li metal. The resulting materials were characterized with magnetic measurements and showed that doped electrons remain localized on the $Mo_3$ clusters and agree with the proposed energy level diagram. DFT-based electronic structure calculations confirm localized partial charge densities and small dispersion for filled states. We find that metallicity cannot be induced through doping of a Mo kagome network and that it is unlikely to be realized in related systems. Low-temperature measurements indicate a spin correlation feature in electrochemically lithiated $Li_2ScMo_3O_8$ (e.c.) not present in high temperature $Li_2ScMo_3O_8$ (h.t.). This work indicates a likely coupling between charge, spin, and Li ordering due to electrochemical Li insertion. This study showcases how electrochem-

istry can serve as an avenue to tune the electronic structure in a frustrated magnetic material and provides additional understanding in the role of disorder in Mo-based kagome cluster magnets.

# Chapter 6

# Conclusion and Outlook

As battery technology is increasingly adopted globally, there are huge parallel efforts from academia and industry. Although these efforts have largely different driving forces, there is still great potential for influence, impact, and synergy between the two. Because of the complexity and scale of $Li^+-$ion batteries, there are an expanding number of fundamental research questions that align with academic and industry interests. These include, but are not limited to; performance, cost, longevity, recylability, and environmental impact of materials and their preparation processes. The work encompassed here focuses on performance and longevity of $Li^+-$ion battery anode materials.

This thesis is the product of an academic research environment, with the driving force to advance our fundamental understanding of materials science and inorganic chemistry related to electrode materials in $Li^+-$ion batteries. Electrochemical studies of $(W_{0.2}V_{0.8})_3O_7$ in Chapter 2 show that this vanadium-rich shear-structured Wadsley$-$Roth phase is a promising high-rate electrode material. This study demonstrated similar fast-charging capabilities between both large and small particles, indi-

cating that the atomic-scale crystallographic features, namely a combination of edge- and corner-sharing polyhedra, truly drive the intrinsic rate performance in these systems. This compound additionally stores more charge at higher voltages than most other reported Wadsley–Roth compounds and points to promising directions for tuning the voltage in this high-performance class of electrode materials. Data-mining efforts in Chapter 3 differentiate and explore the differences in performance more broadly between materials in this family. Despite similar charge storage mechanisms, we have shown that there are measurable differences in their fast-charging capabilities. By defining a new metric that we term edge-sharing density, we show that the capacity retention percents from 1C to 10C increase with decreasing edge-sharing density. These data show that the relative amount of edge-sharing features in a given crystal structure directly influences the rate performance, providing a clear design strategy when selecting and developing fast-charging electrode materials.

Inspired by the findings in Chapter 2 and Chapter 3 on shear structures, Chapter 4 explores metal-metal bonding as an unexplored electrode design principle in $LiScMo_3O_8$. Electrochemical studies show highly reversible and stable cycling in a voltage range that is appropriate for use in $Li^+-$ion batteries. *Operando* X-ray experiments suggest minimal strain in the crystal structure with lithiation, pointing to the rigidity of the structure arising from metal-metal bonding between Mo. The $Mo_3$ clusters in this unusual electrode material were found to effectively minimize structural changes because of the distributed charge. Chapter 5 more deeply explores the relationship between electrochemistry and the electronic structure in this system. We demonstrate the utility of magnetic measurements as an indirect probe of the evolution of the electronic structure of $LiScMo_3O_8$ with lithiation. We find that metallicity cannot be induced through doping of the Mo kagome network and that this work indicates a likely cou-

pling between charge, spin, and $Li^+$ ordering due to electrochemical Li insertion.

Regardless of the commercial utility of the materials explored in this thesis, there is significant value to expanding our understanding of structure−property relationships in inorganic chemistry, even beyond battery applications. This work provides new insight into insulator-metal transitions, ion mobility in crystal structures, crystal structure rigidity and bonding, and electronic structure evolution in transition metal oxide materials. The materials examined in this work serve as models to more finely understand how we can strategically tune material properties through intentional design of the crystal structure. The studies presented in this thesis ultimately provide more clear design strategies when selecting and developing fast-charging electrode materials for $Li^+$−ion batteries.

# Chapter 7

# Appendix

## 7.1 Supporting Information for Chapter 2

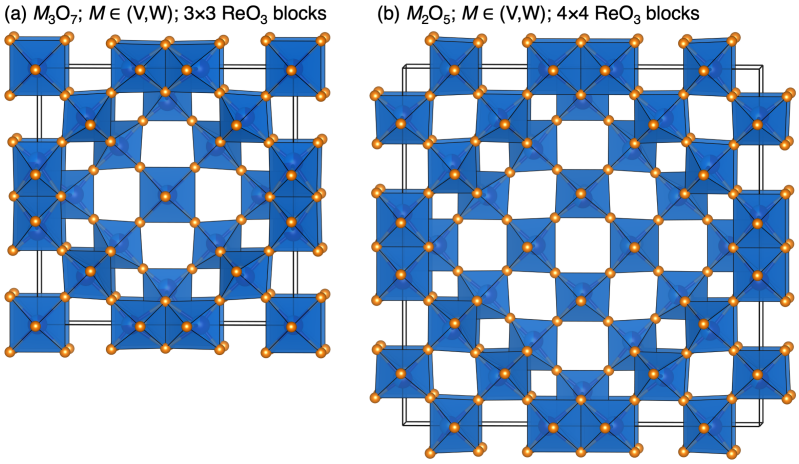


Figure 7.1: (a) The crystal structure of $(W_{0.2}V_{0.8})_3O_7$ is comprised of 3×3 blocks of octahedra, offset and connected through edge-sharing shear planes. The space group is $I4/mmm$. (b) The crystal structure of $(W_{0.35}V_{0.65})_2O_5$ is comprised of 4×4 blocks of octahedra, offset and connected through edge-sharing shear planes. The space group is also $I4/mmm$.

Table 7.1: Summary of refinement parameters from Figure 2 in the main text for Conv. $(W_{0.2}V_{0.8})_3O_7$.

| $(W_{0.2}V_{0.8})_3O_7$ | | $(W_{0.35}V_{0.65})_2O_5$ | |
|---|---|---|---|
| parameter | value | parameter | value |
| lattice constant | $a$ = 14.00277(3) Å<br>$c$ = 3.71467(2) Å | lattice constant | $a$ = 19.55304(8) Å<br>$c$ = 3.70849(7) Å |
| space group | $I_4/mmm$ | space group | $I_4/mmm$ |
| block size | 3×3 | block size | 4×4 |
| percent | 91% | percent | 9% |
| $R_{wp}$ | 13.91 | | |
| $R_{exp}$ | 6.21 | | |
| GOF = $R_{wp}/R_{exp}$ | 2.24 | | |

Table 7.2: Summary of refinement parameters from Figure 2 in the main text for FD $(W_{0.2}V_{0.8})_3O_7$.

$(W_{0.2}V_{0.8})_3O_7$

| parameter | value |
|---|---|
| lattice constant | $a$ = 14.01155(5) Å |
| | $c$ = 3.71502(9) Å |
| space group | $I_4/mmm$ |
| block size | 3×3 |
| percent | 100% |
| | |
| $R_{wp}$ | 12.30 |
| $R_{exp}$ | 6.47 |
| GOF = $R_{wp}/R_{exp}$ | 1.90 |

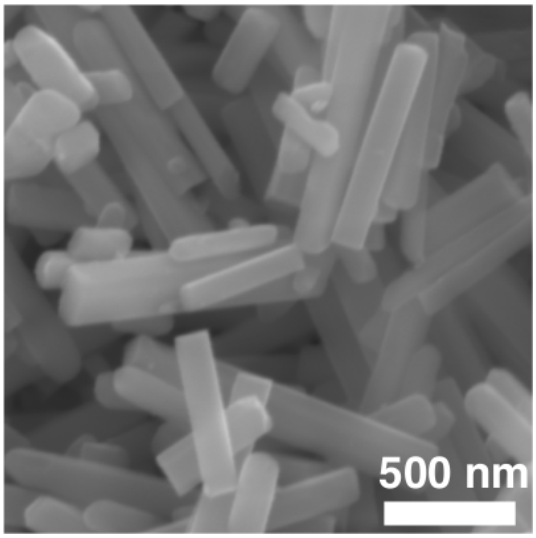


Figure 7.2: Higher magnification image of pristine FD material.

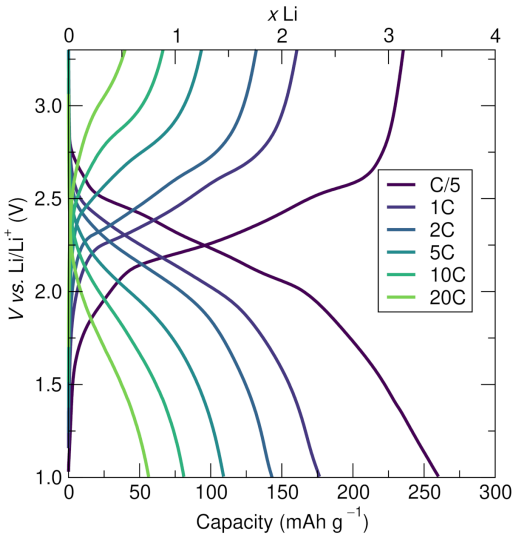


Figure 7.3: Galvanostatic cycling of Conv. $(W_{0.2}V_{0.8})_3O_7$ at rates from C/5 to 20C.

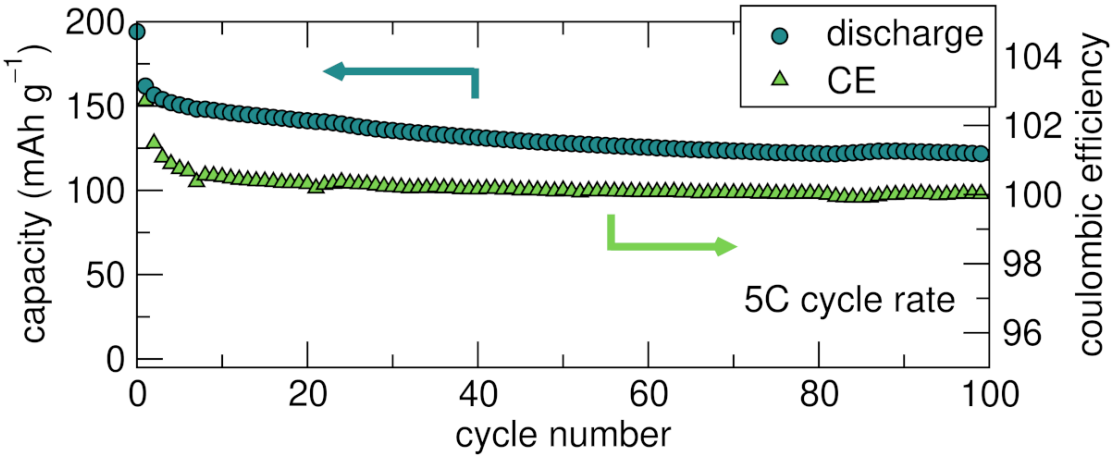


Figure 7.4: Extended cycling of Conv. $(W_{0.2}V_{0.8})_3O_7$ at a 5C rate.

Table 7.3: Summary of analysis of the exponent $b$ from Figure 6 that shows the corresponding equations and coefficient of determination that fit the relationship between current and sweep rate for $(W_{0.2}V_{0.8})_3O_7$.

| | **avg.** | $b$ | $\mathbf{R}^2$ |
|---|---|---|---|
| red | 2.01 V | 0.49 | 0.9975 |
| | 2.41 V | 0.67 | 0.9963 |
| ox | 2.46 V | 0.50 | 0.9968 |
| | 2.69 V | 0.61 | 0.9975 |

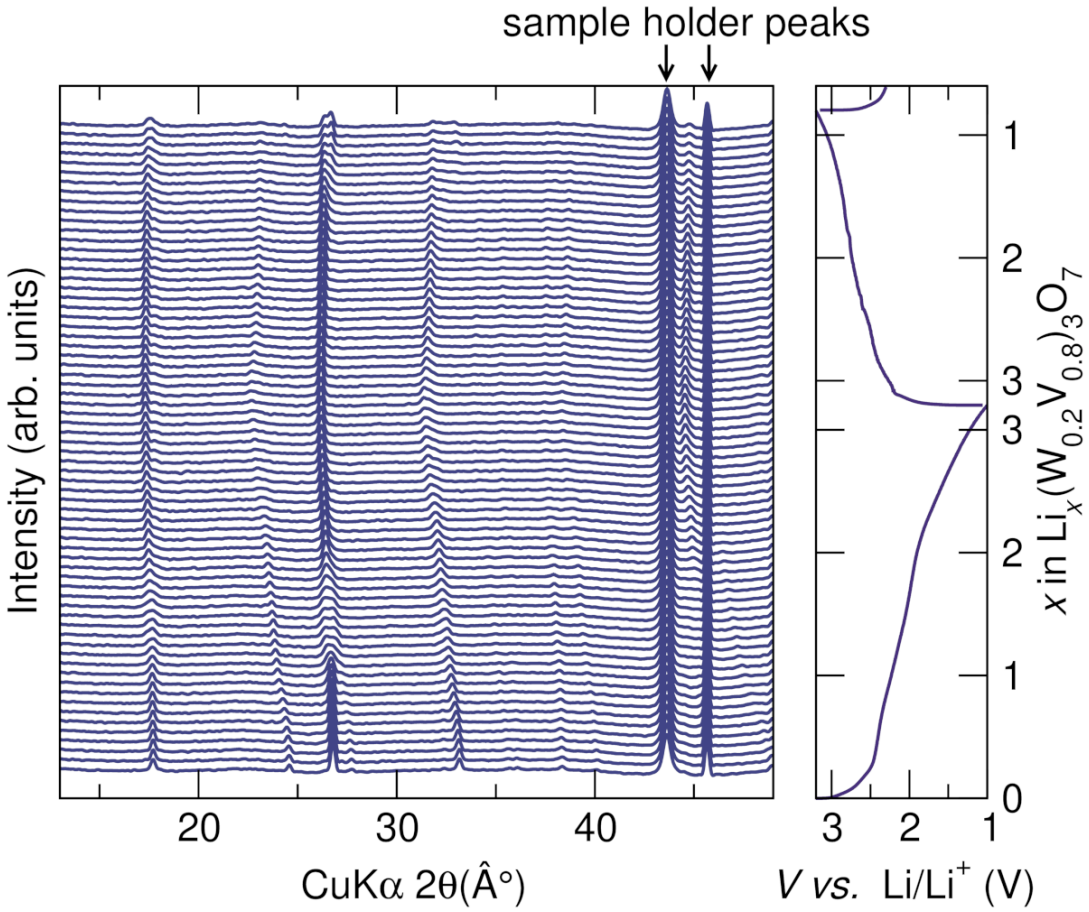


Figure 7.5: (left) Full *operando* diffraction range of FD $(W_{0.2}V_{0.8})_3O_7$ during the first galvanostatic cycle at a rate of C/10. Electrochemistry is shown on the right panel.

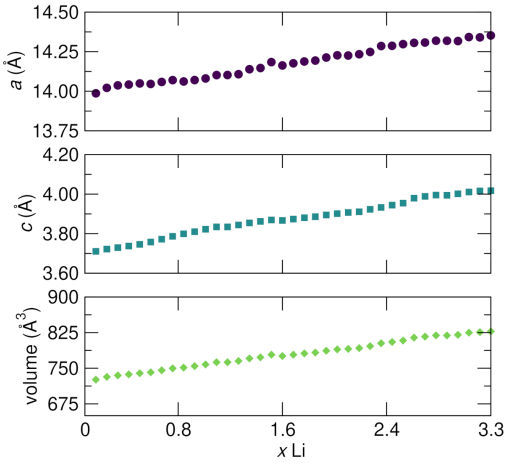


Figure 7.6: Variation of cell parameters and cell volume with lithiation of the principle 3×3 Wadley-Roth phase of FD $(W_{0.2}V_{0.8})_3O_7$ as a function of lithiation under conditions of *operando* diffraction. A moderate and nearly-linear increase in lattice parameters and cell volume is noted with increasing lithiation.

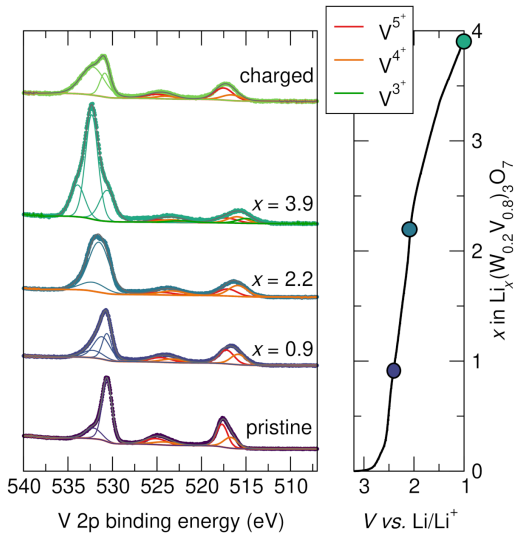


Figure 7.7: (left) Expanded view showing the full spectral regions for V $2p$ and O $1s$ from XPS. To improve accuracy, all states were fit together. The states of charge are mapped on the electrochemistry shown in the right panel.

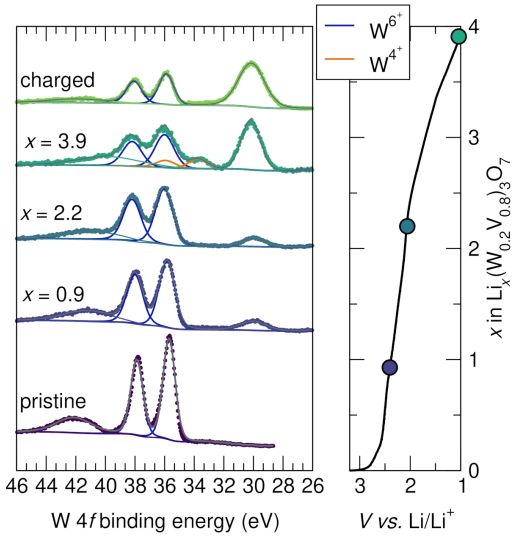


Figure 7.8: (left) Expanded view showing the full spectral regions for W 4$f$ and F 1$s$ from XPS. To improve accuracy, all states were fit together. The states of charge are mapped on the electrochemistry shown in the right panel.

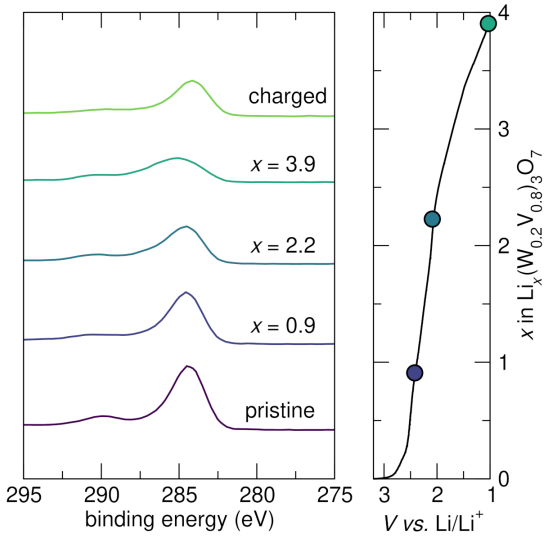


Figure 7.9: (left) XPS survey scans for each state of charge showing that the C 1$s$ region lines up using the calibration method described in the main text. The states of charge are mapped on the electrochemistry shown in the right panel.

Table 7.4: Quantitative analysis of the evolution of oxidation states from fitting the high resolution spectra found in Figure 8 and Figure 9.

| $x$ in $Li_x(W_{0.2}V_{0.6})_3O_7$ | % $V^{5+}$ | % $V^{4+}$ | % $V^{3+}$ | % $W^{6+}$ | % $W^{4+}$ |
|---|---|---|---|---|---|
| 0 | 63 | 37 | 0 | 100 | 0 |
| 0.91 | 57 | 43 | 0 | 100 | 0 |
| 2.15 | 39 | 61 | 0 | 100 | 0 |
| 3.94 | 35 | 38 | 27 | 77 | 23 |
| charged | 67 | 33 | 0 | 100 | 0 |

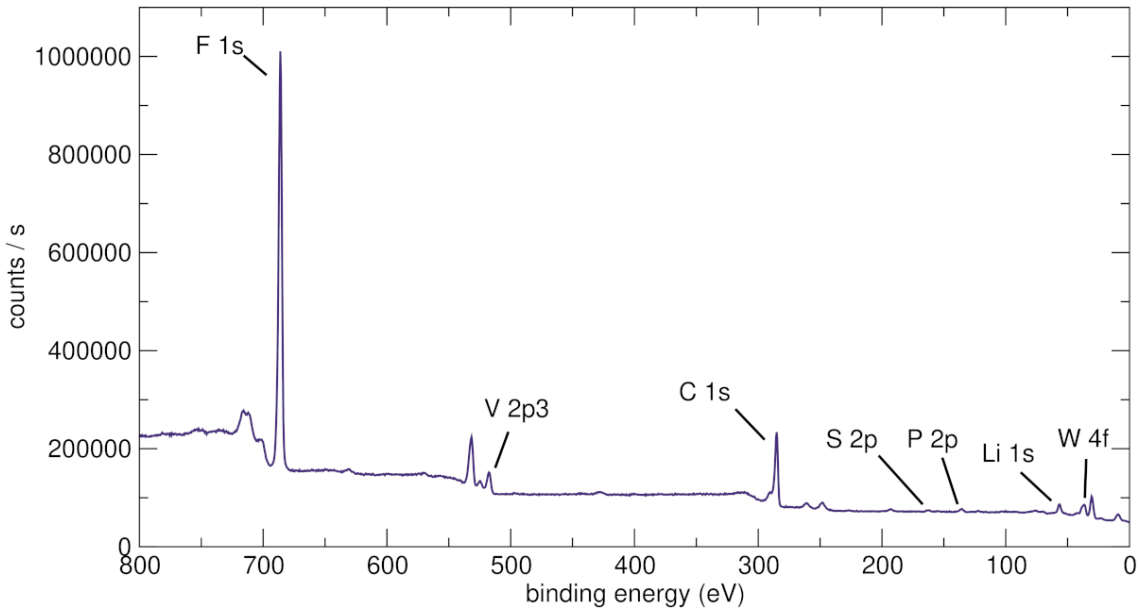


Figure 7.10: XPS survey scan of a fully discharged electrode shows signals from F $1s$, V $2p3$, C $1s$, S $2p$, P $2p$, Li $1s$, and W $4f$.

Table 7.5: Quantitative analysis of the elemental composition in an electrode from fitting the survey scan in Figure S7.10.

| Peak | Peak binding energy (eV) | Atomic % |
|---|---|---|
| F 1s | 685.97 | 39.64 |
| V 2p3 | 517.21 | 1.06 |
| C 1s | 285.04 | 23.33 |
| S 2p | 162.00 | 0.27 |
| P 2P | 135.55 | 0.77 |
| Li 1s | 56.51 | 34.66 |
| W 4f | 36.55 | 0.27 |

| | Expected | Measured |
|---|---|---|
| V:W ratio | 4.0 | 3.93 |

Table 7.6: Quantitative analysis of the elemental composition from energy-dispersive X-ray spectroscopy in the pristine Conv. material.

| Element | Expected atomic fraction | Measured atomic fraction |
|---|---|---|
| W | 0.20 | 0.21 |
| V | 0.80 | 0.79 |

## 7.2 Supporting Information for Chapter 4

Table 7.7: Summary of crystallographic refinement parameters from Figure 3 in the main text for $LiScMo_3O_8$ in space group $P3m1$ using synchrotron powder X-ray diffraction. The lattice parameters are $a = 5.7247$ Å and $c = 4.9436$ Å. $B_{\mathrm{iso}}$ is the thermal displacement parameter. The $R$-factors $R_{\mathrm{wp}}$ and $R_{\mathrm{exp}}$ are 14.12 and 7.05 respectively.

| | Site | $x$ | $y$ | $z$ | $B_{iso}$ (Å$^2$) |
|---|---|---|---|---|---|
| Li1 | 1*c* | 0.6667 | 0.3333 | 0.6140 | 1.0 (fixed) |
| Sc1 | 1*b* | 0.3333 | 0.6667 | 0.71(8) | 0.6(3) |
| Mo1 | 3*d* | 0.8534 | 0.1466 | 0.24(1) | 0.49(3) |
| O1 | 1*a* | 0 | 0 | 0.50(6) | 0.5(7) |
| O2 | 1*c* | 0.6667 | 0.3333 | 0.01(5) | 0.5(7) |
| O3 | 3*d* | 0.4980 | 0.5020 | 0.46(0) | 0.5(7) |
| O4 | 3*d* | 0.1667 | 0.8333 | 0.00(3) | 0.5(7) |

Note: $B_{iso}$ was fixed for Li at 1.0 Å$^2$. $B_{iso}$ values for all of the O atoms were contrained to refine together.

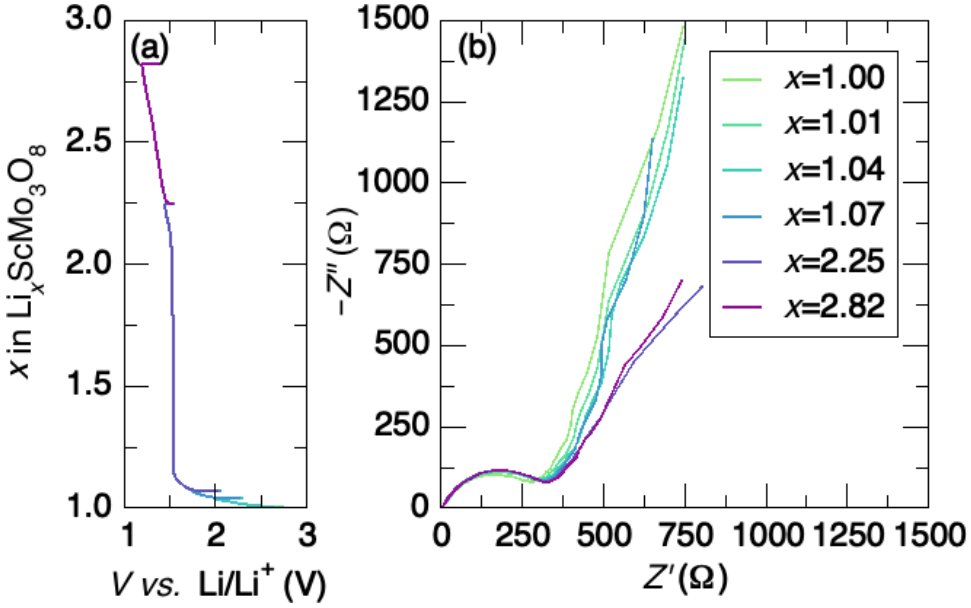


Figure 7.11: Electrochemical impedance spectra of slurry electrodes as a function of $Li^+$ content in $LiScMo_3O_8$. The charge transfer resistance remains relatively constant as a function of lithiation

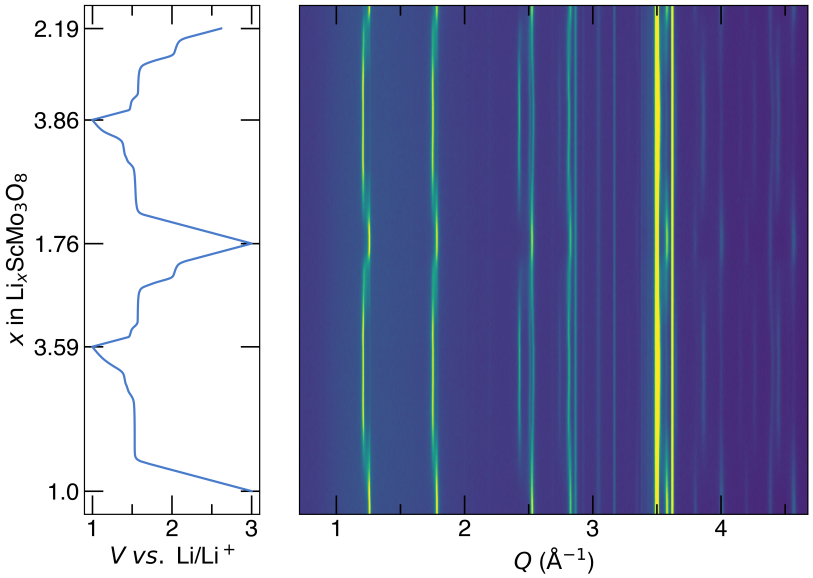


Figure 7.12: *Operando* X-ray diffraction of $LiScMo_3O_8$ during the first two galvanostatic discharge/charge cycles at a C/15 cycling rate. The electrochemistry is shown in the left-most panel, inserting over two additional $Li^+$ to $Li_3ScMo_3O_8$. The entire $Q$ range is shown on the left as a heat map.

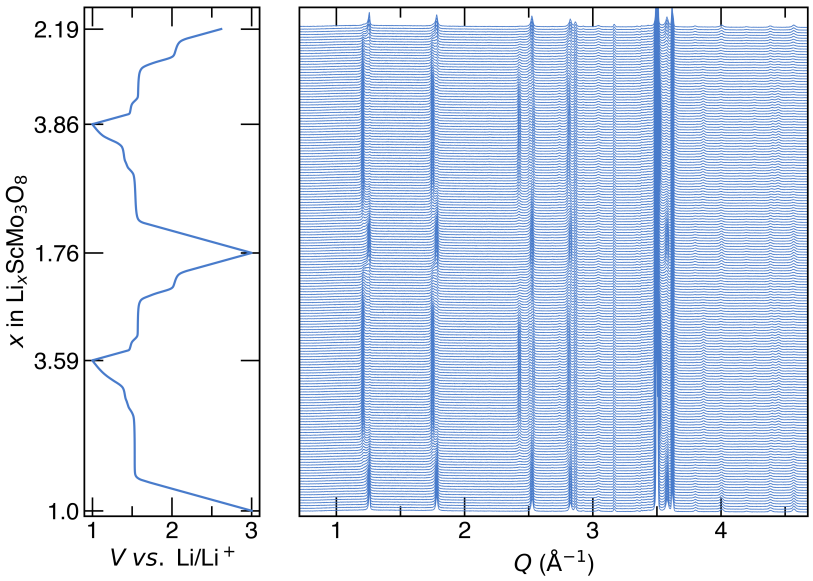


Figure 7.13: *Operando* X-ray diffraction of $LiScMo_3O_8$ during the first two galvanostatic discharge/charge cycles at a C/15 cycling rate. The electrochemistry is shown in the left-most panel, inserting over two additional $Li^+$ to $Li_3ScMo_3O_8$. The entire $Q$ range is shown on the left.

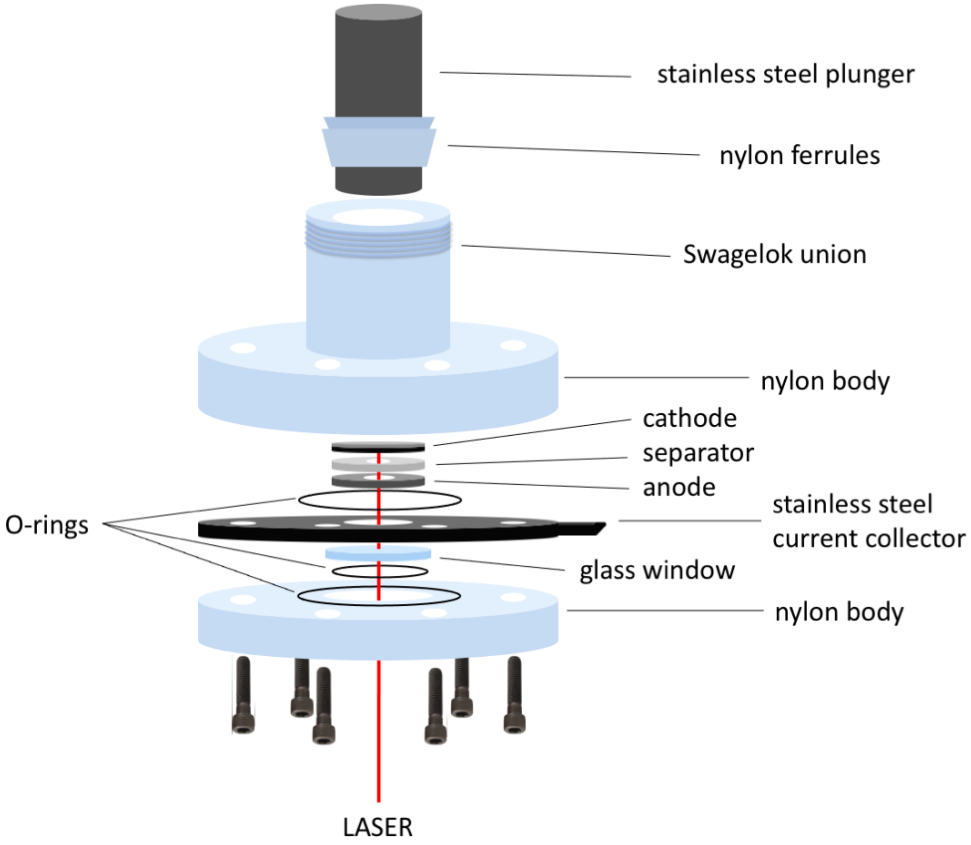


Figure 7.14: Schematic of custom spectroelectrochemical cell for *operando* Raman spectroscopy measurements in a front-side scattering arrangement with respect to the cathode.

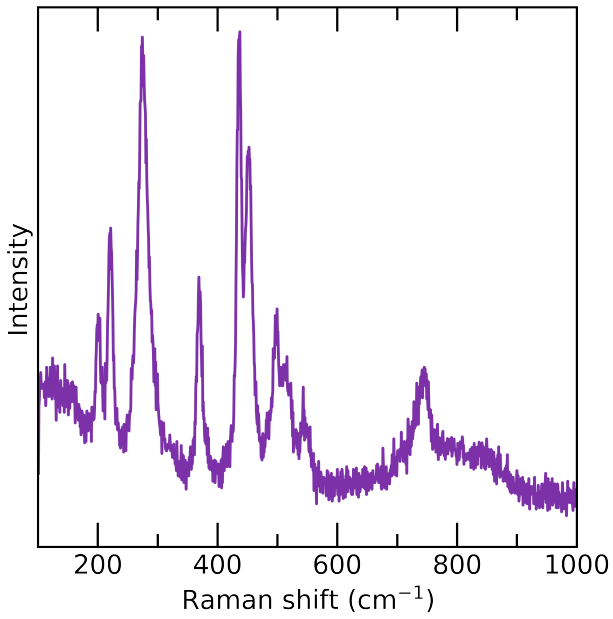


Figure 7.15: *Ex situ* Raman spectroscopy spectrum of pristine $LiScMo_3O_8$.

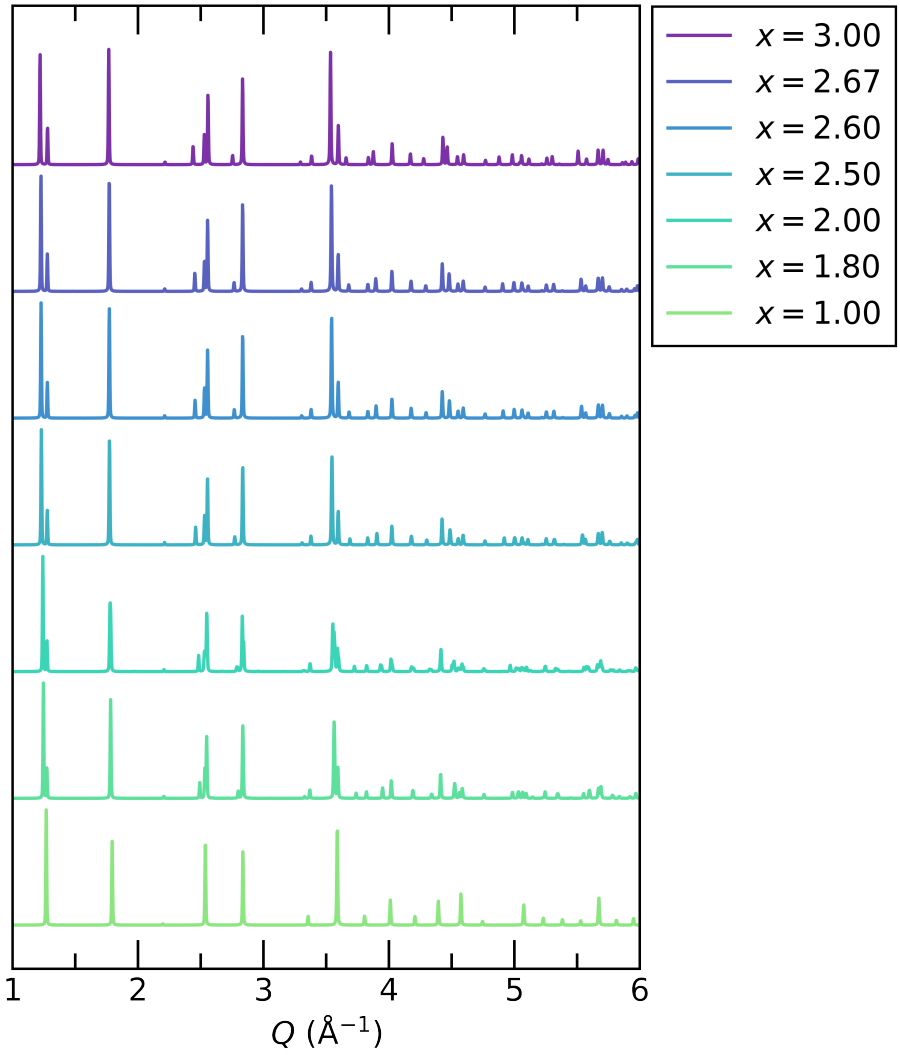


Figure 7.16: Simulated diffraction data for ground state structures of $Li_xScMo_3O_8$ at $x = 1.00$, 1.80, 2.00, 2.50, 2.60, 2.67, and 2.85.

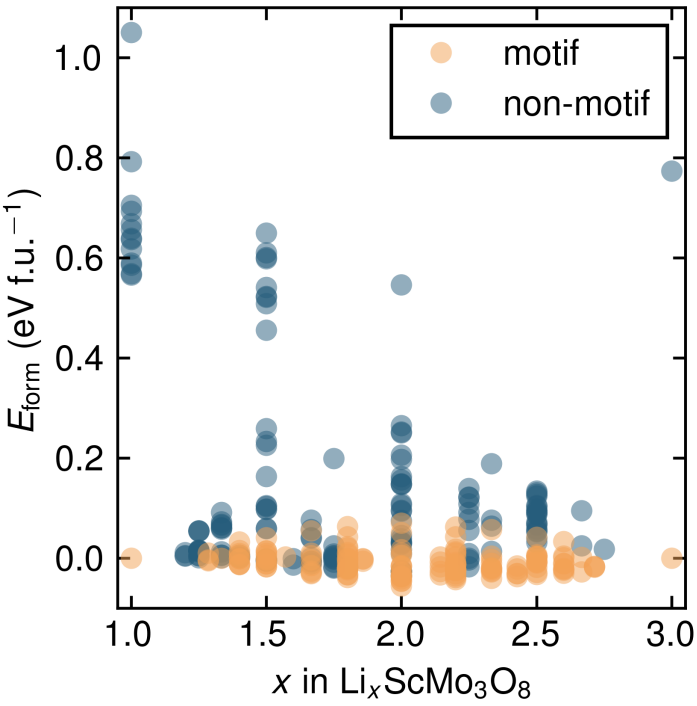


Figure 7.17: Calculated formation energies of distinct $Li^+$-vacancy orderings in $Li_xScMo_3O_8$, labeled by whether the configuration follows the identified favorable $Li^+$ ordering motif.

## 7.3 Supporting Information for Chapter 5

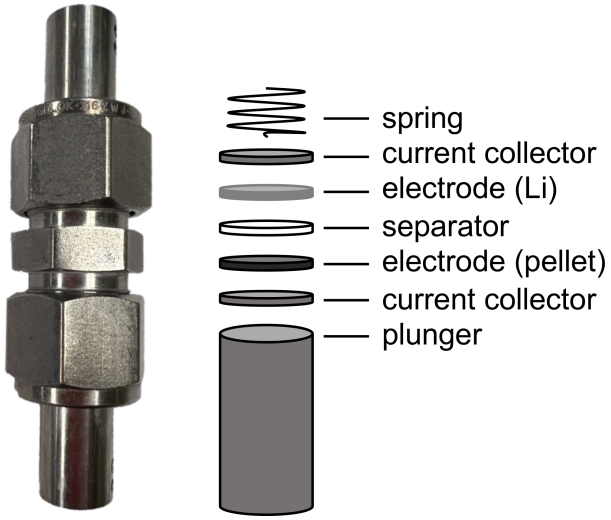


Figure 7.18: Diagram showing a picture of an experimental swagelok cell on the right and a corresponding schematic of the internal components on the left. For electrochemical lithiation, one electrode of the cell is Li metal and the other electrode is a pressed pellet of $LiScMo_3O_8$. The electrodes are separated with a glass fiber separator saturated in electrolyte and the entire stack is kept under light pressure with a metal spring The current collectors are made of stainless steel.

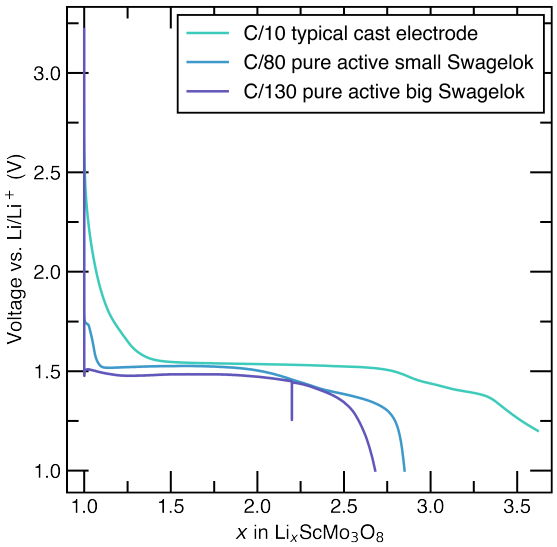


Figure 7.19: Overlay of electrochemical discharge curves comparing pressed pellets of pure active material cycled in both small and large Swagelok cells, compared to a typical composite cast electrode. There is slight overpotential introduced by omitting binder and conductive carbon. Additionally, the structure of the discharge curves smooth with increasing sample size.

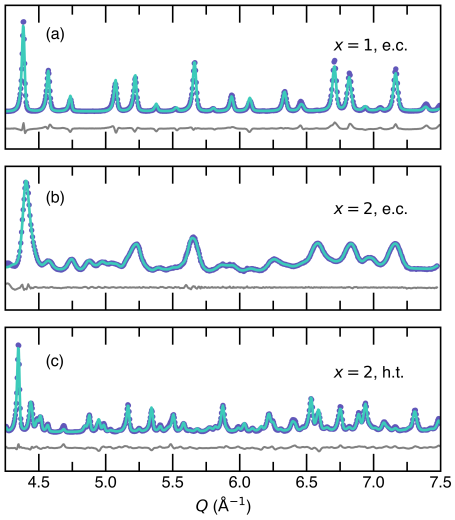


Figure 7.20: Neutron powder Bragg diffraction data and refinements for (a) $LiScMo_3O_8$ (Rietveld refinement on NOMAD data to $P3m1$ space group), (b) $Li_2ScMo_3O_8$ (e.c.) (Pawley refinement on WAND$^2$ data to $C2$ space group), and (c) $Li_2ScMo_3O_8$ (h.t.) (Rietveld refinement on NOMAD data to $P6_3mc$ space group) shows single phases for all materials. Refinement statistics can be found in the following tables.

The starting material $LiScMo_3O_8$ was characterized with neutron powder diffraction at the NOMAD beamline located at Oak Ridge National Laboratory. Rietveld refinement of $LiScMo_3O_8$ in Figure 7.20(a) shows good agreement with the expected structure. Electrochemically prepared $Li_2ScMo_3O_8$ (e.c.) was characterized with neutron powder diffraction at the WAND$^2$ HB-2C beamline at Oak Ridge National Laboratory and shows a single phase from a Pawley refinement to an indexed space group that is closely related to the parent structure. Previous experiments show that the $Li_2ScMo_3O_8$ (e.c.) material stays highly crystalline and the broad peaks shown here are due to the momentum resolution on the WAND$^2$ HB-2C beamline. High-temperature $Li_2ScMo_3O_8$ (h.t.) was also characterized with neutron powder diffraction at the NOMAD beamline and shows good agreement with the accepted structure. Atomic positions can be found in the included CIF files for these refinements.

Table 7.8: Summary of refinement parameters from Figure 7.20 (a) in the Supporting Information from a Rietveld refinement on NOMAD data bank 5 for $LiScMo_3O_8$.

$LiScMo_3O_8$

| parameter | value |
|---|---|
| lattice constant | $a$ = 5.72358(9) Å |
| | $c$ = 4.94235(9) Å |
| space group | $P3m1$ |
| | |
| $R_{wp}$ | 8.75 |
| $R_{exp}$ | 0.72 |
| GOF = $R_{wp}/R_{exp}$ | 12.15 |

Table 7.9: Summary of refinement parameters from Figure 7.20 (b) in the Supporting Information from a Pawley refinement on $WAND^2$ data for $Li_2ScMo_3O_8$ (e.c.).

$Li_2ScMo_3O_8$ (e.c.)

| parameter | value |
|---|---|
| lattice constant | $a$ = 10.37199(8) Å |
| | $b$ = 9.90785(8) Å |
| | $c$ = 3.04370(8) Å |
| space group | $C2$ |
| | |
| $R_{wp}$ | 1.81 |
| $R_{exp}$ | 20.01 |
| GOF = $R_{wp}/R_{exp}$ | 0.09 |

Table 7.10: Summary of refinement parameters from Figure 7.20 (c) in the Supporting Information from a Rietveld refinement on NOMAD data bank 5 for $Li_2ScMo_3O_8$ (h.t.).

$Li_2ScMo_3O_8$ (h.t.)

| parameter | value |
|---|---|
| lattice constant | $a$ = 5.77107(7) Å |
| | $c$ = 10.29286(3) Å |
| space group | $P6_3mc$ |
| | |
| $R_{wp}$ | 9.51 |
| $R_{exp}$ | 0.60 |
| GOF = $R_{wp}/R_{exp}$ | 15.85 |

Table 7.11: Summary of refinement parameters from Figure 5 (a) in the main text from a Rietveld refinement on $Li_2ScMo_3O_8$ (e.c.). The $R_{wp}$ is 12.53, the $R_{exp}$ is 8.86, and the GOF is 2.14. The space group is *P1*.

| | |
|---|---|
| *a* | 5.7224(5) |
| *b* | 7.5748(8) |
| *c* | 7.576(1) |
| $\alpha$ | 81.733(8)° |
| $\beta$ | 67.77(1)° |
| $\gamma$ | 67.795(7)° |

| site | x | y | z | occ |
|---|---|---|---|---|
| Li1 | 0.998973 | 0.181235 | 0.819429 | 1 |
| Li2 | 0.833318 | 0.819686 | 0.514381 | 1 |
| Li3 | 0.319834 | 0.570296 | 0.266863 | 1 |
| Li4 | 0.842511 | 0.571096 | 0.266899 | 1 |
| Mo1 | 0.82(1) | 0.30(1) | 0.51(1) | 1 |
| Mo2 | 0.82(1) | 0.81(1) | 0.00(1) | 1 |
| Mo3 | 0.37(1) | 0.31(1) | 0.50(1) | 1 |
| Mo4 | 0.82(1) | 0.58(1) | 0.80(1) | 1 |
| Mo5 | 0.82(1) | 0.09(1) | 0.28(1) | 1 |
| Mo6 | 0.37(1) | 0.82(1) | 0.01(1) | 1 |
| O1 | 0.161375 | 0.368118 | 0.792542 | 1 |
| O2 | 0.160129 | 0.128359 | 0.551021 | 1 |
| O3 | 0.159852 | 0.866374 | 0.295562 | 1 |
| O4 | 0.661441 | 0.599414 | 0.077696 | 1 |
| O5 | 0.670963 | 0.090764 | 0.567302 | 1 |
| O6 | 0.502138 | 0.027209 | 0.968808 | 1 |
| O7 | 0.503866 | 0.528719 | 0.463267 | 1 |
| O8 | 0.995221 | 0.287411 | 0.221486 | 1 |
| O9 | 0.995775 | 0.777433 | 0.716441 | 1 |
| O10 | 0.677749 | 0.368280 | 0.792407 | 1 |
| O11 | 0.678310 | 0.866258 | 0.295568 | 1 |
| O12 | 0.161290 | 0.623571 | 0.053998 | 1 |
| O13 | 0.510649 | 0.777398 | 0.716385 | 1 |
| O14 | 0.495931 | 0.287302 | 0.221520 | 1 |
| O15 | 0.001795 | 0.000515 | 0.996074 | 1 |
| O16 | 0.000104 | 0.507315 | 0.492484 | 1 |
| Sc1 | 0.32(1) | 0.83(2) | 0.53(1) | 1 |
| Sc2 | 0.34(1) | 0.33(2) | 0.97(1) | 1 |

Table 7.12: Summary of refinement parameters from Figure 5 (b) in the main text from a Rietveld refinement on $Li_3ScMo_3O_8$ (e.c.). The $R_{wp}$ is 8.70, the $R_{exp}$ is 5.98, and the GOF is 1.45. The space group is *P1*.

| | |
|---|---|
| *a* | 5.1514(1) |
| *b* | 5.70220(6) |
| *c* | 5.70220(6) |
| | |
| $\alpha$ | 120° |
| $\beta$ | 90° |
| $\gamma$ | 90° |

| site | x | y | z | occ |
|---|---|---|---|---|
| Li1 | 0.305400 | 0.159078 | 0.318156 | 1 |
| Li2 | 0.305400 | 0.681844 | 0.840922 | 1 |
| Li3 | 0.305400 | 0.159078 | 0.840922 | 1 |
| Mo1 | 0.837(1) | 0.156(1) | 0.335(1) | 1 |
| Mo2 | 0.837(1) | 0.591(2) | 0.793(1) | 1 |
| Mo3 | 0.837(1) | 0.155(1) | 0.792(1) | 1 |
| O1 | 0.565219 | 0.840652 | 0.681304 | 1 |
| O2 | 0.565219 | 0.318696 | 0.159348 | 1 |
| O3 | 0.080746 | 0.012449 | 0.506225 | 1 |
| O4 | 0.080746 | 0.493775 | 0.987551 | 1 |
| O5 | 0.525212 | 0.333333 | 0.666667 | 1 |
| O6 | 0.565219 | 0.840652 | 0.159348 | 1 |
| O7 | 0.080746 | 0.493775 | 0.506225 | 1 |
| O8 | 0.016381 | 0.000000 | 0.000000 | 1 |
| Sc1 | 0.257(3) | 0.666667 | 0.333333 | 1 |

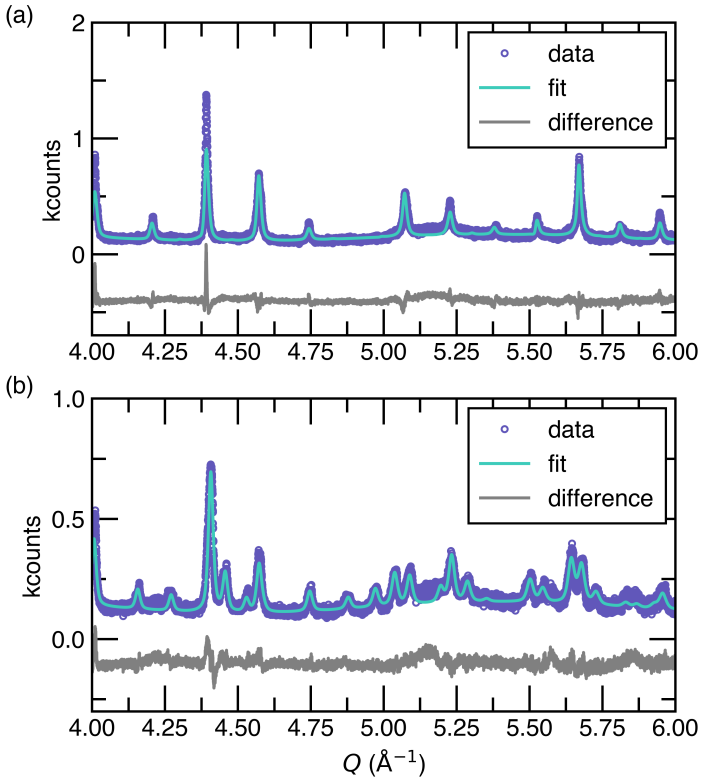


Figure 7.21: Rietveld refinements of (a) $Li_2ScMo_3O_8$ (e.c.) and (b) $Li_3ScMo_3O_8$ (e.c.) of *operando* synchrotron powder diffraction data collected at 11-BM at APS. These diffraction patterns were extracted from the *operando* AMPIX experiment and fit to the calculated ground state structures. The backgrounds were fit and only the lattice parameters and transition metal sites were allowed to refine. This figure shows the high $Q$ region only.

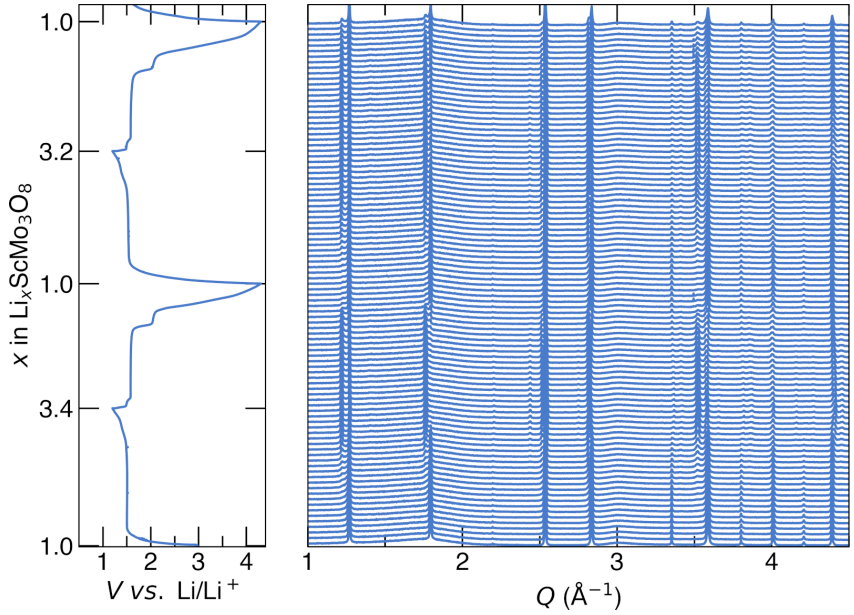


Figure 7.22: *Operando* synchrotron X-ray diffraction of $LiScMo_3O_8$ during the first two galvanostatic discharge/charge cycles at a C/15 cycling rate. The electrochemistry is shown in the left panel.

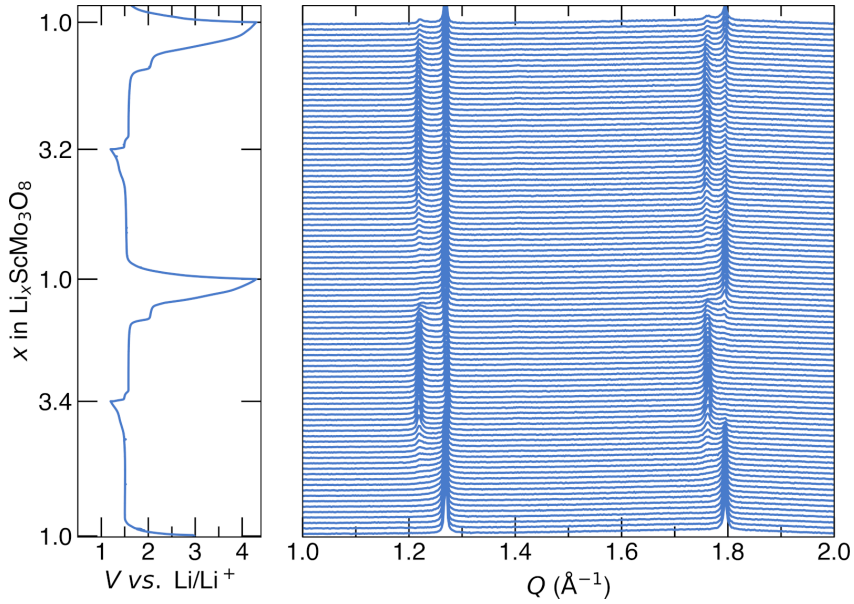


Figure 7.23: *Operando* synchrotron X-ray diffraction of $LiScMo_3O_8$ during the first two galvanostatic discharge/charge cycles at a C/15 cycling rate. The electrochemistry is shown in the left panel. The right panel shows the diffraction data at low $Q$.

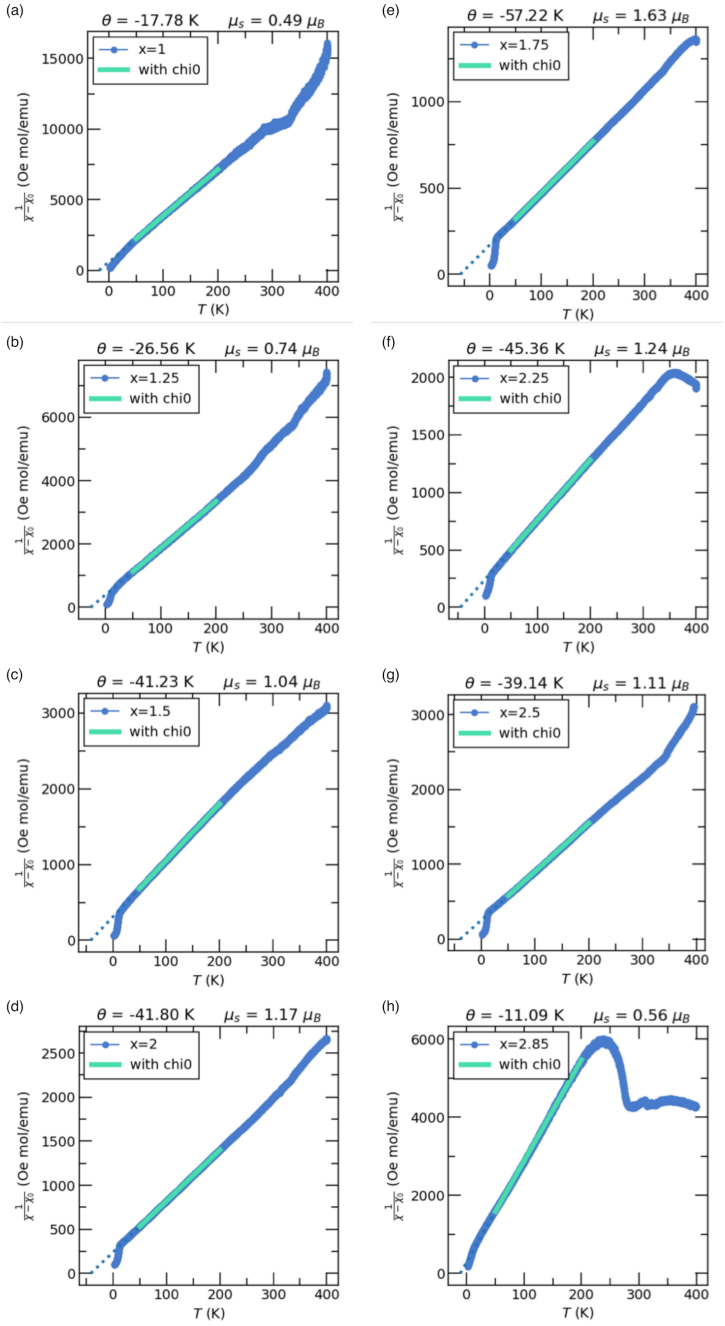


Figure 7.24: Curie-Weiss fits for all of the electrochemically prepared samples from 50 K to 200 K.

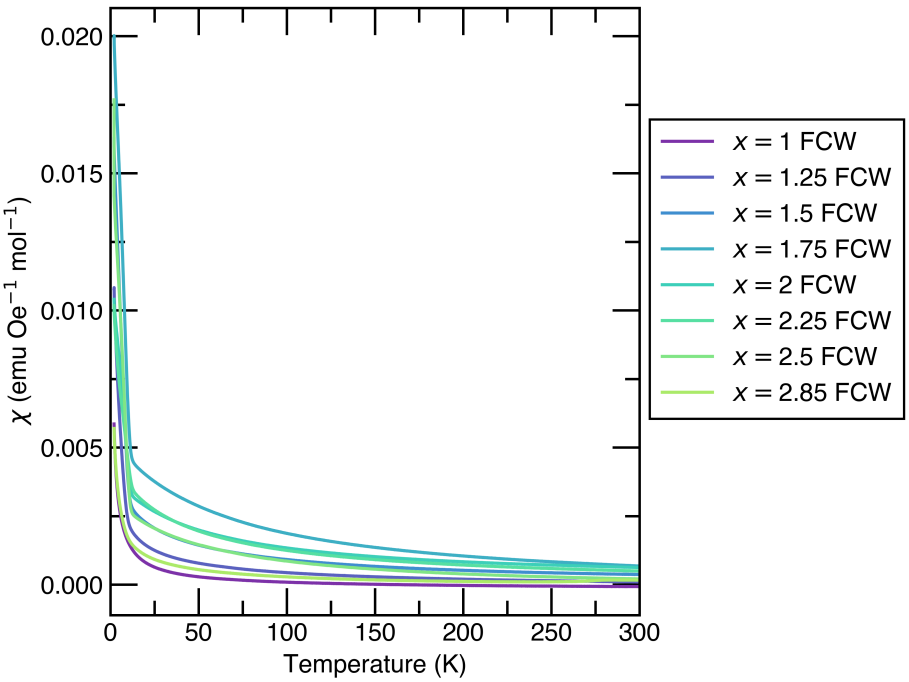


Figure 7.25: Overlay of the field-cooled warming susceptibility data as a function of temperature for all of the samples.

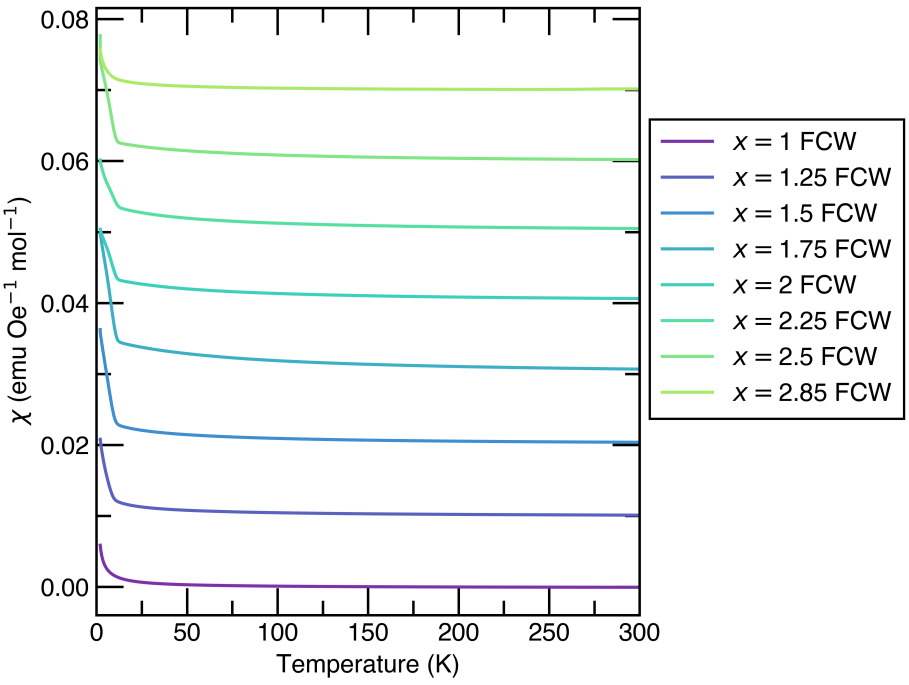


Figure 7.26: Offset of the field-cooled warming susceptibility data as a function of temperature for all of the samples.

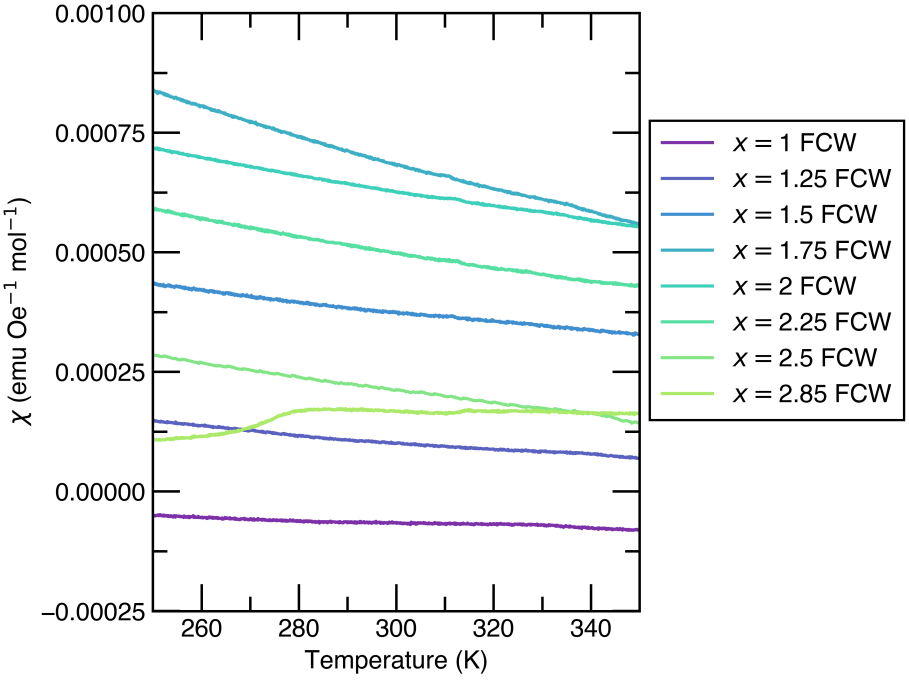


Figure 7.27: Overlay and zoom of the high-temperature regime of the field-cooled warming susceptibility data as a function of temperature for all of the samples.

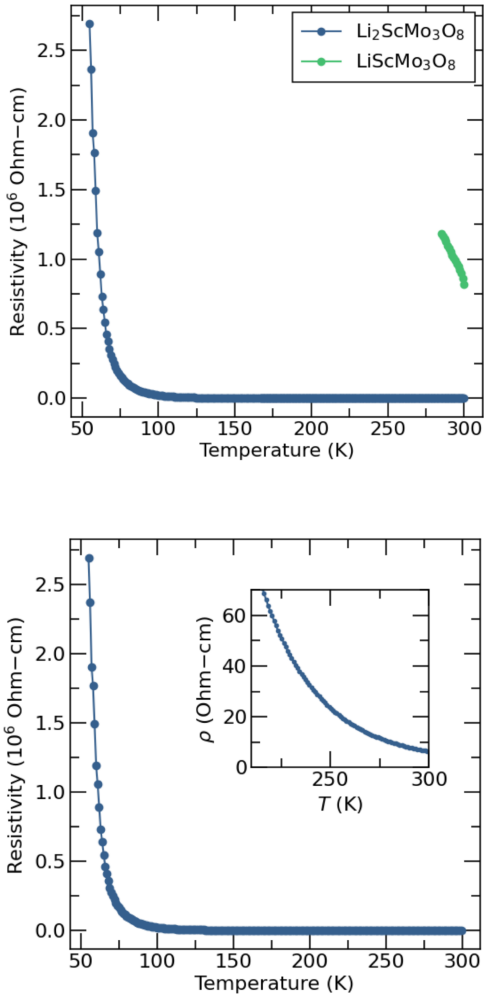


Figure 7.28: (top) Resistivity data for $Li_2ScMo_3O_8$ (h.t.) and $LiScMo_3O_8$ taken using a 4-point probe measurement on a Quantum Design PPMS. $Li_2ScMo_3O_8$ (h.t.) displays nearly 6 orders of magnitude lower resistivty than $LiScMo_3O_8$. (bottom) Resistivity data for $Li_2ScMo_3O_8$ (h.t.) with an inset highlighting the significantly lower resistivity value close to room temperature.

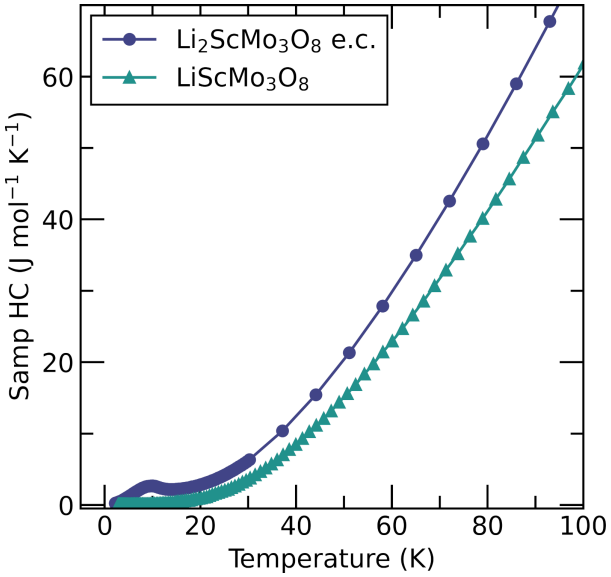


Figure 7.29: Heat capacity for $Li_2ScMo_3O_8$ (e.c.) and $LiScMo_3O_8$ from 3 K to 100 K.

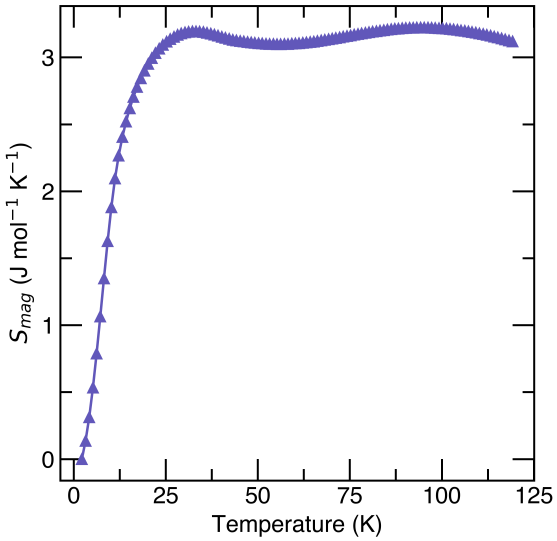


Figure 7.30: Magnetic entropy as a function of temperature for $Li_2ScMo_3O_8$ (e.c.).

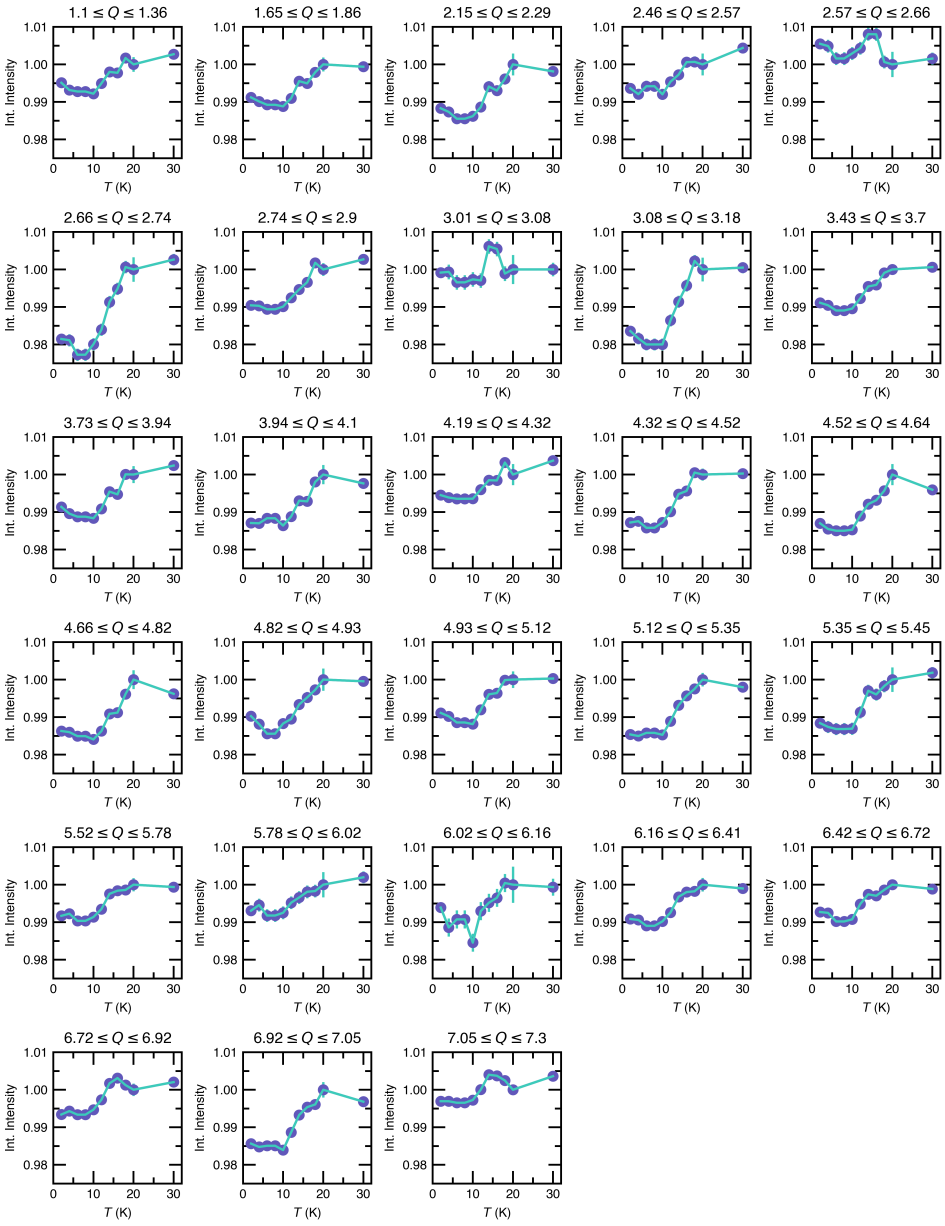


Figure 7.31: Integrated intensity for every diffraction peak as a function of temperature for $Li_2ScMo_3O_8$ (e.c.) from neutron diffraction data taken on WAND$^2$ beamline at Oak Ridge National Laboratory.

## 7.4 Supporting Information for Chapter 3

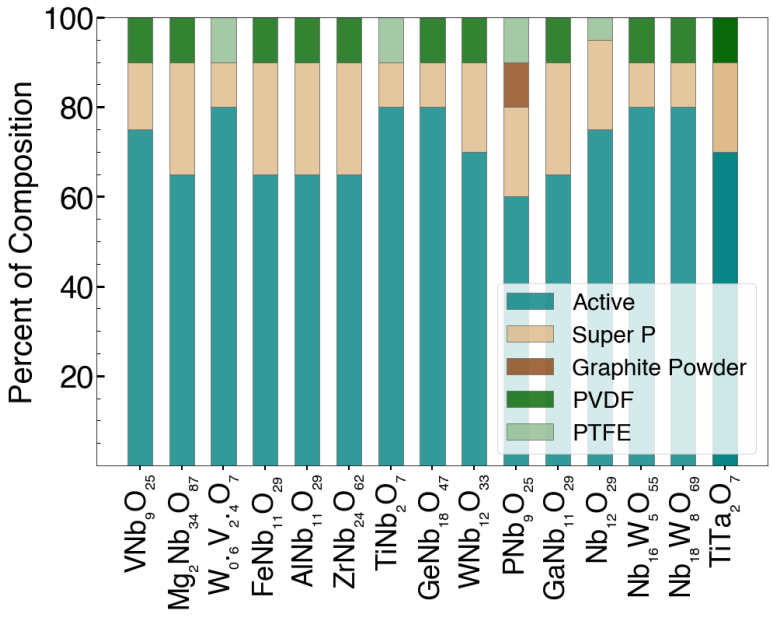


Figure 7.32: Electrode composition breakdowns for the materials analyzed in the text.

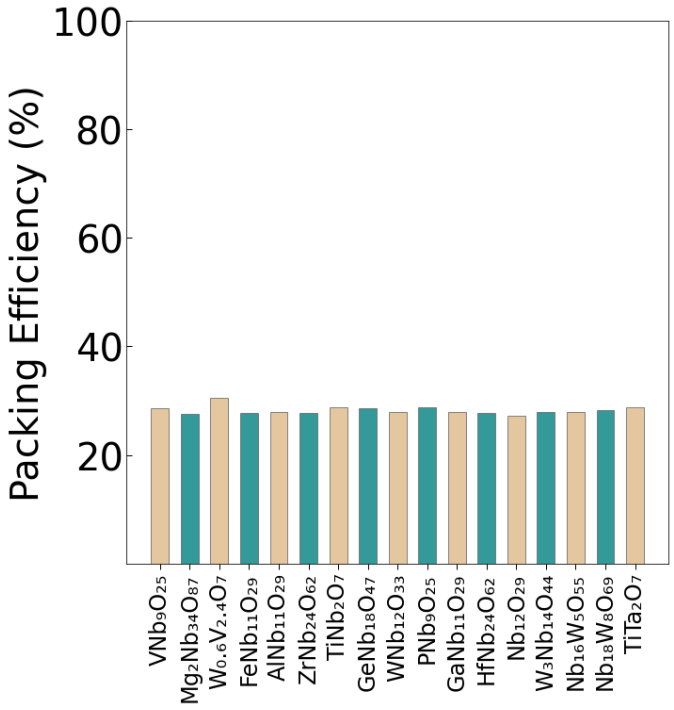


Figure 7.33: Packing efficiencies for the materials analyzed in the text.

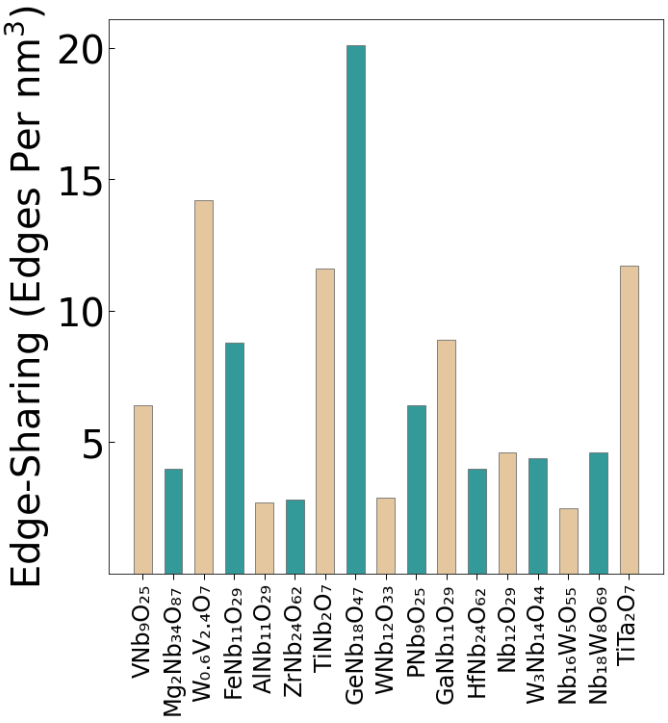


Figure 7.34: Edge-sharing densities for the materials analyzed in the text.

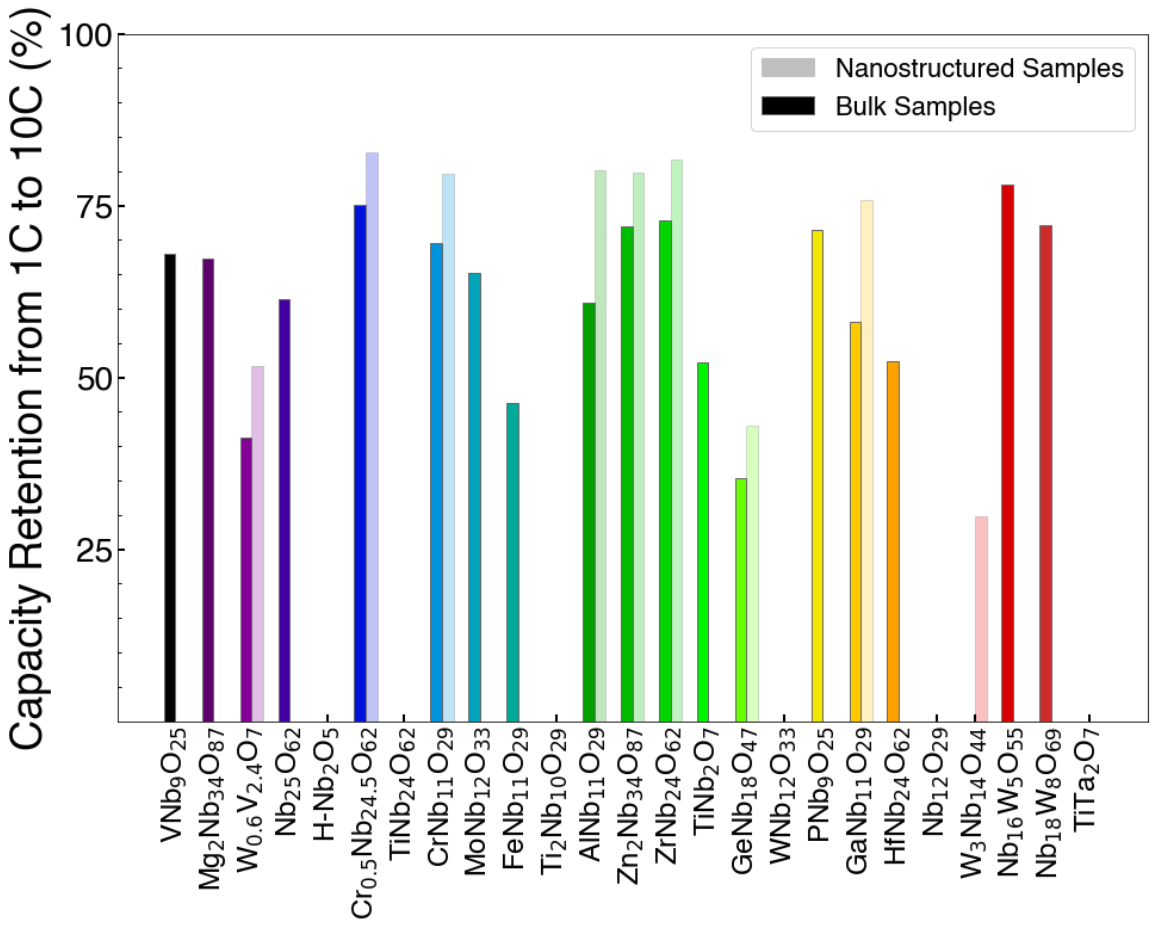


Figure 7.35: Capacity retention for the materials analyzed in the text. Nanostructured capacity retention is compared to bulk capacity retention for select materials.

# Bibliography


[1] M. S. Whittingham. The role of ternary phases in cathode reactions. *J. Electrochem. Soc.* **123** (1976) 315.

[2] K. Mizushima, P. C. Jones, P. J. Wiseman, and J. B. Goodenough. $Li_xCoO_2$ ($0\,x \leq 1$): A new cathode material for batteries of high energy density. *Solid State Ion.* **3** (1981) 171–174.

[3] B. Dunn, H. Kamath, and J.-M. Tarascon. Electrical Energy Storage for the Grid: A Battery of Choices. *Science* **334** (2011) 928–935.

[4] M. R. Lukatskaya, B. Dunn, and Y. Gogotsi. Multidimensional Materials and Device Architectures for Future Hybrid Energy Storage. *Nat. Commun.* **7** (2016) 12647. doi:10.1038/ncomms12647

[5] J. B. Goodenough and K. S. Park. The Li-Ion Rechargeable Battery: A Perspective. *J. Am. Chem. Soc.* **135** (2013) 1167–1176. doi:10.1021/ja3091438

[6] Y. Wang and G. Cao. Developments in Nanostructured Cathode Materials for High-Performance Lithium-Ion Batteries. *Adv. Mater.* **20** (2008) 2251–2269.

[7] R. Mukherjee, R. Krishnan, T.-M. Lu, and N. Koratkar. Nanostructured Electrodes for High-Power Lithium Ion Batteries. *Nano Energy* **1** (2012) 518–533.

[8] D.-H. Kim and J. Kim. Synthesis of $LiFePO_4$ Nanoparticles in Polyol Medium and Their Electrochemical Properties. *Electrochem. Solid-State Lett.* **9** (2006) A439–A442.

[9] Z. Yang, D. Choi, S. Kerisit, K. M. Rosso, D. Wang, J. Zhang, G. Graff, and J. Liu. Nanostructures and Lithium Electrochemical Reactivity of Lithium Titanites and Titanium Oxides: A Review. *J. Power Sources* **192** (2009) 588–598. doi:10.1016/j.jpowsour.2009.02.038

[10] M. R. Palacín, P. Simon, and J. M. Tarascon. Nanomaterials for Electrochemical Energy Storage: The Good and the Bad. *Acta Chim. Slov.* **63** (2016) 417–423.

[11] J. B. Cook, T. C. Lin, H.-S. Kim, A. Siordia, B. S. Dunn, and S. H. Tolbert. Suppression of Electrochemically Driven Phase Transitions in Nanostructured $MoS_2$ Pseudocapacitors Probed Using Operando X-ray Diffraction. *ACS Nano* **13** (2019) 1223–1231.

[12] M. M. Doeff, J. D. Wilcox, R. Kostecki, and G. Lau. Optimization of Carbon Coatings on $LiFePO_4$. *J. Power Sources* **163** (2006) 180–184.

[13] H. C. Shin, W. I. Cho, and H. Jang. Electrochemical Properties of Carbon-Coated $LiFePO_4$ Cathode Using Graphite, Carbon Black, and acetylene black. *Electrochim. Acta* **52** (2006) 1472–1476.

[14] J. Jiang and J. R. Dahn. Dependence of the Heat of Reaction of $Li_{0.81}C_6$ (0.1 V), $Li_7Ti_5O_{12}$ (1.55 V), and $Li_{0.5}VO_2$ (2.45 V) Reacting with Nonaqueous Solvents or Electrolytes on the Average Potential of the Electrode Material. *J. Electrochem. Soc.* **153** (2006) A310–A315. doi:10.1149/1.2146914

[15] L. E. Downie, L. J. Krause, J. C. Burns, L. D. Jensen, V. L. Chevrier, and J. R. Dahn. In Situ Detection of Lithium Plating on Graphite Electrodes by Electrochemical Calorimetry. *J. Electrochem. Soc.* **160** (2013) A588–A594. doi:10.1149/2.049304jes

[16] J. C. Burns, D. A. Stevens, and J. R. Dahn. In-Situ Detection of Lithium Plating Using High Precision Coulometry. *J. Electrochem. Soc.* **162** (2015) A959–A964. doi:10.1149/2.0621506jes

[17] P. Ribière, S. Grugeon, M. Morcrette, S. Boyanov, S. Laruelle, and G. Marlair. Investigation on the Fire-Induced Hazards of Li-Ion Battery Cells by Fire Calorimetry. *Energy Environ. Sci.* **5** (2012) 5271–5280. doi:10.1039/c1ee02218k

[18] K. Zhao, M. Pharr, J. J. Vlassak, and Z. Suo. Fracture of Electrodes in Lithium-Ion Batteries Caused by Fast Charging. *J. Appl. Phys.* **108** (2010) 073517. doi:10.1063/1.3492617

[19] M. Odziomek, F. Chaput, A. Rutkowska, K. Świerczek, D. Olszewska, M. Sitarz, F. Lerouge, and S. Parola. Hierarchically Structured Lithium Titanate for Ultrafast Charging in Long-Life High Capacity Batteries. *Nat. Commun.* **8** (2017) 15636. doi:10.1038/ncomms15636

[20] C. M. Hayner, X. Zhao, and H. H. Kung. Materials for Rechargeable Lithium-Ion Batteries. *Annu. Rev. Chem. Biomol. Eng.* **3** (2012) 445–471. doi:10.1146/annurev-chembioeng-062011-081024

[21] A. Magnéli. The Crystal Structures of $Mo_90_{26}$ ($\beta'$-Molybdenum Oxide) and $Mo_80_{23}$ ($\beta$-Molybdenum Oxide). *Acta Chem. Scand.* **8** (1948) 501–517.

[22] R. Roth and A. Wadsley. Multiple Phase Formation in the Binary system $Nb_2O_5$–$WO_3$. I. Preparation and Identification of Phases. *Acta Crystallogr.* **19** (1965) 26–32.

[23] R. S. Roth, A. D. Wadsley, and S. Andersson. The Crystal Structure of $PNb_9O_{25}$ ($P_2O_5{\cdot}9Nb_2O_5$). *Acta Crystallogr.* **18** (1965) 643–647.

[24] S. Andersson and A. D. Wadsley. Crystallographic Shear and Diffusion Paths in Certain Higher Oxides of Niobium, Tungsten, Molybdenum and Titanium. *Nature* **211** (1966) 581–583. doi:10.1038/211581a0

[25] S. Andersson. The Description of Non-Stoichiometric Transition Metal Oxides. A Logical Extension of Inorganic Crystallography. *Bull. Mineral.* **90** (1967) 522–527. URL https://www.persee.fr/doc/bulmi_0037-9328_1967_act_90_4_6039. doi:10.3406/bulmi.1967.6039

[26] A. Cheetham and R. Von Dreele. Cation Distributions in Niobium Oxide Block Structures. *Nat. Phys. Sci.* **244** (1973) 139–140.

[27] R. V. Dreele and A. K. Cheetham. The structures of some titanium-niobium oxides by powder neutron diffraction. *Proc. R. Soc. Lond. A* **338** (1974) 311–326.

[28] D. Murphy, M. Greenblatt, R. J. Cava, and S. Zahurak. Topotactic Lithium Reactions with $ReO_3$ Related Shear Structures. *Solid State Ionics* **5** (1981) 327–329.

[29] R. J. Cava, D. J. Kleinman, and S. M. Zahurak. $V_{3.2}W_{1.8}O_{13}$ and Studies of the $V_2O_5$–$WO_3$–$VO_2$ Ternary System. *Mater. Res. Bull.* **18** (1983) 869–873. doi:10.1016/0025-5408(83)90065-X

[30] R. J. Cava, D. W. Murphy, and S. M. Zahurak. Lithium Insertion in Wadsley-Roth Phases Based on Niobium Oxide. *J. Electrochem. Soc.* **130** (1983) 2345–2351.

[31] R. J. Cava, A. Santoro, D. W. Murphy, S. M. Zahurak, and R. S. Roth. The Structures of the Lithium Inserted Metal Oxides $Li_{0.2}ReO_3$ and $Li_{0.36}WO_3$. *J. Solid State Chem.* **50** (1983) 121–128.

[32] R. J. Cava, D. Murphy, E. Rietman, S. Zahurak, and H. Barz. Lithium Insertion, Electrical Conductivity, and Chemical Substitution in Various Crystallographic Shear Structures. *Solid State Ionics* **9** (1983) 407–411.

[33] J. T. Han, Y. H. Huang, and J. B. Goodenough. New Anode Framework for Rechargeable Lithium Batteries. *Chem. Mater.* **23** (2011) 2027–2029. doi:10.1021/cm200441h

[34] J.-T. Han and J. B. Goodenough. 3-V Full Cell Performance of Anode Framework $TiNb_2O_7$/Spinel $LiNi_{0.5}Mn_{1.5}O_4$. *Chem. Mater.* **23** (2011) 3404–3407.

[35] D. Saritha, V. Pralong, U. V. Varadaraju, and B. Raveau. Electrochemical Li Insertion Studies on $WNb_{12}O_{33}$ – A Shear $ReO_3$ Type Structure. *J. Solid State Chem.* **183** (2010) 988–993.

[36] V. Augustyn, J. Come, M. A. Lowe, J. W. Kim, P. L. Taberna, S. H. Tolbert, H. D. Abruña, P. Simon, and B. Dunn. High-Rate Electrochemical Energy Storage Through $Li^+$ Intercalation Pseudocapacitance. *Nat. Mater.* **12** (2013) 518–522. doi:10.1038/nmat3601

[37] K. J. Griffith, A. C. Forse, J. M. Griffin, and C. P. Grey. High-Rate Intercalation without Nanostructuring in Metastable $Nb_2O_5$ Bronze Phases. *J. Am. Chem. Soc.* **138** (2016) 8888–8899. doi:10.1021/jacs.6b04345

[38] K. J. Griffith, A. Senyshyn, and C. P. Grey. Structural Stability from Crystallographic Shear in $TiO_2$-$Nb_2O_5$ Phases: Cation Ordering and Lithiation Behavior of $TiNb_{24}O_{62}$. *Inorg. Chem.* **56** (2017) 4002–4010. doi:10.1021/acs.inorgchem.6b03154

[39] K. J. Griffith, K. M. Wiaderek, G. Cibin, L. E. Marbella, and C. P. Grey. Niobium Tungsten Oxides for High-Rate Lithium-Ion Energy Storage. *Nature* **559** (2018) 556–563. doi:10.1038/s41586-018-0347-0

[40] K. J. Griffith, I. D. Seymour, M. A. Hope, M. M. Butala, L. K. Lamontagne, M. B. Preefer, C. P. Koçer, G. Henkelman, A. J. Morris, M. J. Cliffe, S. E. Dutton, and C. P. Grey. Ionic and Electronic Conduction in $TiNb_2O_7$. *J. Am. Chem. Soc.* **141** (2019) 16706–16725. doi:10.1021/jacs.9b06669

[41] X. Zhu, J. Xu, Y. Luo, Q. Fu, G. Liang, L. Luo, Y. Chen, C. Lin, and X. Zhao. $MoNb_{12}O_{33}$ as a New Anode Material for High-Capacity, Safe, Rapid and Durable $Li^+$ Storage: Structural Characteristics, Electrochemical Properties and Working Mechanisms. *J. Mater. Chem. A* **7** (2019) 6522–6532.

[42] M. B. Preefer, M. Saber, Q. Wei, N. H. Bashian, J. D. Bocarsly, W. Zhang, G. Lee, J. Milam-Guerrero, E. S. Howard, R. C. Vincent, B. C. Melot, A. Van der Ven, R. Seshadri, and B. S. Dunn. Multielectron Redox and Insulator-to-Metal Transition upon Lithium Insertion in the Fast-Charging, Wadsley-Roth Phase $PNb_9O_{25}$. *Chem. Mater.* **32** (2020) 4553–4563.

[43] C. P. Koçer, K. J. Griffith, C. P. Grey, and A. J. Morris. Cation Disorder and Lithium Insertion Mechanism of Wadsley-Roth Crystallographic Shear Phases from First Principles. *J. Am. Chem. Soc.* **141** (2019) 15121–15134.

[44] N. H. Bashian, S. Zhou, M. Zuba, A. M. Ganose, J. W. Stiles, A. Ee, D. S. Ashby, D. O. Scanlon, L. F. Piper, B. Dunn, and B. C. Melot. Correlated Polyhedral Rotations in the Absence of Polarons during Electrochemi-

cal Insertion of Lithium in $ReO_3$. *ACS Energy Lett.* **3** (2018) 2513–2519. doi:10.1021/acsenergylett.8b01179

[45] K. J. Griffith and C. P. Grey. Superionic Lithium Intercalation through 2×2 $nm^2$ Columns in the Crystallographic Shear Phase $Nb_{18}W_8O_{69}$. *Chem. Mater.* **32** (2020) 3860–3868.

[46] M. W. Gaultois, T. D. Sparks, C. K. Borg, R. Seshadri, W. D. Bonificio, and D. R. Clarke. Data-Driven Review of Thermoelectric Materials: Performance and Resource Considerations. *Chem. Mater.* **25** (2013) 2911–2920.

[47] J. Darriet and J. Galy. $(W_{0.2}V_{0.8})_3O_7$: Synthese et Structure Cristalline. *J. Solid State Chem.* **4** (1972) 357–361.

[48] I. Zibrov, V. Filonenko, V. Sidorov, and S. Lyapin. $V_{3.047}O_7$, a New High-Pressure Oxide with the Simpsonite Structure. *Inorg. Mater.* **52** (2016) 902–908.

[49] A. A. Voskanyan, M. Abramchuk, and A. Navrotsky. Entropy Stabilization of $TiO_2$–$Nb_2O_5$ Wadsley–Roth Shear Phases and Their Prospects for Lithium-Ion Battery Anode Materials. *Chem. Mater.* **32** (2020) 5301–5308.

[50] A. A. Coelho. *TOPAS* and *TOPAS-Academic*: An Optimization Program Integrating Computer Algebra and Crystallographic Objects Written in C++. *J. Appl. Crystallogr.* **51** (2018) 210–218.

[51] K. Momma and F. Izumi. *VESTA 3* For Three-Dimensional Visualization of Crystal, Volumetric and Morphology Data. *J. Appl. Crystallogr.* **44** (2011) 1272–1276.

[52] J. J. Stickel. Data Smoothing and Numerical Differentiation by a Regularization Method. *Comput. Chem. Eng.* **34** (2010) 467–475.

[53] R. Dedryvère, H. Martinez, S. Leroy, D. Lemordant, F. Bonhomme, P. Biensan, and D. Gonbeau. Surface Film Formation on Electrodes in a $LiCoO_2$/Graphite cell: A Step by Step XPS Study. *J. Power Sources* **174** (2007) 462–468.

[54] V. Eshkenazi, E. Peled, L. Burstein, and D. Golodnitsky. XPS Analysis of the SEI Formed on Carbonaceous Materials. *Solid State Ionics* **170** (2004) 83–91.

[55] P. Verma, P. Maire, and P. Novák. A Review of the Features and Analyses of the Solid Electrolyte Interphase in Li-ion Batteries. *Electrochim. Acta* **55** (2010) 6332–6341.

[56] G. Silversmit, D. Depla, H. Poelman, G. B. Marin, and R. De Gryse. Determination of the V2p XPS Binding Energies for Different Vanadium Oxidation States ($V^{5+}$ to $V^{0+}$). *J. Electron Spectrosc. Relat. Phenom.* **135** (2004) 167–175.

[57] G. Kresse and J. Hafner. *Ab initio* Molecular-Dynamics Simulation of the Liquid-Metal–Amorphous-Semiconductor Transition in Germanium. *Phys. Rev. B* **49** (1994) 251–269.

[58] G. Kresse and J. Furthmüller. Efficient Iterative Schemes for *ab initio* Total-Energy Calculations Using a Plane-Wave Basis Set. *Phys. Rev. B* **54** (1996) 169–186. doi:10.1103/PhysRevB.54.11169

[59] G. Kresse and J. Furthmüller. Efficiency of *Ab-Initio* Total Energy Calculations for Metals and Semiconductors Using a Plane-Wave Basis Set. *Comput. Mater. Sci.* **6** (1996) 15–50.

[60] P. E. Blöchl. Projector Augmented-Wave Method. *Phys. Rev. B* **50** (1994) 953–979.

[61] G. Kresse and D. Joubert. From Ultrasoft Pseudopotentials to the Projector Augmented-Wave Method. *Phys. Rev. B* **59** (1999) 1758–1775.

[62] J. P. Perdew, K. Burke, and M. Ernzerhof. Generalized Gradient Approximation Made Simple. *Phys. Rev. Lett.* **77** (1996) 3865–3868.

[63] J. Sun, A. Ruzsinszky, and J. P. Perdew. Strongly Constrained and Appropriately Normed Semilocal Density Functional. *Phys. Rev. Lett.* **115** (2015) 1–6. doi:10.1103/PhysRevLett.115.036402

[64] A. Chakraborty, M. Dixit, D. Aurbach, and D. T. Major. Predicting Accurate Cathode properties of Layered Oxide Materials Using the SCAN Meta-GGA Density Functional. *npj Comput. Mater.* **4** (2018) 1–9.

[65] R. Dronskowski and P. E. Bloechl. Crystal Orbital Hamilton Populations (COHP). Energy-Resolved Visualization of Chemical Bonding in Solids Based on Density-Functional Calculations. *J. Phys. Chem.* **97** (1993) 8617–8624.

[66] V. L. Deringer, A. L. Tchougréeff, and R. Dronskowski. Crystal Orbital Hamilton Population (COHP) Analysis as Projected from Plane-Wave Basis Sets. *J. Phys. Chem. A* **115** (2011) 5461–5466.

[67] S. Maintz, V. L. Deringer, A. L. Tchougréeff, and R. Dronskowski. Analytic Projection From Plane-Wave and PAW Wavefunctions and Application to Chemical-Bonding Analysis in Solids. *J. Comput. Chem.* **34** (2013) 2557–2567.

[68] S. Maintz, V. L. Deringer, A. L. Tchougréeff, and R. Dronskowski. LOBSTER: A Tool to Extract Chemical Bonding from Plane-Wave Based DFT. *J. Comput. Chem.* **37** (2016) 1030–1035.

[69] S. Nishimura. PyAbstantia. *GitHub repository* (2017). URL https://shinichinishimura.github.io/pyabst/, (Accessed on October 11, 2019)

[70] G. Heurung and R. Gruehn. High-Resolution Transmission Electron Microscopy – Investigation of Vanadium–Tungsten Oxides Prepared by Chemical Transport Reactions. *J. Solid State Chem.* **55** (1984) 337–343. doi:10.1016/0022-4596(84)90287-1

[71] J. Allpress, J. Sanders, and A. Wadsley. Multiple Phase Formation in the Binary System $Nb_2O_5$–$WO_3$. VI. Electron Microscopic Observation and Evaluation of Non-Periodic Shear Structures. *Acta Crystallogr. B* **25** (1969) 1156–1164.

[72] K. A. See, M. A. Lumley, G. D. Stucky, C. P. Grey, and R. Seshadri. Reversible Capacity of Conductive Carbon Additives at Low Potentials: Caveats for Testing Alternative Anode Materials for Li-Ion Batteries. *J. Electrochem. Soc.* **164** (2017) A327–A333.

[73] V. Augustyn, P. Simon, and B. Dunn. Pseudocapacitive Oxide Materials for High-Rate Electrochemical Energy Storage. *Energy Environ. Sci.* **7** (2014) 1597–1614. doi:10.1039/c3ee44164d

[74] J. Gopalakrishnan. Insertion/Extraction of Lithium and Sodium in Transition Metal Oxides and Chalcogenides. *Bull. Mater. Sci.* **7** (1985) 201–214.

[75] F. Xie, L. Gong, X. Liu, Y. Tao, W. Zhang, S. Chen, H. Meng, and J. Chen. XPS Studies on Surface Reduction of Tungsten Oxide Nanowire Film by $Ar^+$ Bombardment. *J. Electron Spectrosc. Relat. Phenom.* **185** (2012) 112–118.

[76] S. Adams. From Bond Valence Maps to Energy Landscapes for Mobile Ions in Ion-Conducting Solids. *Solid State Ionics* **177** (2006) 1625–1630.

[77] S. Adams and R. P. Rao. High Power Lithium Ion Battery Materials by Computational Design. *Phys. Status Solidi A* **208** (2011) 1746–1753.

[78] I. D. Brown. Recent Developments in the Methods and Applications of the Bond Valence Model. *Chem. Rev.* **109** (2009) 6858–6919.

[79] C. P. Koçer, K. J. Griffith, C. P. Grey, and A. J. Morris. First-Principles Study of Localized and Delocalized Electronic States in Crystallographic Shear Phases of Niobium Oxide. *Phys. Rev. B* **99** (2019) 075151.

[80] J. Parras, A. Genreith-Schriever, H. Zhang, M. Elm, T. Norby, and R. De Souza. Is $ReO_3$ A mixed Ionic–Electronic conductor? A DFT Study of Defect Formation and Migration in a $B^{VI}O_3$ Perovskite-Type Oxide. *Phys. Chem. Chem. Phys.* **20** (2018) 8008–8015.

[81] T. P. Heins, N. Harms, L.-S. Schramm, and U. Schröder. Development of a New Electrochemical Impedance Spectroscopy Approach for Monitoring the Solid Electrolyte Interphase Formation. *Energy Technol.* **4** (2016) 1509–1513.

[82] B. Scrosati and J. Garche. Lithium Batteries: Status, Prospects and Future. *J. Power Sources* **195** (2010) 2419–2430.

[83] Z. M. Konz, E. J. McShane, and B. D. McCloskey. Detecting the onset of lithium plating and monitoring fast charging performance with voltage relaxation. *ACS Energy Letters* **5** (2020) 1750–1757.

[84] H. Lee, N. Sitapure, S. Hwang, and J. S.-I. Kwon. Multiscale modeling of dendrite formation in lithium-ion batteries. *Computers & Chemical Engineering* **153** (2021) 107415.

[85] K. Kang and G. Ceder. Factors that affect Li mobility in layered lithium transition metal oxides. *Phys. Rev. B* **74** (2006) 094105.

[86] B. Ellis, L. K. Perry, D. H. Ryan, and L. F. Nazar. Small polaron hopping in $Li_xFePO_4$ solid solutions: coupled lithium-ion and electron mobility. *J. Am. Chem. Soc.* **128** (2006) 11416–11422.

[87] L. Croguennec and M. R. Palacin. Recent Achievements on Inorganic Electrode Materials for Lithium-Ion Batteries. *J. Am. Chem. Soc.* **137** (2015) 3140–3156.

[88] G. Hautier, A. Jain, S. P. Ong, B. Kang, C. Moore, R. Doe, and G. Ceder. Phosphates as lithium-ion battery cathodes: an evaluation based on high-throughput ab initio calculations. *Chem. Mater.* **23** (2011) 3495–3508.

[89] Y. Liu, Y. Zhu, and Y. Cui. Challenges and opportunities towards fast-charging battery materials. *Nature Energy* **4** (2019) 540–550.

[90] P. Das, Q. Zayat, B.and Wei, C. Z. S., I. Magdău, R. Elizalde-Segovia, D. Rawlings, D. Lee, G. Pace, A. Irshad, L. Ye, A. Schmitt, R. A. Segalman, T. F. Miller III, S. H. Tolbert, B. S. Dunn, S. R. Narayan, and B. C. Thompson. Dihexyl-substituted poly (3, 4-propylenedioxythiophene) as a dual ionic and electronic conductive cathode binder for lithium-ion batteries. *Chem. Mater.* **32** (2020) 9176–9189.

[91] J. Asenbauer, T. Eisenmann, M. Kuenzel, A. Kazzazi, Z. Chen, and D. Bresser. The success story of graphite as a lithium-ion anode material–fundamentals, remaining challenges, and recent developments including silicon (oxide) composites. *Sustain.Energy Fuels* **4** (2020) 5387–5416.

[92] J. Wandt, J. Jakes, P.and Granwehr, R. Eichel, and H. A. Gasteiger. Quantitative and time-resolved detection of lithium plating on graphite anodes in lithium ion batteries. *Mater Today* **21** (2018) 231–240.

[93] N. H. Bashian, M. B. Preefer, J. Milam-Guerrero, J. J. Zak, C. Sendi, S. A. Ahsan, R. C. Vincent, R. Haiges, K. A. See, R. Seshadri, and B. C. Melot. Understanding the Role of Crystallographic Shear on the Electrochemical Behavior of Niobium Oxyfluorides. *J. Mater. Chem. A* **8** (2020) 12623–12632.

[94] X. Lou, C. Lin, Q. Luo, J. Zhao, B. Wang, Q. Li, J.and Shao, N. Guo, X.and Wang, and Z. Guo. Crystal structure modification enhanced $FeNb_{11}O_{29}$ anodes for lithium-ion batteries. *ChemElectroChem* **4** (2017) 3171–3180.

[95] X. Lou, Q. Fu, J. Xu, X. Liu, C. Lin, J. Han, Y. Luo, Y. Chen, X. Fan, and J. Li. $GaNb_{11}O_{29}$ nanowebs as high-performance anode materials for lithium-ion batteries. *ACS Appl. Nano Mater.* **1** (2017) 183–190.

[96] D. Saritha, V. Pralong, U. V. Varadaraju, and B. Raveau. Electrochemical Li insertion studies on $WNb_{12}O_{33}$—A shear $ReO_3$ type structure. *J. Solid State Chem.* **183** (2010) 988–993.

[97] D. Saritha and U. V. Varadaraju. Studies on electrochemical lithium insertion in isostructural titanium niobate and tantalate phases with shear $ReO_3$ structure. *Mater. Res. Bull.* **48** (2013) 2702–2706.

[98] K. J. Griffith, A. Senyshyn, and C. P. Grey. Structural stability from crystallographic shear in $TiO_2$–$Nb_2O_5$ phases: Cation ordering and lithiation behavior of $TiNb_{24}O_{62}$. *Inorg. Chem.* **56** (2017) 4002–4010.

[99] X. Zhu, Q. Fu, L. Tang, C. Lin, J. Xu, G. Liang, R. Li, L. Luo, and Y. Chen. $Mg_2Nb_{34}O_{87}$ porous microspheres for use in high-energy, safe, fast-charging, and stable lithium-ion batteries. *ACS Appl. Mater. Interfaces* **10** (2018) 23711–23720.

[100] X. Zhu, J. Xu, Y. Luo, Q. Fu, G. Liang, L. Luo, Y. Chen, C. Lin, and X. S. Zhao. $MoNb_{12}O_{33}$ as a new anode material for high-capacity, safe, rapid and durable $Li^+$ storage: structural characteristics, electrochemical properties and working mechanisms. *J. Mater. Chem. A* **7** (2019) 6522–6532.

[101] Y. Li, C. Sun, and J. B. Goodenough. Electrochemical lithium intercalation in monoclinic $Nb_{12}O_{29}$. *Chem. Mater.* **23** (2011) 2292–2294.

[102] K. J. Griffith and C. P. Grey. Superionic lithium intercalation through $2\times2$ $nm^2$ columns in the crystallographic shear phase $Nb_{18}W_8O_{69}$. *Chem. Mater.* **32** (2020) 3860–3868.

[103] Q. Fu, H. Cao, G. Liang, Y. Luo, L.and Chen, V. Murugadoss, S. Wu, T. Ding, C. Lin, and Z. Guo. A highly $Li^+$-conductive $HfNb_{24}O_{62}$ anode material for superior $Li^+$ storage. *Chem. Comm.* **56** (2020) 619–622.

[104] Q. Fu, X. Liu, J. Hou, Y. Pu, C. Lin, L. Yang, X. Zhu, L. Hu, S. Lin, L. Luo, and Y. Chen. Highly conductive $CrNb_{11}O_{29}$ nanorods for use in high-energy, safe, fast-charging and stable lithium-ion batteries. *J. Power Sources* **397** (2018) 231–239.

[105] Y. Li, R. Zheng, H. Yu, X. Cheng, T. Liu, N. Peng, J. Zhang, M. Shui, and J. Shu. Observation of $ZrNb_{14}O_{37}$ nanowires as a lithium container via in situ and ex situ techniques for high-performance lithium-ion batteries. *ACS Appl. Mater. Interfaces* **11** (2019) 22429–22438.

[106] X. Lou, R. Li, X. Zhu, L. Luo, Y. Chen, C. Lin, H. Li, and X. S. Zhao. New anode material for lithium-ion batteries: aluminum niobate ($AlNb_{11}O_{29}$). *ACS Appl. Mater. Interfaces* **11** (2019) 6089–6096.

[107] R. Li, Y. Qin, X. Liu, L. Yang, C. Lin, R. Xia, S. Lin, Y. Chen, and J. Li. Conductive $Nb_{25}O_{62}$ and $Nb_{12}O_{29}$ anode materials for use in high-performance lithium-ion storage. *Electrochim. Acta* **266** (2018) 202–211.

[108] C. Yang, Y. Zhang, F. Lv, C. Lin, Y. Liu, K. Wang, J. Feng, X. Wang, Y. Chen, J. Li, and S. Guo. Porous $ZrNb_{24}O_{62}$ nanowires with pseudocapacitive behavior achieve high-performance lithium-ion storage. *J. Mater. Chem. A* **5** (2017) 22297–22304.

[109] C. Yang, S. Yu, C. Lin, F. Lv, S. Wu, Y. Yang, W. Wang, Z. Zhu, J. Li, N. Wang, and S. Guo. $Cr_{0.5}Nb_{24.5}O_{62}$ nanowires with high electronic conductivity for high-rate and long-life lithium-ion storage. *ACS nano* **11** (2017) 4217–4224.

[110] F. Ran, X. Cheng, H. Yu, R. Zheng, T. Liu, X. Li, N. Ren, M. Shui, and J. Shu. Nano-structured $GeNb_{18}O_{47}$ as novel anode host with superior lithium storage performance. *Electrochim. Acta* **282** (2018) 634–641.

[111] L. Yan, J. Shu, C. Li, X. Cheng, H. Zhu, H. Yu, C. Zhang, Y. Zheng, Y. Xie, and Z. Guo. $W_3Nb_{14}O_{44}$ nanowires: ultrastable lithium storage anode materials for advanced rechargeable batteries. *Energy Storage Mater.* **16** (2019) 535–544.

[112] T. Takashima, T. Tojo, R. Inada, and Y. Sakurai. Characterization of mixed titanium–niobium oxide $Ti_2Nb_{10}O_{29}$ annealed in vacuum as anode material for lithium-ion battery. *J. Power Sources* **276** (2015) 113–119.

[113] X. Zhu, H. Cao, R. Li, Q. Fu, G. Liang, Y. Chen, L. Luo, C. Lin, and X. S. Zhao. Zinc niobate materials: crystal structures, energy-storage capabilities and working mechanisms. *J. Mater. Chem. A* **7** (2019) 25537–25547.

[114] A. Rohatgi. WebPlotDigitizer user manual version 3.4. *URL http://arohatgi.info/WebPlotDigitizer/app* (2014) 1–18.

[115] K. J. Griffith, Y. Harada, S. Egusa, R. M. Ribas, R. S. Monteiro, R. B. Von Dreele, A. K. Cheetham, R. J. Cava, C. P. Grey, and J. B. Goodenough. Titanium niobium oxide: from discovery to application in fast-charging lithium-ion batteries. *Chemistry of Materials* **33** (2020) 4–18.

[116] S. W. Baek, K. E. Wyckoff, D. D. Robertson, M. Frajnkovic̈, Y. Zhou, S. H. Tolbert, R. Seshadri, and L. Pilon. Operando Calorimetry Investigation of Particle Size Effects on Heat Generation in Wadsley–Roth (W0. 2V0. 8) 3O7-Based Electrodes. *ACS Applied Energy Materials* **6** (2023) 1355–1367.

[117] K. E. Wyckoff, D. D. Robertson, M. B. Preefer, S. M. L. Teicher, J. Bienz, L. Kautzsch, T. E. Mates, J. A. Cooley, S. H. Tolbert, and R. Seshadri. High-Capacity $Li^+$ Storage through Multielectron Redox in the Fast-Charging Wadsley–Roth Phase $(W_{0.2}V_{0.8})_3O_7$. *Chem. Mater.* **32** (2020) 9415–9424.

[118] W. Li, H. Y. Asl, Q. Xie, and A. Manthiram. Collapse of $LiNi_{1-x-y}Co_xMn_yO_2$ Lattice at Deep Charge Irrespective of Nickel Content in Lithium-Ion Batteries. *J. Am. Chem. Soc.* **141** (2019) 5097–5101.

[119] Y. Gao, R. Yi, Y. C. Li, J. Song, S. Chen, Q. Huang, T. E. Mallouk, and D. Wang. General Method of Manipulating Formation, Composition, and Morphology of Solid-Electrolyte Interphases for Stable Li-Alloy Anodes. *J. Am. Chem. Soc.* **139** (2017) 17359–17367.

[120] R. Deshpande, M. Verbrugge, Y.-T. Cheng, J. Wang, and P. Liu. Battery Cycle Life Prediction with Coupled Chemical Degradation and Fatigue Mechanics. *J. Electrochem. Soc.* **159** (2012) A1730.

[121] J. Vetter, P. Novák, M. R. Wagner, C. Veit, K.-C. Möller, J. O. Besenhard, M. Winter, M. Wohlfahrt-Mehrens, C. Vogler, and A. Hammouche. Ageing Mechanisms in Lithium-Ion Batteries. *J. Power Sources* **147** (2005) 269–281.

[122] D. Wang, X. Wu, Z. Wang, and L. Chen. Cracking Causing Cyclic Instability of $LiFePO_4$ Cathode Material. *J. Power Sources* **140** (2005) 125–128.

[123] Y. Wang, X. Guo, S. Greenbaum, J. Liu, and K. Amine. Solid Electrolyte Interphase Formation on Lithium-Ion Electrodes: A $^7$Li Nuclear Magnetic Resonance Study. *Electrochem. Solid State Lett.* **4** (2001) A68.

[124] X. Lu, L. Gu, Y.-S. Hu, H.-C. Chiu, H. Li, G. P. Demopoulos, and L. Chen. New Insight Into the Atomic-Scale Bulk and Surface Structure Evolution of $Li_4Ti_5O_{12}$ Anode. *J. Am. Chem. Soc.* **137** (2015) 1581–1586.

[125] H. Tavassol, E. M. Jones, N. R. Sottos, and A. A. Gewirth. Electrochemical Stiffness in Lithium-Ion Batteries. *Nat. Mater.* **15** (2016) 1182–1187.

[126] C. Xu, K. Märker, J. Lee, A. Mahadevegowda, P. J. Reeves, S. J. Day, M. F. Groh, S. P. Emge, C. Ducati, B. L. Mehdi, C. C. Tang, and C. P. Grey. Bulk fatigue induced by surface reconstruction in layered Ni-rich cathodes for Li-ion batteries. *Nat. Mater.* **20** (2021) 84–92.

[127] N. Li, M. Sun, W. H. Kan, Z. Zhuo, S. Hwang, S. E. Renfrew, M. Avdeev, A. Huq, B. D. McCloskey, D. Su, W. Yang, and W. Tong. Layered-Rocksalt Intergrown Cathode for High-Capacity Zero-Strain Battery Operation. *Nat. Commun.* **12** (2021) 1–10.

[128] M. Wu, X. Xiao, N. Vukmirovic, S. Xun, P. K. Das, X. Song, P. Olalde-Velasco, D. Wang, A. Z. Weber, L.-W. Wang, V. S. Battaglia, W. Yang, and L. Gao. Toward an Ideal Polymer Binder Design for High-Capacity Battery Anodes. *J. Am. Chem. Soc.* **135** (2013) 12048–12056.

[129] P. Das, B. Zayat, Q. Wei, C. Z. Salamat, I.-B. Magdău, R. Elizalde-Segovia, D. Rawlings, D. Lee, G. Pace, A. Irshad, L. Ye, A. Schmitt, R. A. Segalman, T. F. Miller III, S. H. Tolbert, B. Dunn, S. R. Narayan, and B. C. Thompson. Dihexyl-Substituted Poly (3,4–Propylenedioxythiophene) as a Dual Ionic and Electronic Conductive Cathode Binder for Lithium-Ion Batteries. *Chem. Mater.* **32** (2020) 9176–9189.

[130] L. Zhang, H. B. Wu, S. Madhavi, H. H. Hng, and X. W. Lou. Formation of $Fe_2O_3$ Microboxes with Hierarchical Shell Structures from Metal–Organic Frameworks and their Lithium Storage Properties. *J. Am. Chem. Soc.* **134** (2012) 17388–17391.

[131] J. Li, Q. Zhang, X. Xiao, Y.-T. Cheng, C. Liang, and N. J. Dudney. Unravelling the Impact of Reaction Paths on Mechanical Degradation of Intercalation Cathodes for Lithium-Ion Batteries. *J. Am. Chem. Soc.* **137** (2015) 13732–13735.

[132] J. N. Reimers and J. R. Dahn. Electrochemical and In Situ X-Ray Diffraction Studies of Lithium Intercalation in $Li_xCoO_2$. *J. Electrochem. Soc.* **139** (1992) 2091.

[133] J. Cho, Y. J. Kim, T.-J. Kim, and B. Park. Zero-Strain Intercalation Cathode for Rechargeable Li-Ion Cell. *Angew. Chem.* **113** (2001) 3471–3473.

[134] T. Ohzuku, A. Ueda, and M. Kouguchi. Synthesis and Characterization of $LiAl_{1/4}Ni_{3/4}O_2$ ($R-3m$) for Lithium-Ion (Shuttlecock) Batteries. *J. Electrochem. Soc.* **142** (1995) 4033.

[135] J. Waring and R. Roth. Phase Equilibria in the System Vanadium Oxide-Niobium Oxide. *J. Res. Nat. Bur. Stand. Sec. A* **69A** (1965) 119–129.

[136] A. A. Voskanyan and A. Navrotsky. Shear Pleasure: The Structure, Formation, and Thermodynamics of Crystallographic Shear Phases. *Annu Rev. Mater. Res.* **51** (2021) 521–540.

[137] B. Guo, X. Yu, X.-G. Sun, M. Chi, Z.-A. Qiao, J. Liu, Y.-S. Hu, X.-Q. Yang, J. B. Goodenough, and S. Dai. A Long-Life Lithium-Ion Battery with a Highly Porous $TiNb_2O_7$ Anode for Large-Scale Electrical Energy Storage. *Energy Environ. Sci.* **7** (2014) 2220–2226.

[138] K. J. Griffith, Y. Harada, S. Egusa, R. M. Ribas, R. S. Monteiro, R. B. Von Dreele, A. K. Cheetham, R. J. Cava, C. P. Grey, and J. B. Goodenough. Titanium Niobium Oxide: From Discovery to Application in Fast-Charging Lithium-Ion Batteries. *Chem. Mater.* **33** (2020) 4–18.

[139] S. W. Baek, K. E. Wyckoff, D. M. Butts, J. Bienz, A. Likitchatchawankun, M. B. Preefer, M. Frajnkovič, B. S. Dunn, R. Seshadri, and L. Pilon. Operando Calorimetry Informs the Origin of Rapid Rate Performance in Microwave-Prepared $TiNb_2O_7$ Electrodes. *J. Power Sources* **490** (2021) 229537.

[140] K. McColl, K. J. Griffith, R. L. Dally, R. Li, J. E. Douglas, K. R. Poeppelmeier, F. Corà, I. Levin, and M. M. Butala. Energy Storage Mechanisms in Vacancy-Ordered Wadsley–Roth Layered Niobates. *J. Mater. Chem. A* **9** (2021) 20006–20023.

[141] C. C. Torardi and R. E. McCarley. Sodium Tetramolybdenum Hexoxide ($NaMo_4O_6$). A Metallic Infinite-Chain Polymer Derived by Condensation of Octahedral Clusters. *J. Am. Chem. Soc.* **101** (1979) 3963–3964.

[142] J. B. Goodenough. Chemistry and Uses of Molybdenum. In *Proc. Climax 4th Int. Conf., Barry HF and Mitchell PC, Eds., Ann Arbor: Climax Molybdenum Corp*, volume 1 (1982) page 1.

[143] A. M. Chippindale and A. K. Cheetham. The Oxide Chemistry of Molybdenum. *Studies Inorg. Chem.* **19** (1994) 146–184.

[144] W. H. McCarroll, L. Katz, and R. Ward. Some Ternary Oxides of Tetravalent Molybdenum. *J. Am. Chem. Soc.* **79** (1957) 5410–5414.

[145] P. C. Donohue and L. Katz. A Lithium-Scandium-Molybdenum (IV) Oxide. *Nature* **201** (1964) 180–181.

[146] J. DeBenedittis and L. Katz. Complex Metal Oxides of the Type $AMMo_3^{IV}O_8$. *Inorg. Chem.* **4** (1965) 1836–1839.

[147] W. H. McCarroll. Structural Relationships in $ARMo_3O_8$ Metal Atom Cluster Oxides. *Inorg. Chem.* **16** (1977) 3351–3353.

[148] B. Das, M. V. Reddy, G. V. S. Rao, and B. V. R. Chowdari. Synthesis of Mo-cluster compound, $LiHoMo_3O_8$ by carbothermal reduction and its reactivity towards Li. *J. Solid State Electrochem.* **12** (2008) 953–959.

[149] B. Das, M. Reddy, C. Krishnamoorthi, S. Tripathy, R. Mahendiran, G. S. Rao, and B. Chowdari. Carbothermal synthesis, spectral and magnetic characterization and Li-cyclability of the Mo-cluster compounds, $LiYMo_3O_8$ and $Mn_2Mo_3O_8$. *Electrochim Acta* **54** (2009) 3360–3373.

[150] R. Chevrel, M. Sergent, and J. Prigent. Sur de nouvelles phases sulfurées ternaires du molybdène. *J. Solid State Chem.* **3** (1971) 515–519.

[151] D. Aurbach, Z. Lu, A. Schechter, Y. Gofer, H. Gizbar, R. Turgeman, Y. Cohen, M. Moshkovich, and E. Levi. Prototype systems for rechargeable magnesium batteries. *Nature* **407** (2000) 724–727.

[152] P. Saha, P. H. Jampani, M. K. Datta, D. Hong, C. U. Okoli, A. Manivannan, and P. N. Kumta. Electrochemical Performance of Chemically and Solid State-Derived Chevrel Phase $Mo_6T_8$ (T= S, Se) Positive Electrodes for Sodium-Ion Batteries. *J. Phys. Chem. C* **119** (2015) 5771–5782.

[153] M. D. Levi and D. Aurbach. A comparison between intercalation of Li and Mg ions into the model Chevrel phase compound ($M_xMo_6S_8$): Impedance spectroscopic studies. *J. Power Sources* **146** (2005) 349–354.

[154] L. Vitoux, M. Guignard, N. Penin, D. Carlier, J. Darriet, and C. Delmas. $NaMoO_2$: a Layered Oxide with Molybdenum Clusters. *Inorg. Chem.* **59** (2020) 4015–4023.

[155] Y. Takeda, R. Kanno, T. Tanaka, and O. Yamamoto. Lithium/$V_9Mo_6O_{40}$ Cells. *J. Electrochem. Soc.* **134** (1987) 641.

[156] S. Britto, M. Leskes, X. Hua, C.-A. Hébert, H. S. Shin, S. Clarke, O. Borkiewicz, K. W. Chapman, R. Seshadri, J. Cho, and C. P. Grey. Multiple Redox Modes in the Reversible Lithiation of High-Capacity, Peierls-Distorted Vanadium Sulfide. *J. Am. Chem. Soc.* **137** (2015) 8499–8508.

[157] A. Walsh, A. A. Sokol, J. Buckeridge, D. O. Scanlon, and C. R. A. Catlow. Oxidation States and Ionicity. *Nat. Mater.* **17** (2018) 958–964.

[158] C. J. Hansen, J. J. Zak, A. J. Martinolich, J. S. Ko, N. H. Bashian, F. Kaboudvand, A. Van der Ven, B. C. Melot, J. Nelson Weker, and K. A. See. Multielectron, Cation and Anion Redox in Lithium-Rich Iron Sulfide Cathodes. *J. Am. Chem. Soc.* **142** (2020) 6737–6749.

[159] D. A. Kitchaev, J. Vinckeviciute, and A. Van der Ven. Delocalized Metal–Oxygen $\pi$-Redox is the Origin of Anomalous Nonhysteretic Capacity in Li-Ion and Na-Ion Cathode Materials. *J. Am. Chem. Soc.* **143** (2021) 1908–1916.

[160] S. W. Baek, K. E. Wyckoff, D. M. Butts, J. Bienz, A. Likitchatchawankun, M. B. Preefer, M. Frajnkovič, B. S. Dunn, R. Seshadri, and L. Pilon. *Operando* Calorimetry Informs the Origin of Rapid Rate Performance in Microwave-prepared $TiNb_2O_7$ Electrodes. *J. Power Sources* **490** (2021) 229537.

[161] A. Van der Ven, J. Bhattacharya, and A. A. Belak. Understanding Li Diffusion in Li-Intercalation Compounds. *Acc. Chem. Res.* **46** (2013) 1216–1225.

[162] M. J. Moran, M. B. Bailey, D. D. Boettner, and H. N. Shapiro. *Fundamentals of Engineering Thermodynamics*. Wiley (2018).

[163] V. V. Viswanathan, D. Choi, D. Wang, W. Xu, S. Towne, R. E. Williford, J.-G. Zhang, J. Liu, and Z. Yang. Effect of entropy change of lithium intercalation in cathodes and anodes on $Li^+$ion battery thermal management. *Journal of Power Sources* **195** (2010) 3720–3729.

[164] X.-F. Zhang, Y. Zhao, Y. Patel, T. Zhang, W.-M. Liu, M. Chen, G. J. Offer, and Y. Yan. Potentiometric Measurement of Entropy Change for Lithium Batteries. *Phys. Chem. Chem. Phys.* **19** (2017) 9833–9842.

[165] S. Schlueter, R. Genieser, D. Richards, H. E. Hoster, and M. P. Mercer. Quantifying Structure Dependent Responses in Li-Ion Cells with Excess Li Spinel Cathodes: Matching Voltage and Entropy Profiles through Mean Field Models. *Phys. Chem. Chem. Phys.* **20** (2018) 21417–21429.

[166] G. Kresse and J. Hafner. Ab Initio Molecular Dynamics for Liquid Metals. *Phys. Rev. B* **47** (1993) 558–561. doi:10.1103/PhysRevB.47.558

[167] G. Kresse and J. Hafner. Ab Initio Molecular-Dynamics Simulation of the Liquid-Metal–Amorphous-Semiconductor Transition in Germanium. *Phys. Rev. B* **49** (1994) 14251–14269. doi:10.1103/PhysRevB.49.14251

[168] G. Kresse and J. Furthmüller. Efficiency of Ab-Initio Total Energy Calculations for Metals and Semiconductors Using a Plane-Wave Basis Set. *Computational Mater. Sci.* **6** (1996) 15–50. doi:10.1016/0927-0256(96)00008-0

[169] G. Kresse and J. Furthmüller. Efficient Iterative Schemes for Ab Initio Total-Energy Calculations Using a Plane-Wave Basis Set. *Phys. Rev. B* **54** (1996) 11169–11186. doi:10.1103/PhysRevB.54.11169

[170] P. E. Blöchl. Projector Augmented-Wave Method. *Phys. Rev. B* **50** (1994) 17953–17979. doi:10.1103/PhysRevB.50.17953

[171] G. Kresse and D. Joubert. From Ultrasoft Pseudopotentials to the Projector Augmented-Wave Method. *Phys. Rev. B* **59** (1999) 1758–1775. doi:10.1103/PhysRevB.59.1758

[172] J. Sun, A. Ruzsinszky, and J. P. Perdew. Strongly Constrained and Appropriately Normed Semilocal Density Functional. *Phys. Rev. Lett.* **115** (2015) 036402. doi:10.1103/PhysRevLett.115.036402

[173] J. Sun, R. C. Remsing, Y. Zhang, Z. Sun, A. Ruzsinszky, H. Peng, Z. Yang, A. Paul, U. Waghmare, X. Wu, M. L. Klein, and J. P. Perdew. Accurate First-Principles Structures and Energies of Diversely Bonded Systems from an Efficient Density Functional. *Nat. Chem.* **8** (2016) 831–836. doi:10.1038/nchem.2535

[174] H. J. Monkhorst and J. D. Pack. Special Points for Brillouin-Zone Integrations. *Phys. Rev. B* **13** (1976) 5188–5192. doi:10.1103/PhysRevB.13.5188

[175] P. E. Blöchl, O. Jepsen, and O. K. Andersen. Improved Tetrahedron Method for Brillouin-Zone Integrations. *Phys. Rev. B* **49** (1994) 16223–16233. doi:10.1103/PhysRevB.49.16223

[176] CASM: A Clusters Approach to Statistical Mechanics. https://github.com/prisms-center/CASMcode (2021).

[177] J. C. Thomas and A. Van der Ven. Finite-Temperature Properties of Strongly Anharmonic and Mechanically Unstable Crystal Phases from First Principles. *Phys. Rev. B* **88** (2013) 214111. doi:10.1103/PhysRevB.88.214111

[178] A. Van der Ven, J. Thomas, B. Puchala, and A. Natarajan. First-Principles Statistical Mechanics of Multicomponent Crystals. *Annu. Rev. Mater. Res.* **48** (2018) 27–55. doi:10.1146/annurev-matsci-070317-124443

[179] B. Puchala and A. Van der Ven. Thermodynamics of the Zr-O system from first-principles calculations. *Phys. Rev. B* **88** (2013) 094108. doi:10.1103/PhysRevB.88.094108

[180] H.-S. Kim, J. B. Cook, H. Lin, J. S. Ko, S. H. Tolbert, V. Ozolins, and B. Dunn. Oxygen Vacancies Enhance Pseudocapacitive Charge Storage Properties of $MoO_{3-x}$. *Nat. Mater.* **16** (2017) 454–460.

[181] K. Tsuge, H. Imoto, and T. Saito. Synthesis, Structure, and Molecular Orbital Calculation of the Bicapped Triangular Molybdenum Cluster Complex $[Mo_3S_5(PMe_3)_6]$. *Inorg. Chem.* **34** (1995) 3404–3409.

[182] A. Van der Ven, J. Bhattacharya, and A. A. Belak. Understanding Li Diffusion in Li-Intercalation Compounds. *Acc. Chem. Res.* **46** (2013) 1216–1225.

[183] Y. Hinuma, H. Hayashi, Y. Kumagai, I. Tanaka, and F. Oba. Comparison of Approximations in Density Functional Theory Calculations: Energetics and Structure of Binary Oxides. *Phys. Rev. B* **96** (2017) 094102.

[184] G.-X. Zhang, A. M. Reilly, A. Tkatchenko, and M. Scheffler. Performance of Various Density-Functional Approximations for Cohesive Properties of 64 Bulk Solids. *New J. Phys.* **20** (2018) 063020.

[185] A. M. Fry-Petit, A. F. Rebola, M. Mourigal, M. Valentine, N. Drichko, J. P. Sheckelton, C. J. Fennie, and T. M. McQueen. Direct Assignment of Molecular Vibrations via Normal Mode Analysis of the Neutron Dynamic Pair Distribution Function Technique. *J. Chem. Phys.* **143** (2015) 124201.

[186] V. V. T. Doan-Nguyen, K. S. Subrahmanyam, M. M. Butala, J. A. Gerbec, S. M. Islam, K. N. Kanipe, C. E. Wilson, M. Balasubramanian, K. M. Wiaderek, O. J. Borkiewicz, K. W. Chapman, P. J. Chupas, M. Moskovits, B. S. Dunn, M. G. Kanatzidis, and R. Seshadri. Molybdenum Polysulfide Chalcogels as High-Capacity, Anion-Redox-Driven Electrode Materials for Li-Ion Batteries. *Chem. Mater.* **28** (2016) 8357–8365.

[187] J. R. Schoonover, T. C. Zietlow, D. L. Clark, J. A. Heppert, M. H. Chisholm, H. B. Gray, A. P. Sattelberger, and W. H. Woodruff. Resonance Raman Spectra of $[M_6X_8Y_6]^{2-}$ Cluster Complexes (M = Mo, W; X, Y= Cl, Br, I). *Inorg. Chem.* **35** (1996) 6606–6613.

[188] E. Deiss. Spurious Chemical Diffusion Coefficients of $Li^+$ in Electrode Materials Evaluated With GITT. *Electrochim. Acta* **50** (2005) 2927–2932.

[189] J. Dahn and R. Haering. Entropy Measurements on $Li_xTiS_2$. *Canadian J. Phys.* **61** (1983) 1093–1098.

[190] Y. Haraguchi, C. Michioka, M. Imai, H. Ueda, and K. Yoshimura. Spin-Liquid Behavior in the Spin-Frustrated $Mo_3$ Cluster Magnet $Li_2ScMo_3O_8$ in Contrast to Magnetic Ordering in Isomorphic $Li_2InMo_3O_8$. *Phys. Rev. B* **92** (2015) 014409.

[191] W. D. Johnston, R. R. Heikes, and D. Sestrich. The Preparation, Crystallography, and Magnetic Properties of the $Li_xCo_{(1-x)}O$ System. *J. Phys. Chem. Solids* **7** (1958) 1–13.

[192] K. Mizushima, P. C. Jones, P. J. Wiseman, and J. B. Goodenough. $Li_xCoO_2$ ($0 < x < 1$): A New Cathode Material for Batteries of High Energy Density. *Mater. Res. Bull.* **15** (1980) 783–789.

[193] H. Nguyen and R. J. Clément. Rechargeable Batteries from the Perspective of the Electron Spin. *ACS Energy Lett.* **5** (2020) 3848–3859.

[194] T. Motohashi, T. Ono, Y. Sugimoto, Y. Masubuchi, S. Kikkawa, R. Kanno, M. Karppinen, and H. Yamauchi. Electronic Phase Diagram of the Layered Cobalt Oxide System $Li_xCoO_2$ ($0.0 \leq x \geq 1.0$). *Phys. Rev. B* **80** (2009) 165114.

[195] T. J. Diethrich, S. Gnewuch, K. G. Dold, K. M. Taddei, and E. E. Rodriguez. Tuning Magnetic Symmetry and Properties in the Olivine Series $Li_{1-x}Fe_xMn_{1-x}PO_4$ Through Selective Delithiation. *Chem. Mater.* **34** (2022) 5039–5053.

[196] P. Mukherjee, J. A. M. Paddison, C. Xu, Z. Ruff, A. R. Wildes, D. A. Keen, R. I. Smith, C. P. Grey, and S. E. Dutton. Sample Dependence of Magnetism in the Next-Generation Cathode Material $LiNi_{0.8}Mn_{0.1}Co_{0.1}O_2$. *Inorg. Chem.* **60** (2020) 263–271.

[197] Q. Xia, X. Li, K. Wang, Z. Li, H. Liu, W. Wang, X.and Ye, H. Li, X. Teng, J. Pang, Q. Zhang, C. Ge, L. Gu, G. Miao, S. Yan, H. Hu, and Q. Li. Unraveling the Evolution of Transition Metals during Li Alloying–Dealloying by In-Operando Magnetometry. *Chem. Mater.* **34** (2022) 5852–5859.

[198] K. Romanenko, P. W. Kuchel, and A. Jerschow. Accurate Visualization of Operating Commercial Batteries Using Specialized Magnetic Resonance Imaging with Magnetic Field Sensing. *Chem. Mater.* **32** (2020) 2107–2113.

[199] G. H. Wannier. Antiferromagnetism. The Triangular Ising Net. *Phys. Rev.* **79** (1950) 357.

[200] A. P. Ramirez. Strongly Geometrically Frustrated Magnets. *Annu. Rev. of Mater. Sci.* **24** (1994) 453–480.

[201] L. Balents. Spin Liquids in Frustrated Magnets. *Nature* **464** (2010) 199–208.

[202] P. W. Anderson. The Resonating Valence Bond State in $La_2CuO_4$ and Superconductivity. *Science* **235** (1987) 1196–1198.

[203] M. R. Norman. Colloquium: Herbertsmithite and the Search for the Quantum Spin Liquid. *Rev. Mod. Phys.* **88** (2016) 041002.

[204] M. P. Shores, E. A. Nytko, B. M. Bartlett, and D. G. Nocera. A Structurally Perfect S= 1/2 Kagome Antiferromagnet. *J. Am. Chem. Soc.* **127** (2005) 13462–13463.

[205] J. P. Sheckelton, J. R. Neilson, D. G. Soltan, and T. M. McQueen. Possible Valence-Bond Condensation in the Frustrated Cluster Magnet $LiZn_2Mo_3O_8$. *Nat. Mater.* **11** (2012) 493–496.

[206] L. Jiao, Q. Xu, Y. Cheon, Y. Sun, C. Felser, E. Liu, and S. Wirth. Signatures for Half-Metallicity and Nontrivial Surface States in the Kagome Lattice Weyl Semimetal $Co_3Sn_2S_2$. *Phys. Rev. B* **99** (2019) 245158.

[207] B. R. Ortiz, L. C. Gomes, J. R. Morey, M. Winiarski, M. Bordelon, J. S. Mangum, I. W. H. Oswald, J. A. Rodriguez-Rivera, J. R. Neilson, S. D. Wilson, E. Ertekin, T. M. McQueen, and E. S. Toberer. New Kagome Prototype Materials: Discovery of $KV_3Sb_5$, $RbV_3Sb_5$, and $CsV_3Sb_5$. *Phys. Rev. Mat.* **3** (2019) 094407.

[208] Q. Chen, R. Sinclair, A. Akbari-Sharbaf, Q. Huang, Z. Dun, E. S. Choi, M. Mourigal, A. Verrier, R. Rouane, X. Bazier-Matte, J. A. Quilliam, A. A. Aczel, and H. D. Zhou. Magnetic Order and Spin Liquid Behavior in $[Mo_3]^{11+}$ Molecular Magnets. *Phys. Rev. Mater.* **6** (2022) 044414.

[209] K. Iida, H. Yoshida, H. Okabe, N. Katayama, Y. Ishii, A. Koda, Y. Inamura, N. Murai, M. Ishikado, R. Kadono, and R. Kajimoto. Quantum magnetisms in uniform triangular lattices $Li_2AMo_3O_8$ ($A$= In, Sc). *Sci. Rep.* **9** (2019) 1–9.

[210] J. P. Sheckelton, F. R. Foronda, L. Pan, C. Moir, R. D. McDonald, T. Lancaster, P. J. Baker, N. P. Armitage, T. Imai, S. J. Blundell, and T. M. McQueen. Local Magnetism and Spin Correlations in the Geometrically Frustrated Cluster Magnet $LiZn_2Mo_3O_8$. *Phys. Rev. B* **89** (2014) 064407.

[211] M. Mourigal, W. T. Fuhrman, J. P. Sheckelton, A. Wartelle, J. A. Rodriguez-Rivera, D. L. Abernathy, T. M. McQueen, and C. L. Broholm. Molecular Quantum Magnetism in $LiZn_2Mo_3O_8$. *Phys. Rev. Lett.* **112** (2014) 027202.

[212] D. I. Khomskii and S. V. Streltsov. Orbital Effects in Solids: Basics, Recent Progress, and Opportunities. *Chem. Rev.* **121** (2020) 2992–3030.

[213] S. A. Nikolaev, I. V. Solovyev, and S. V. Streltsov. Quantum Spin Liquid and Cluster Mott Insulator Phases in the $Mo_3O_8$ Magnets. $npj$ *Quantum Mater.* **6** (2021) 1–8.

[214] G. Chen, H. Kee, and Y. B. Kim. Cluster Mott Insulators and Two Curie-Weiss Regimes on an Anisotropic Kagome Lattice. *Phys. Rev. B* **93** (2016) 245134.

[215] K. E. Wyckoff, J. L. Kaufman, S. W. Baek, C. Dolle, J. J. Zak, J. Bienz, L. Kautzsch, R. C. Vincent, A. Zohar, K. A. See, Y. M. Eggeler, L. Pilon, A. Van der Ven, and R. Seshadri. Metal–Metal Bonding as an Electrode Design Principle in the Low-Strain Cluster Compound $LiScMo_3O_8$. *J. Am. Chem. Soc.* **144** (2022) 5841–5854.

[216] A. Akbari-Sharbaf, R. Sinclair, A. Verrier, D. Ziat, H. D. Zhou, X. F. Sun, and J. A. Quilliam. Tunable Quantum Spin Liquidity in the 1/6 th-Filled Breathing Kagome Lattice. *Phys. Rev. Lett.* **120** (2018) 227201.

[217] M. D. Radin and A. Van der Ven. Stability of prismatic and octahedral coordination in layered oxides and sulfides intercalated with alkali and alkaline-earth metals. *Chem. Mater.* **28** (2016) 7898–7904.

[218] A. K. Cheetham, R. Seshadri, and F. Wudl. Chemical Synthesis and Materials Discovery. *Nature Synthesis* (2022) 1–7.

[219] S. Calder, K. An, R. Boehler, C. R. Dela Cruz, M. D. Frontzek, M. Guthrie, B. Haberl, A. Huq, S. A. J. Kimber, J. Liu, J. J. Molaison, J. Neuefeind, K. Page, A. M. dos Santos, K. M. Taddei, C. Tulk, and M. G. Tuker. A Suite-Level Review of the Neutron Powder Diffraction Instruments at Oak Ridge National Laboratory. *Rev. Sci. Instrum.* **89** (2018) 092701.

[220] J. Neuefeind, M. Feygenson, J. Carruth, R. Hoffmann, and K. K. Chipley. The Nanoscale Ordered Materials Diffractometer NOMAD at the Spallation Neutron Source SNS. *Nucl. Instrum. Methods Phys. Res. B* **287** (2012) 68–75.

[221] J. Liu, Z. Du, X. Wang, S. Tan, X. Wu, L. Geng, B. Song, P. Chien, S. Michelle Everett, and E. Hu. Anionic Redox Induced Anomalous Structural Transition in Ni-rich Cathodes. *Energy Environ. Sci.* **14** (2021) 6441–6454.

[222] Y. Zhang, J. Liu, and M. G. Tucker. Lorentz Factor for Time-of-Flight Neutron Bragg and Total Scattering. *Acta Crystallogr. A* **79** (2023).

[223] O. J. Borkiewicz, B. Shyam, K. M. Wiaderek, C. Kurtz, P. J. Chupas, and K. W. Chapman. The AMPIX Electrochemical Cell: A Versatile Apparatus for In Situ X-ray Scattering and Spectroscopic Measurements. *J. Appl. Crystallogr.* **45** (2012) 1261–1269.

[224] Y. Haraguchi, C. Michioka, H. Ueda, and K. Yoshimura. Charge Fluctuation in $S = 1/2$ Triangular Lattice Cluster Antiferromagnets $Li_2ScMo_3O_8$ and $Li_2InMo_3O_8$. *J. Phys.: Conf. Series* **868** (2017) 012022.

[225] A. D. Fortes, I. G. Wood, J. P. Brodholt, M. Alfredsson, L. Vočadlo, G. S. McGrady, and K. S. Knight. A High-Resolution Neutron Powder Diffraction Study of Ammonia Dihydrate ($ND_3{\cdot}2D_2O$) phase I. *Chem. Phys.* **119** (2003) 10806–10813.

[226] M. C. Kemei, P. T. Barton, S. L. Moffitt, M. W. Gaultois, J. A. Kurzman, R. Seshadri, M. R. Suchomel, and Y. Kim. Crystal Structures of Spin-Jahn–Teller-Ordered $MgCr_2O_4$ and $ZnCr_2O_4$. *J. Phys. Condens. Matter* **25** (2013) 326001.